


2010-01-01

Development Of Wide Band Gap Semiconductor Materials For Renewable Energy

S.m. Sarif Masud

University of Texas at El Paso, ssmasud@miners.utep.edu

Follow this and additional works at: https://digitalcommons.utep.edu/open_etd

 Part of the [Chemical Engineering Commons](#), [Nanoscience and Nanotechnology Commons](#), and the [Oil, Gas, and Energy Commons](#)

Recommended Citation

Masud, S.m. Sarif, "Development Of Wide Band Gap Semiconductor Materials For Renewable Energy" (2010). *Open Access Theses & Dissertations*. 2728.

https://digitalcommons.utep.edu/open_etd/2728

This is brought to you for free and open access by DigitalCommons@UTEP. It has been accepted for inclusion in Open Access Theses & Dissertations by an authorized administrator of DigitalCommons@UTEP. For more information, please contact lweber@utep.edu.

DEVELOPMENT OF WIDE BAND GAP SEMICONDUCTOR
MATERIALS FOR RENEWABLE ENERGY

S. M. SARIF MASUD

Materials Science and Engineering

APPROVED:

Geoffrey B. Saupe, Ph.D., Chair

Jorge Gardea-Torresdey, Ph.D.

Cristian E. Botez, Ph.D.

Ramana V. Chintalapalle, Ph.D.

Roy Arrowood, Ph.D.

Patricia D. Witherspoon, Ph.D.
Dean of the Graduate School

Copyright ©

by

S. M. Sarif Masud

2010

Dedication

To the people who are incessantly striving for a better environment for their successors,
as did my parents Anwar Hossain & Anwara Begum.

DEVELOPMENT OF WIDE BAND GAP SEMICONDUCTOR
MATERIALS FOR RENEWABLE ENERGY

by

S. M. SARIF MASUD, M.S.

DISSERTATION

Presented to the Faculty of the Graduate School of
The University of Texas at El Paso
in Partial Fulfillment
of the Requirements
for the Degree of

DOCTOR OF PHILOSOPHY

Materials Science and Engineering

THE UNIVERSITY OF TEXAS AT EL PASO

May 2010

Acknowledgements

I would like to acknowledge Dr. Geoffrey B. Saupe, my dissertation supervising professor for his guidance throughout my study, proving a friendly environment in which to work independently, tolerance of my messy work, motivation to think beyond the research ideology, listening and helping my personal problems, and trying to help whenever he can by supporting me on my rainy days. Dr. Lawrence E. Murr, Program Director of The Materials Science and Engineering Program gave me financial support throughout my study, helped me find the right supervisor in my research interests, and generously permitted me to use SEM, TEM and XRD in his department. My hat is off for you sir. I am very much grateful to Dr. Jorge Gardea-Torresdey, Chair, Department of Chemistry for his permission to use his laboratory to a great extent. I am also very much grateful to Dr. Ramana V. Chintalapalle who trained me to run the SEM. Thanks to Dr. Mahsa Hosseini and Dr. Maryam Zarei, who were always helping me by giving me their research ideas, instrumentation ability, and friendly tips. I really appreciate their valuable time. I acknowledge The Graduate School at The University of Texas at El Paso for their generosity, supporting me through The Dodson Dissertation Fellowship, Research Award, Cotton Memorial Scholarship and Travel Award for twelve national and international conferences. Last but not least, I am really grateful to my wife Munne who always supports me in my job. Without her support it would not have been possible to finish my dissertation.

Abstract

Several new wide band gap semiconductor nanocomposite photocatalytic materials have been synthesized from HTiNbO_5 and HNb_3O_8 for solar energy conversion. As a source of renewable energy, the materials are being tested to produce hydrogen fuel from water via photolysis. The materials have high surface areas, are macroporous, and have flatband potentials suitable for reducing water to create hydrogen. Under visible or ultra violet light, the materials were found to be very promising as hydrogen evolving photocatalysts. As part of the synthesis of the composites, the catalysts also exhibited excellent catalytic activity under UV light for reducing ionic platinum and gold out of solution and onto the surfaces of the catalysts. A topotactic dehydration treatment was also developed as a way to enhance the electronic conductivity within the solids and to improve catalytic activity. Topotactic dehydration increased the photocatalytic activity of the wide band gap semiconducting materials as much as 75% in some cases. Under visible light and when sensitized with N3 dye (cis-bis(isothio cyanato)bis(2,2'-bipyridyl-4,4'-dicarboxylato)-ruthenium(II)), these materials exhibited their great potential in producing hydrogen from water splitting under sunlight, with a maximum apparent quantum yield of 61.66%.

Table of Contents

Acknowledgements.....	v
Abstract.....	vi
Table of Contents.....	vii
List of Tables	x
List of Figures.....	xi
List of Illustrations.....	xiv
Chapter 1: Overview.....	1
1.1 Introduction.....	1
1.2 Global energy scenario	2
1.3 Harvesting of solar energy.....	3
1.4 Rate limiting factors	7
1.5 Novel catalyst for solar energy harvesting	9
1.6 Conclusion	10
Chapter 2: Semiconductor photocatalysis	11
2.1 Introduction.....	11
2.3 Photocatalysis	11
2.4 Basic principles of a semiconductor	13
2.5 Photoelectrochemical cells	14
2.6 Uses of semiconductor catalyst	18
2.7 Conclusion	25
Chapter 3: Synthesis of Semiconducting Porous Metal Oxides (POX)	27
3.1 Introduction.....	27
3.2 Synthesis of KTiNbO_5 and KNb_3O_8	27
3.3 Acid exchange of KTiNbO_5 and KNb_3O_8	30
3.4 Preparation of single lamellar sheet colloids: Exfoliation.....	32
3.5 Synthesis of Porous Metal Oxides.....	34
3.6 Topotactic dehydration	39
3.7 Conclusion	40

Chapter 4: Characterization of POX.....	41
4.1 Introduction.....	41
4.2 BET surface area analysis.....	41
4.3 X-ray diffraction analysis	47
4.4 UV-visible reflectance spectrometry	52
4.5 X-ray fluorescence spectrometry	53
4.6 Scanning electron microscopy	55
4.7 Transmission electron microscopy	56
4.8 ICP-OES analysis	62
4.9 Elemental analysis	63
4.10 Conclusion	63
Chapter five: Metal reduction and hydrogen production under UV light	64
5.1 Introduction.....	64
5.2 Experimental setup	64
5.3 Metal reduction	66
5.4 Hydrogen evolution	72
5.5 Influence of metal loading on H ₂ evolution.....	75
5.6 Influence of electron donor concentration on H ₂ evolution.....	77
5.7 Influence of metal deposition method on H ₂ evolution	78
5.8 Quantum efficiency of H ₂ evolution.....	79
5.9 Conclusion	80
Chapter six: Hydrogen production under visible light	81
6.1 Introduction.....	81
6.2 Experimental setup	81
6.3 Hydrogen evolution	84
6.4 Hydrogen evolution at different dye attachment methods.....	86
6.5 Dependence of metal loading on hydrogen evolution	88
6.6 Dependence of dye loading on hydrogen evolution	89
6.7 Dependence of electron donor on hydrogen evolution.....	90
6.8 Quantum efficiency of hydrogen evolution	91
6.9 Conclusion	93
Chapter seven: Concluding remarks	94
7.1 Introduction.....	94

7.2 Overall discussion.....	94
7.3 Experimental limitations.....	95
7.4 Future work.....	96
7.5 Conclusion	97
References.....	98
Vita	102

List of Tables

Table 2.1: Examples of TiO ₂ sensitized photosynthetic and photocatalytic processes ³	13
Table 2.2: Examples of different macrophotosynthetic electrochemical cells (after ref. 3).....	17
Table 2.3: Examples of semiconductor-sensitized systems for the photoreduction- (a), photo-oxidation (b) and photodissociation (c) of water (after ref. 3).....	20
Table 3.1 Masses of K ₂ CO ₃ , TiO ₂ and Nb ₂ O ₅ needed for preparation of KTiNbO ₅	28
Table 3.2 Masses of K ₂ CO ₃ , and Nb ₂ O ₅ needed for preparation of KNb ₃ O ₈	28
Table 3.3: Amounts of acid exchanged material and TBAOH used	33
Table 4.1: BET surface area measurements of POX materials	47
Table 4.2: ICP-OES analysis of metal oxide catalysts	62
Table 4.3: Elemental analysis of metal oxide catalysts	63
Table 6.1: Summary of quantum yields in visible light H ₂ evolution.	92

List of Figures

Figure 1.1: Growth of energy demand (2005-2030) ¹	2
Figure 1.2: Global energy consumption scenario ²	3
Figure 1.3: Available energy on earth surface.....	4
Figure 3.1: High temperature furnace.....	28
Figure 3.2: Stirring powders of KTiNbO_5 in acid solutions produces HTiNbO_5	31
Figure 3.3: Addition of TBAOH to HTiNbO_5 produces exfoliated individual sheets	33
Figure 3.4: Vapor precipitation of metal oxide sheets.....	35
Figure 3.5: Solvent exchange- (a) use of acetone and stirrer and (b) use of acetone, silica beads with a moderate heat.....	36
Figure 3.6: Supercritical point CO_2 chamber	38
Figure 3.7: Dried Porous Metal Oxides (POX) are very light-weight low density materials	39
Figure 4.1: Front view of ASAP2020 porosity system.....	42
Figure 4.2 Parameters for degassing the porous metal oxides in ASAP porosity system.	43
Figure 4.3: BJH desorption dV/dD pore volume graph of POX – HTiNbO_5	44
Figure 4.4: BJH desorption cumulative pore volume of POX – HTiNbO_5	44
Figure 4.5: BJH desorption dV/dD pore volume graph of POX – HNb_3O_8	45
Figure 4.6: BJH desorption cumulative pore volume graph of HNb_3O_8	45
Figure 4.7: Sample analysis in ASAP porosity system.	46
Figure 4.8: X-ray diffraction of parent material – KTiNbO_5	47
Figure 4.9: X-ray diffraction of unexfoliated material – HTiNbO_5	48
Figure 4.10: X-ray diffraction of POX – HTiNbO_5	48
Figure 4.11: X-ray diffraction of topotactic dehydrated materials – $\text{Ti}_2\text{Nb}_2\text{O}_9$	49
Figure 4.12: X-ray diffraction of parent material – KNb_3O_8	49

Figure 4.13: X-ray diffraction pattern of unexfoliated material – HNb_3O_8	50
Figure 4.14: X-ray diffraction pattern of POX – HNb_3O_8	50
Figure 4.15: X-ray diffraction pattern of topotactic dehydrated materials – Nb_6O_{15}	51
Figure 4.16: UV-VIS reflectance graph for HTiNbO_5	52
Figure 4.17: UV-VIS reflectance graph for HNb_3O_8	53
Figure 4.18: X-ray fluorescence image of POX- HTiNbO_5	54
Figure 4.19: X-ray fluorescence image of POX- HNb_3O_8	54
Figure 4.20: SEM image of POX- HTiNbO_5	55
Figure 4.21: SEM image of POX- HTiNbO_5	55
Figure 4.22: SEM image of POX- HNb_3O_8	56
Figure 4.23: TEM image of exfoliated colloidal HTiNbO_5 materials.	57
Figure 4.24: TEM image of exfoliated HNb_3O_8 materials.	58
Figure 4.25: TEM image of exfoliated colloidal HNb_3O_8 materials.	59
Figure 4.26: TEM image of exfoliated colloidal HNb_3O_8 materials.	60
Figure 4.27: TEM image of exfoliated colloidal HNb_3O_8 material at high magnification. An electron diffraction pattern is shown in the inset.....	61
Figure 5.1: Experimental setup for UV light assisted H_2 evolution and metal reduction.	65
Figure 5.2: Gas chromatograph setup for measuring evolved H_2	66
Figure 5.3: Metal reduction under UV light – (a) white POX materials before metal reduction, (b) dark grey POX materials after Pt reduction and (c) pink/red POX materials after Au reduction.	67
Figure 5.4: Kinetic study of Pt metal reduction under UV light	68
Figure 5.5: Kinetic study of Au metal reduction under UV light.....	69
Figure 5.6: SEM analysis of Au deposited HTiNbO_5 . (a) Au reduces without any preferences and (b) reduced gold particles grow and make nice facet.	70

Figure 5.7: (a) and (b) SEM analysis of Pt deposited HTiNbO ₅ . Pt prefers edges of the sheets.....	71
Figure 5.8: Calibration curve for evolved hydrogen gas measurement.....	72
Figure 5.9: Hydrogen evolution by HTiNbO ₅ materials under UV light	73
Figure 5.10: Hydrogen evolution by HNb ₃ O ₈ materials under UV light	74
Figure 5.11: Hydrogen evolution at different loading percentage of gold	75
Figure 5.12: Hydrogen evolution at different loading percentage of platinum	76
Figure 5.13: Effect of electron donor-EtOH amount in Pt deposited HNb ₃ O ₈ -POX system.....	77
Figure 5.14: Different methods of metal deposition in HNb ₃ O ₈ system.	78
Figure 6.1: Visible light experimental setup.....	82
Figure 6.2: Light emission spectrum from 75W xenon arc lamp	82
Figure 6.3: Chemical structure of N3 dye	83
Figure 6.4: Absorption spectrum of N3 dye at 50 μ molar concentration.....	83
Figure 6.5: Transmission spectrum of plastic filter used to block UV light from xenon arc lamp.	84
Figure 6.6: Hydrogen evolution in visible light by Au/Pt deposited HNb ₃ O ₈ materials.....	85
Figure 6.7: Hydrogen evolution in visible light by Au/Pt deposited HTiNbO ₅ materials.....	86
Figure 6.8: Hydrogen evolution at different dye attachment methods in 5% Pt loaded HNb ₃ O ₈ POX	87
Figure 6.9: Hydrogen evolution in HNb ₃ O ₈ POX materials at different Pt loading.....	88
Figure 6.10: Hydrogen evolution in HNb ₃ O ₈ POX materials at different Au loading	89
Figure 6.11: Hydrogen evolution in 5% Pt loaded HNb ₃ O ₈ POX at different dye concentrations	90
Figure 6.12: Hydrogen evolution in 0.5% Pt loaded HNb ₃ O ₈ POX at different amount of EtOH.....	91

List of Illustrations

Illustration 1.1: Schematic of dye sensitized watersplitting on porous TiO_2 film	7
Illustration 2.1: Change in the electronic structure of a semiconductor compound	14
Illustration 2.2: Major electronic processes occurring on a semiconductor particle following electronic excitation.....	15
Illustration 2.3: Energetics of a macrophotosynthetic cell for driving reaction	16
Illustration 2.4: Valence and conduction band positions for various semiconductors, and useful, relevant redox couples at pH 0.	18
Illustration 2.5: Valence schematic Illustration of the common form of typical systems	21
Illustration 2.6: Energetics and major general processes for the photo-oxidative mineralization of organic pollutants in aqueous solution by dissolved oxygen, sensitized by semiconductor particles.....	22
Illustration 3.1: Block diagram showing the synthesis process of porous metal oxides (POX).....	27
Illustration 3.2: Schematic of temperature program for heating ingredients in the furnace.....	29
Illustration 3.3 KTiNbO_5 and KNb_3O_8 have layered structures with exchangeable cations	30
Illustration 3.4: Acid base neutralization reactions between HNb_3O_8 and TBAOH	32
Illustration 3.5: (a) shows exfoliated colloidal single sheets and	34
(b) shows exposure to acid vapor makes sheets precipitate.	34
Illustration 3.6: Phase diagram of carbon dioxide	37
Illustration 5.1: Au metal reduction under UV light.....	67

Chapter 1: Overview

1.1 Introduction

With the overall improvement of human lifestyle on earth, we have developed a strong dependence on technology and the availability of many services. As a consequence our global energy consumption is always increasing. Electric Power generation continues to be the fastest-growing energy-demand sector, and global demand is expected to increase by 50 percent to 124 MBDOE (Million Barrels per Day of Oil-Equivalent) in 2030.¹ MBDOE provides a standardized unit of measure for different types of energy sources (oil, gas, coal, etc.) based on energy content relative to a typical barrel of oil. One MBDOE is enough energy to fuel about 3 percent of the vehicles on the world's roads today. Approximately 80 percent of that growth will be in rapidly developing countries such as China. Transportation demand will grow by 40 percent to close to 62 MBDOE by 2030, even with significant vehicle-efficiency gains around the world. As with power generation, nearly all of the incremental demand will come from developing nations. The industrial and residential/commercial sectors will grow at a relatively slower pace. Industrial demand will increase by 28 percent to almost 85 MBDOE, and residential/commercial demand will rise 10 percent to 40 MBDOE (Figure 1). In total, global energy-demand growth is expected to average 1.2 percent per year in 2005-2030, growing from roughly 230 MBDOE or 15 trillion watts to 310 MBDOE or 22 trillion watts.¹

In the early 1970's global energy consumption was 3 trillion watts and in 2008 this number grew to 16 trillion watts.² About 37% of the global energy used comes from oil, 26% from coal, 23% from gas, 7% from nuclear power and just 6% from renewable fuel (Figure 2).² However, the use of non renewable fossil fuel has had a great impact on the global environment. Global warming and climate change is a very important problem today. Rising sea levels, retreating glaciers, the disappearance of polar ice caps, and altered patterns of agriculture are cited as direct consequences of global warming. Predictions for secondary and regional effects include extreme weather events, an expansion of tropical

diseases, changes in the timing of seasonal patterns in ecosystems, and drastic economic impact.² So, there exists a great need for developing low cost renewable clean energy sources.

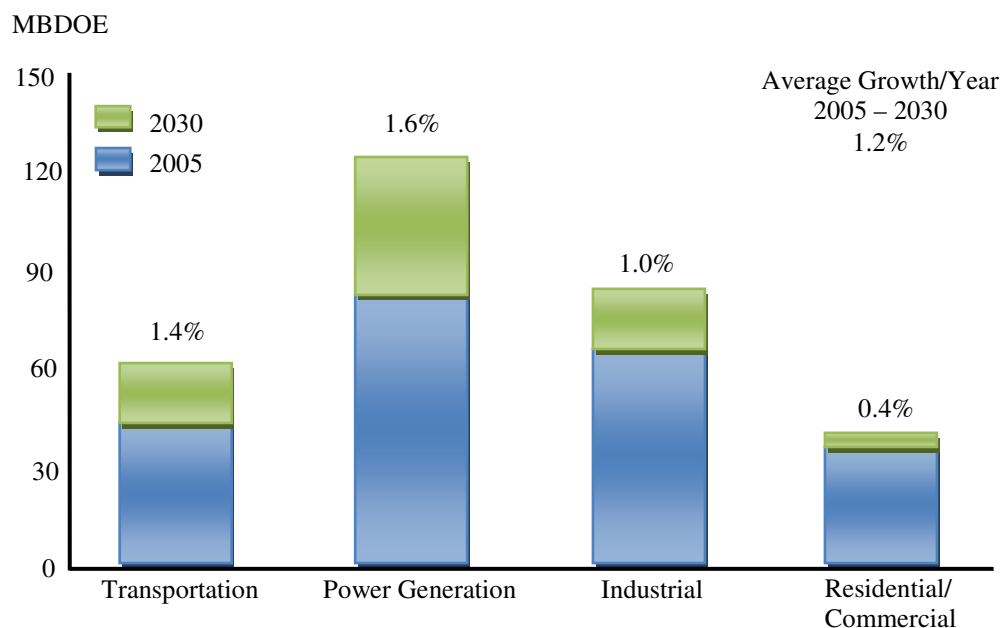


Figure 1.1: Growth of energy demand (2005-2030)¹

1.2 Global energy scenario

The main source of most renewable energy sources is the sun. In comparison to the global demand of 15 trillion watts of energy, there are 89,000 trillion watts of solar energy and 370 trillion watts of wind energy available on the earth's surface (Figure 3).² There are a variety of technologies that have been developed to take advantage of solar energy. One is photovoltaics (solar cells), which convert solar energy into electricity and the another one is inorganic photocatalysts that have the potential to be less expensive than photovoltaic systems, which need to be coupled with batteries or water electrolyzer systems in order to store solar energy. The photo conversion efficiencies of inorganic systems that directly convert solar energy into energy rich chemicals, such as hydrogen via water photolysis, are presently too low for practical systems.^{3,5-6} Consequently, there still remains a great interest in trying to improve inorganic photocatalytic systems.

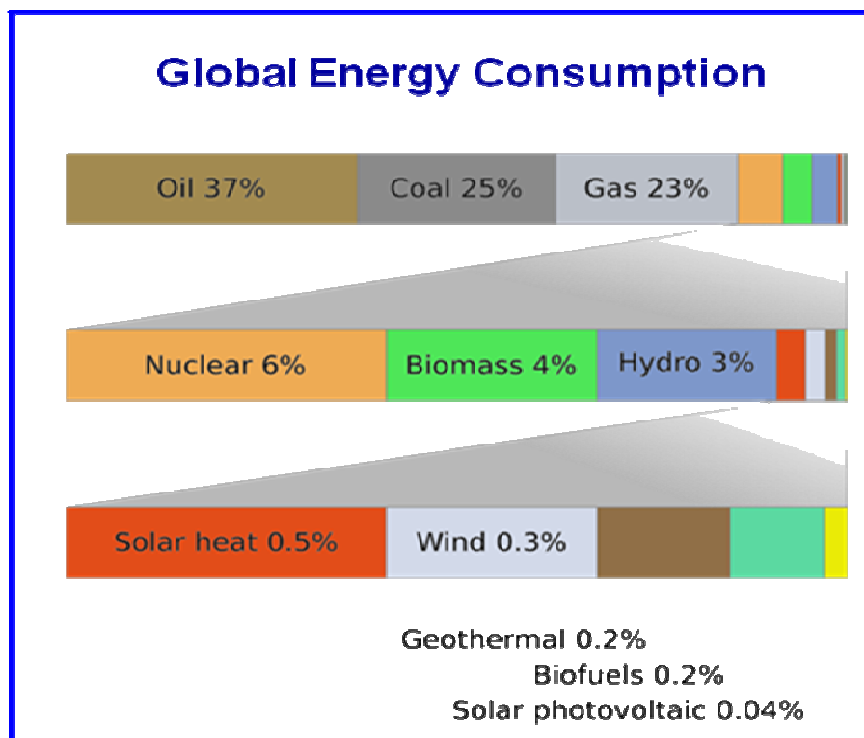
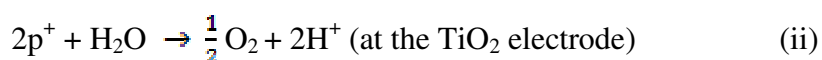


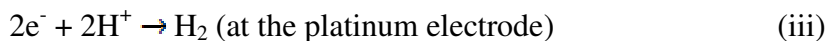
Figure 1.2: Global energy consumption scenario²

1.3 Harvesting of solar energy

In 1972 Fujishima and Honda discovered the photosensitization of a TiO_2 electrode for the electrolysis of water into H_2 and O_2 and recorded a 0.1% quantum efficiency for H_2 production.⁵ Since then, water photolysis by TiO_2 semiconductors have received significant attention and have been widely studied to convert solar light energy into useful chemical energy.⁶⁻¹⁰ Thirty two years after the discovery by Fujishima and Honda, in the year 2004, Takabayashi recorded a 10% solar to chemical conversion of H_2 using Si/TiO_2 composite electrode.²⁹ Numerous researchers around the world are striving to make an efficient process of solar H_2 production with economic feasibility.

The schemes of electrochemical photolysis of water molecules presented by Fujishima and Honda are as follows:





The overall reaction is:

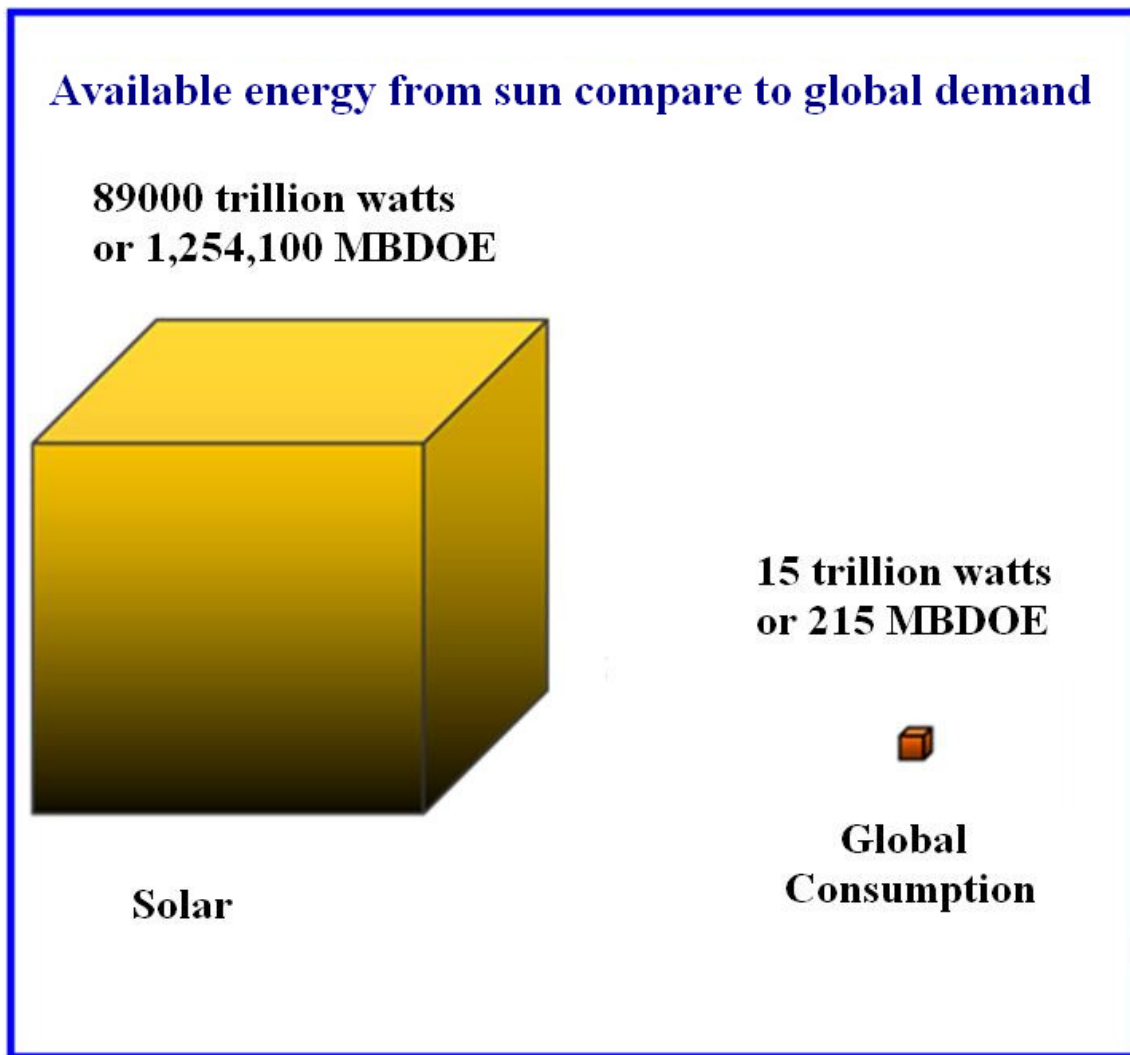
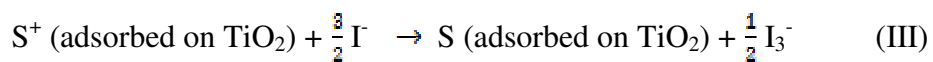
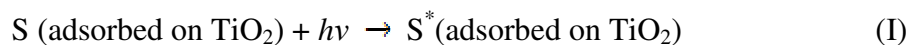


Figure 1.3: Available energy on earth surface

A new generation of solar cells, called dye sensitized solar cells, has been developed as an alternative to the conventional silicon based solar cells.⁶ In these cells, sensitizing dyes and mesoporous titania films are the two key components for high power-conversion efficiencies. Different ruthenium dye complexes containing anchoring groups, such as carboxylic acid, phosphonic acid, sulphonic, thiocyno, and dihydroxy on pyridine ligands, have been used as dyes.¹⁰ The anchoring groups adsorb

the dye on the nanocrystalline TiO₂ surface. The immobilized ruthenium sensitizing dye absorbs a photon from light energy to produce an excited state (state I), which transfers its electron efficiently into the TiO₂ conduction band (state II). The oxidized dye is subsequently reduced by electron donation from an electrolyte, the iodide/triiodide redox system (state III). The injected electron flows through the semiconductor network to arrive at the anode and then through the external load to the counter electrode (cathode). At the counter electrode, reduction of triiodide in turn regenerates iodide (state IV), which completes the circuit. Originally the major drawback of these dye sensitized solar cells was very low conversion efficiencies (less than 0.5%).⁷ It was partly because of the low absorbance of a single monolayer of dye on a plane surface of a semiconductor. The report of O'Regan and Grätzel in 1991 was the major breakthrough in this field which overcame this problem by use of a nano structured TiO₂ semiconductor.⁶ Because of the large surface area and high porosity of the nano structured TiO₂ film, a monolayer of dye adsorbed onto the porous TiO₂ surface is sufficient to collect a large part of the incident light. This property led to the enhancement of the light harvesting capacity of the dye-TiO₂ system and consequently to the high efficiency of the cell.⁶

Schemes of electricity generation in solar cell presented by Nazeeruddin and Grätzel⁷ are as follows:



where S is doping TiO₂, is another technique to make TiO₂ visible light sensitive. There are many reports of scientists where they chemically modified white TiO₂ with a colored complex so that the solar energy can be absorbed and converted into chemical energy. The chemical modifications of the TiO₂

composites are being done with polyaniline, adsorbing Fe^{3+} cations onto S- or N-doped TiO_2 , codoping C^{4+} and S^{4+} in rutile TiO_2 , polycrystalline Si doped with TiO_2 .¹⁰⁻¹⁸

Nano crystalline TiO_2 films can also be used for the generation of hydrogen. Using UV light these wide band gap semiconductor materials can be used to photo-split water into H_2 and O_2 . Visible light can also be used with these semiconductors in combination with special dye sensitizer molecules, which may enable H_2 production using natural sunlight. There are different ways of making TiO_2 films.⁷⁻¹⁴

A key aspect of effective, next-generation solar energy technology is the ability to synthesize films with controlled morphology. It has been reported that crystalline structures oriented normal to the substrate have superior performance relative to irregular disordered structures.⁷ Dye sensitized solar cells rely on a nanostructured interpenetrating interface between an electron-conducting layer (TiO_2 or ZnO), a light absorbing layer (Ru based dye), and a hole conducting layer (redox electrolyte or hole conducting polymer) to generate and separate charge.⁶⁻⁷ The electron conducting TiO_2 layer serves two important functions. First it provides a large surface area onto which the light absorbing agent is immobilized, while maintaining the short transport distances to the substrate. Second, the TiO_2 conducts electrons generated by light absorbing layer to the substrate where they are collected. Similarly, surface area, electron transport, and photo electron lifetime are the critical factors in dye-sensitized TiO_2 system. Control over morphology is very critical, as it can be used to optimize conversion efficiency. However, the morphology is ultimately determined by the synthesis process of TiO_2 nanostructure.

A variety of synthesis techniques have been employed to synthesize TiO_2 films. These synthesis methods include: thermal oxidation and anodization of titanium foils, dip-coating, screen-printing, sol-gel processes, sputtering, spray-pyrolysis, and chemical vapor deposition among others. High performance film morphologies can be obtained through these processes, but the synthesis is either difficult to control or involves multiple time consuming steps or the use of expensive processing

equipments. The use of such time consuming and expensive processing is undesirable for the widespread industrial production of films that would be required to harvest a meaningful amount of solar energy. There is a need for a robust, inexpensive synthesis process to fabricate high performance materials that provide rational control over morphology.

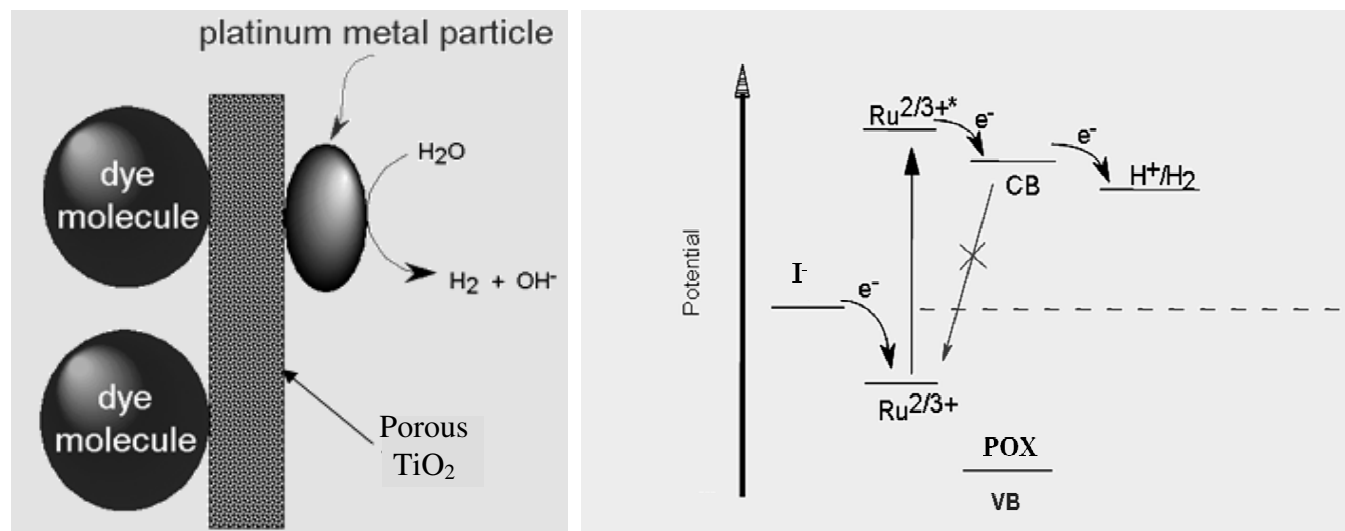


Illustration 1.1: Schematic of dye sensitized watersplitting on porous TiO₂ film (left) and energy level diagram of the system (right).

1.4 Rate limiting factors

The photoconversion efficiency of solar energy to chemical energy, such as hydrogen energy by water photolysis, is too low to use practically. In fact the efficiency limiting factors, such as light absorption efficiency (either by the use of photosensitizer or chemical modification of semiconductor by doping), electronic conduction in the framework, recombination of electrons and holes and availability of electrons at the proton reducing sites, needs to be resolved. With a suitable design of experimental setup, good light source, utilization of dye sensitizer or chemical doping, people have made significant gains in visible light photo absorption activity. However, poor electronic conduction contributed to a less success that was assumed. This is mostly because of the defects of nanostructure materials, which lead recombination reactions of photoelectron-hole (e^-/h^+) charge pairs. In the recombination process,

photo electrons and holes that are created for the purpose of driving a desired chemical reaction are lost, when instead they recombine with each other, thus producing only thermal energy.²² Optimizing photocatalysts by reducing recombination reactions remains a major challenge.

The problem of charge recombination is exacerbated by the existence of charge trap sites in the semiconductor photocatalytic material. Therefore, it is logical to conclude that a catalyst's efficiency might be improved by reducing the number of possible traps in the catalyst material. Potential trap sites can generally be defined as any discontinuity in the nature or structure of a material. Such discontinuities, such as grain boundaries, impurities, dislocations, vacancies, surface states, etc., act as sticking points on which mobile electrons or holes can localize and hence stop their movement through a material.³⁴ On average, the lack of e^-/h^+ movement decreases the separation distance between charge pairs and increases the probability that an electron will find a hole, and vice versa. The lifetime of the charge separated state is therefore a vital parameter, because time is needed for electrons or holes to find a suitable reaction sites on the surface and complete a desired reaction. If no reaction site is found in that lifetime, then charge recombination is inevitable. A longer charge separation lifetime improves the odds of success for completing an intended reaction, such as the production of energy-rich chemicals like hydrogen.

Distance has the same effect as time. In other words, if photo electrons and holes are forced to travel too far in the photocatalyst before they are able to find a productive reaction site on the surface, then again, charge recombination is inevitable. Therefore, shortening the distance (and hence time) that charges must travel to find suitable reaction sites on the semiconductor surface should improve catalyst performance. One possibility for improving reaction efficiencies includes increasing the density of suitable reactions sites on the surface that electrons and holes participate in, and therefore increasing the probability of a productive encounter. Another way to extend this distance is to decrease the density of trap sites in the material. In heterogeneous catalysis involving semiconductors, desired reactions

generally occur at the surface of the material, at the interface between a solid, a liquid, and sometimes also a gas. Therefore, electrons and holes must access the material's surface to be able to participate in meaningful chemical reactions. A significant fraction of photons penetrate deep into the bulk of a semiconductor, where they produce electrons and holes. To be useful, photo initiated electrons and holes must travel to the material's surface. That distance traveled may be greater than the debye length of the charge pair, and recombination is therefore likely, and hence those photons do not produce useful products and there is a loss of efficiency.³⁴

When particle dimensions are close to or less than the debye length of a semiconductor, then quantum efficiencies should improve, as the electrons and holes can reach and sample more of the semiconductor surface, where they can react with other species. Indeed, there have been numerous reports where the photo activity of nano powders appears to be better than bulk powders, on a mass basis (from higher surface to volume ratios) and on a surface area basis (greater activity per unit surface area).² The differences in catalytic character due to the differences in morphology (i.e. more exposed crystal edges, greater roughness, etc.) between nano powders and bulk powders may also play a role. Photocatalytic materials with nanometric dimensions (<50 nm) and low trap site densities hold promise for improving photochemical energy conversion.

1.5 Novel catalyst for solar energy harvesting

HTiNbO₅ porous oxide and HNb₃O₈ porous oxide, two new wide band gap semiconducting nanocomposites are being developed to address the need for new materials that are wide band gap semiconductors, have high surface area, are stable, and have good electronic characteristics. These materials are synthesized via a low-temperature synthetic route and are crystalline. Most porous materials are made in their amorphous states and change from their amorphous states to crystalline solids during heating. These changes often result in pore collapse, loss of structural integrity, and diminished surface areas. The new composite materials have a unique structure that is porous with pore

walls that are crystalline and the pore sizes are large sometimes, many over 20 nm in diameter. This highly crystalline nature of the new material holds promise as a way to improve photocatalytic efficiency in inorganic photochemical energy conversion and treatment of contaminated water supply. The details of the synthesis process will be discussed in later chapter. The dried porous catalysts used in the research here are called as POX, or porous oxides.

1.6 Conclusion

The long term goal of this research is to find a cost-effective way of generating H_2 by photo splitting water molecules. H_2 will act as an energy vector in a renewable energy scheme, which will eventually reduce the consumption of fossil fuels. The first step of the research is to develop and characterize wide band gap semiconductors with porous structures as catalysts. Then, the second step is to test how the catalysts perform in metal ion reductions from solution. The third step is to test the new materials with metallic co-catalysts like Pt for their ability to produce H_2 from H_2O . The fourth and final step of the research is to attempt to reduce water molecules into hydrogen in presence of only visible light by using photosensitizer with the catalysts. The second chapter of this dissertation discusses briefly semiconductor photocatalysis, an explanation of their working principles, and achievements and future promises. The third and fourth chapters explain the synthesis processes of the new semiconductor catalysts and their characterization techniques respectively. The fifth and sixth chapters present the research findings and a discussion of them. The seventh chapter is the concluding remarks, future goals and shortcomings of the projects etc.

Chapter 2: Semiconductor photocatalysis

2.1 Introduction

This chapter will give an overview of the field of semiconductor photocatalysis: a brief explanation of theories, achievements and possible future. The semiconductor titanium dioxide (TiO_2) features predominantly in past and present work of semiconductor photocatalysis; as a result, TiO_2 is used in most of the examples selected to illustrate various points.

2.3 Photocatalysis

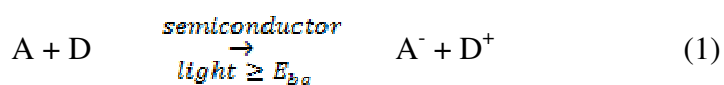
Photocatalysis refers to acceleration of a photoreaction by the presence of a catalyst. The term "photoreaction" is sometimes elaborated on as a "photoinduced" or "photoactivated" reaction, all to the same effect. The above definition of "photocatalysis" includes the process of "photosensitization", i.e. a process by which a photochemical alteration occurs in one chemical species as a result of the initial absorption of radiation by another chemical species called the photosensitizer. Heterogeneous photocatalysis involves photoreactions which occur at the surface of a catalyst. If the initial photoexcitation process occurs in an adsorbate molecule, which then interacts with the ground state of the catalyst substrate, the process is referred to as a "catalyzed photoreaction", if, on the other hand, the initial photoexcitation takes place in the catalyst substrate and the photoexcited catalyst then interacts with the ground state adsorbate molecule, the process is a "sensitized photoreaction". In most cases, heterogeneous photocatalysis refers to semiconductor photocatalysis or semiconductor-sensitized photoreactions.

It is sometimes argued that the term "catalysis" should not be used unless it has been demonstrated that the turnover number (TN) for the process (i.e. the number of product molecules per number of active sites) is greater than unity; if this is not demonstrated, the term "heterogeneous (or semiconductor)-assisted photoreaction" should be used. In most examples of heterogeneous

photocatalysis, the value of TN has not been demonstrated to be greater than unity because of the difficulty in determining the number of active sites on irradiation.

When titanium dioxide is used as the semiconductor, it is sometimes assumed that the number of active sites can be taken as the product of the surface density of OH⁻ groups (typically 10²-10¹⁵ cm⁻²) and the specific surface area of TiO₂. However, the latter parameter is usually measured using the powder in the dry state (the Brunauer-Emmett-Teller (BET) surface area), and the actual surface area of the TiO₂ photocatalyst dispersed in solution will depend on the degree of aggregation. In addition, it does not follow that all the surface sites occupied by the OH⁻ groups will be necessarily active. These approximations are likely to lead to a value for TN which is lower than the actual value; thus, if by carrying out such calculations it can be shown that TN is still greater than unity, it appears reasonable to assume that the process under examination is a "catalyzed", rather than "assisted", reaction. For most research conducted in the area of semiconductor-assisted photoreactions, it is assumed that the process under study is an example of semiconductor-sensitized heterogeneous photocatalysis, especially if it can be shown, or it is known, that there is no evidence of a marked loss in semiconductor photoactivity with extended use.

The overall process of semiconductor sensitized photoreactions can be summarized as follows:



where E_{bg} is the bandgap of the semiconductor. If, in the absence of semiconductor and light of energy greater than or equal to E_{bg}, ΔG° for reaction (1) is negative, the semiconductor-sensitized photoreaction is an example of photocatalysis. Alternatively, if ΔG° for reaction (1) is positive, the semiconductor-sensitized photoreaction is an example of photosynthesis. Reported examples of the two different semiconductor-sensitized photoreactions are given in Table 2.1.

Table 2.1: Examples of TiO₂ sensitized photosynthetic and photocatalytic processes³

Reaction $A + D \rightarrow A^- + D^+$	Description	ΔG° (kJ/mol)
Photosynthesis		
$H_2O + H_2O \rightarrow 2H_2 + O_2$	Water splitting	475
$2CO_2 + 4H_2O \rightarrow 2CH_3OH + 3O_2$	Carbon dioxide reduction	1401
$2N_2 + 6H_2O \rightarrow 4NH_3 + 3O_2$	Nitrogen reduction	1355
$6CO_2 + 6H_2O \rightarrow C_6H_{12}O_6 + 6O_2$	Green plant photosynthesis	2895
Photocatalysis		
$3O_2 + 2CH_3OH \rightarrow 4H_2O + 2CO_2$	Methanol mineralization	-1401
$2HAuCl_4 + CH_3OH + H_2O \rightarrow 2Au + 8HCl + CO_2$	Deposition of precious metals	
$6H_2O + C_6H_{12}O_6 \rightarrow 12H_2 + 6CO_2$	Biomass conversion to hydrogen	-32

2.4 Basic principles of a semiconductor

As indicated in illustration 2.1, for many compounds, as the number N of monomeric units in a particle increases the energy necessary to photoexcite the particle decreases. In the limit when the $N \gg 2000$, it is possible to end up with a particle which exhibits the band electronic structure of a semiconductor in which the highest occupied band (the valence band) and lowest unoccupied energy band (the conduction band) are separated by a bandgap E_{bg} , a region devoid of energy levels in a perfect crystal.

Illustration 2.2 shows that activation of the semiconductor photocatalyst for reaction (1) is achieved through the absorption of a photon of ultra-bandgap energy, which results in the promotion of an electron e^- from the valence band to the conduction band, with the concomitant generation of a hole h^+ in the valence band. For a semiconductor photocatalyst to be efficient, the different interfacial electron processes involving e^- and h^+ , i.e. reactions (c) and (d) in illustration 2.2 must compete

effectively with the major deactivation processes involving e^- and h^+ recombination, i.e. reactions (a) and (b) in illustration 2.2. Electron-hole recombination can occur at the surface (reaction (a)) or in the bulk (reaction (b)) of the semiconductor. At the surface of the particle, photogenerated electrons can reduce an electron acceptor A (reaction c) and photogenerated holes can oxidize an electron donor D (reaction (d)). The combination of reactions (c) and (d) represents the semiconductor sensitization of the general redox reaction (1).

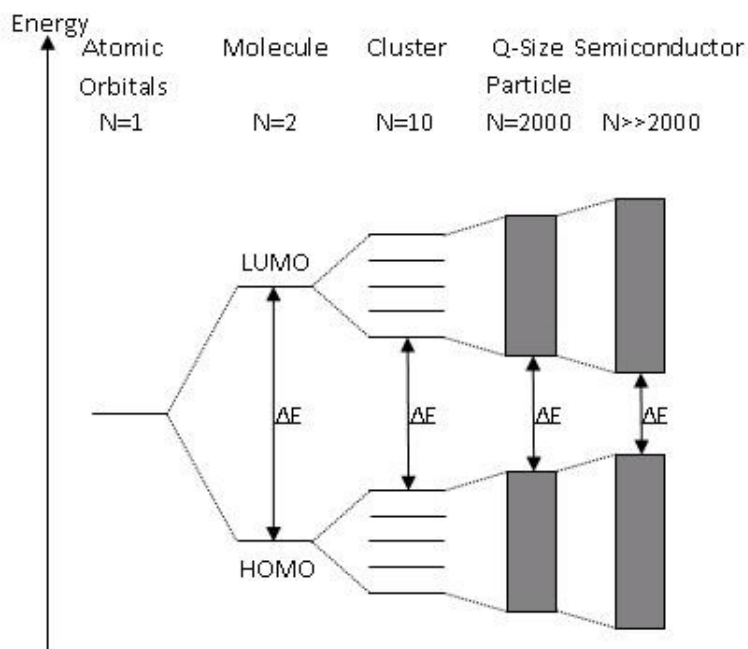


Illustration 2.1: Change in the electronic structure of a semiconductor compound as the number N of monomeric units present increases from unity to clusters of more than 2000 (after ref. 3).

2.5 Photoelectrochemical cells

As indicated in Illustration 2.2, e^-/h^+ pairs can be generated in a semiconductor by the absorption of light of energy greater than or equal to E_{bg} . In an n-type semiconductor immersed in solution, an electric field forms spontaneously at the semiconductor-electrolyte interface; e^-/h^+ pairs generated in the region of the electric field, i.e. the space-charge region, are separated efficiently, rather than undergoing recombination. As a consequence, in an n-type semiconductor, the photogenerated electron moves into

the bulk of the semiconductor, where it can be transferred either through a wire to a second, non-photoactive electrode (such as Pt) or through a surface site to a point where an electron acceptor A can be reduced, e.g.

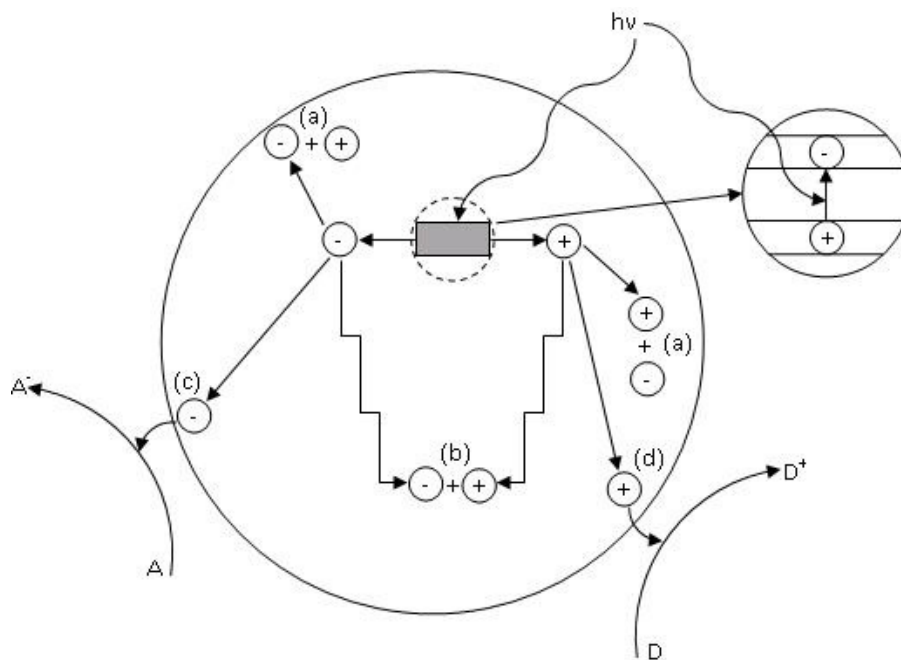


Illustration 2.2: Major electronic processes occurring on a semiconductor particle following electronic excitation.

In the meantime, the photogenerated hole, under the influence of the electric field, migrates towards the surface of the semiconductor to a surface site where it can oxidize a suitable electron donor D, e.g.



The energetics of such a macrophotoelectrosynthetic cell for driving reaction (1) are shown in illustration 2.3, and Table 2.2 lists some examples. From thermodynamic considerations, if the photogenerated electron in the conductance band can reduce water, the potential of the band (E_{CB}) must be less than $E(H^+/H_2)$; it also follows that, if the photo generated hole in the valence band can oxidize water, E_{VB} must be greater than $E(O_2/H_2O)$. Illustration 2.4 shows the band positions of various

semiconductors, including rutile and anatase TiO_2 and SrTiO_3 , and the redox potentials of relevant redox couples.

The first photoelectrochemical cell for water splitting, i.e. $2\text{H}_2\text{O} \rightarrow 2\text{H}_2 + \text{O}_2$ (see Table 2.1), was reported by Fujishima and Honda in 1972 using a rutile TiO_2 photoanode and Pt counter electrode. This work came at a time when there was increasing interest in developing artificial systems capable of converting solar to chemical or electrical energy. Such work was given greater impetus with the oil crisis of 1973, and it arose a substantial research effort into photoelectrochemical cells for water splitting and electricity production.

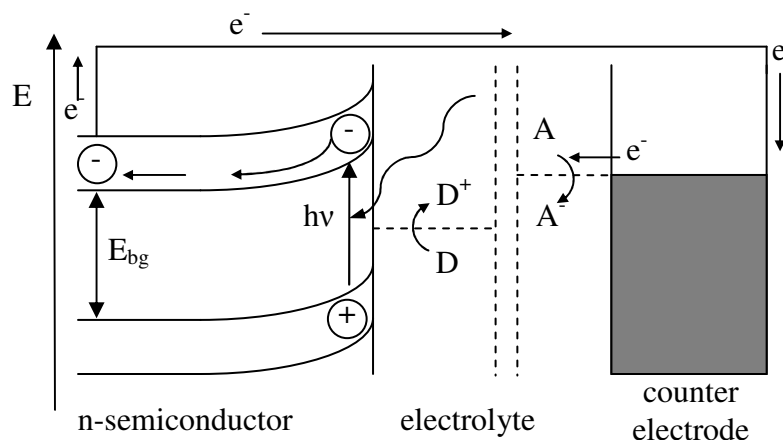


Illustration 2.3: Energetics of a macrophotosynthetic cell for driving reaction (1); in such a reaction, $\Delta G^\circ > 0$.

It is not often recognized that the Fujishima and Honda $\text{TiO}_2/\text{H}_2\text{O}/\text{Pt}$ photoelectrochemical cell requires a degree of chemical or electrical bias to make it work. This is not surprising given that E_{CB} (TiO_2 ; rutile) is approximately 0.2 V more positive than $E(\text{H}^+/\text{H}_2)$ (Illustration 2.4). Indeed, it appears likely that the original short-circuit photocurrents observed in the Fujishima and Honda $\text{TiO}_2/\text{H}_2\text{O}/\text{Pt}$ photoelectrochemical cell corresponded to the oxidation of water to oxygen at the TiO_2 photoanode, but not the concomitant reduction of water to hydrogen at the Pt-black cathode, rather the reduction of dissolved oxygen and/or some electrolyte impurity; alternatively, these workers may have used a chemical bias (alkali in the TiO_2 photoanode half-cell and acid in the Pt cathode half-cell) which was not

mentioned in their original paper. In contrast, Wrighton et al. were able to show subsequently that the SrTiO₃/H₂O/Pt photoelectrolysis cell worked with no bias and with a 25% efficiency with respect to UV photons ($E_{bg} = 3.2$ eV; $\lambda(\text{threshold}) = 388$ nm), but only 1% solar energy conversion efficiency η , since the proportion of UV light in the solar spectrum is very low (less than 5%). The reason for the success of the latter cell, compared with the Fujishima and Honda cell, is that in SrTiO₃, unlike rutile TiO₂, E_{CB} and E_{VB} straddle the hydrogen and oxygen evolution potentials, i.e. $E(H^+/H_2)$ and $E(O_2/H_2O)$ respectively (Illustration 2.4). Although other n-type oxide semiconductors have been used as photoanodes for the photoelectrolysis of water, the inappropriate disposition of the conductance and valence bands and/or a bandgap, which is too large, makes these materials less than ideal for use in efficient solar photoelectrolysis cells. In addition, it is generally accepted that there is not a single non-oxide, n-type semiconductor which has been shown to be capable of sustaining the oxidation of water to oxygen when illuminated with ultra-bandgap light; all such semiconductors show a tendency towards photoanodic corrosion. In the case of p-type semiconductors, which are much rarer in nature, the bandgaps are usually too small and most suffer serious stability problems. As a result, p-type semiconductors are rarely used in semiconductor photocatalysis.

Table 2.2: Examples of different macrophotosynthetic electrochemical cells (after ref. 3)

Semiconductor photoelectrode	Reaction $A + D \rightarrow A^- + D^+$	E_{bg} (eV)
n-TiO ₂	$H_2O + H_2O \rightarrow 2H_2 + O_2$	3.0
n-SrTiO ₃	$H_2O + H_2O \rightarrow 2H_2 + O_2$	3.2
n-MoSe ₂	$SO_2 + 2H_2O \rightarrow H_2SO_4 + H_2$	1.09
p-GaAs	$2N_2 + 6H_2O \rightarrow 4NH_3 + 3O_2$	2.3
p-GaAs	$2CO_2 + 4H_2O \rightarrow 2CH_3OH + 3O_2$	2.3

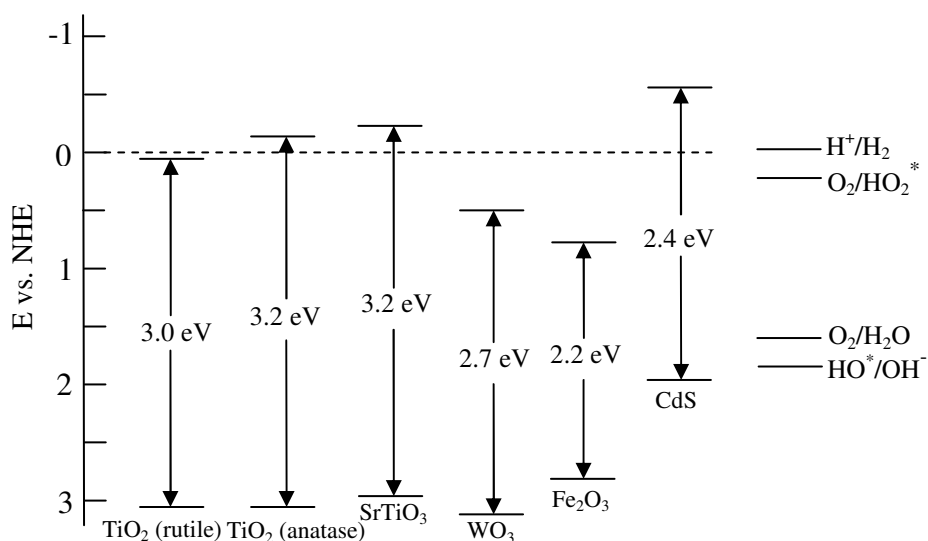


Illustration 2.4: Valence and conduction band positions for various semiconductors, and useful, relevant redox couples at pH 0. In order to photoreduce a chemical species, the conduction band of the semiconductor must be more negative than the reduction potential of the chemical species; to photooxidize a chemical species, the potential of the valence band of the semiconductor must be more positive than the oxidation potential of the chemical species.

2.6 Uses of semiconductor catalyst

As mentioned above semiconductor catalysts have been used in various experiments for various applications and a lot of promising outcomes have occurred worldwide.¹⁵⁻²⁰ Different aspects of semiconductor catalysts are discussed here briefly.

2.6.1 Semiconductor particles as sensitizers for water reduction, oxidation or dissociation

Schematic Illustrations of the mechanisms by which an n-type semiconductor is able to photosensitize the reduction, oxidation or cleavage of water are given in Illustration 2.5(a)-(c) respectively. A platinum group metal (PGM) redox catalyst, such as Pt, deposited on the surface of the semiconductor is invariably used to facilitate the reduction of water by the photogenerated electrons. Although a PGM oxide, such as RuO_2 , is often used to mediate the oxidation of water by the photogenerated holes, this is often unnecessary when the semiconductor is a large bandgap metal oxide,

such as TiO_2 , since $E_{\text{VB}} \gg E(\text{O}_2/\text{H}_2\text{O})$ (Illustration 2.4), i.e. there is a sufficiently large overpotential for the reaction to proceed readily without an oxygen redox catalyst. Table 2.3 provides some examples of the semiconductor-sensitized systems for water photoreduction (incorporating a sacrificial electron donor), water photo-oxidation (incorporating a sacrificial electron acceptor) and water photodissociation.

There is no doubt that it is possible to use semiconductors to sensitize the photoreduction and photo-oxidation of water through the use of sacrificial electron donors and acceptors respectively. The photocleavage of water is another matter. Most research groups have had to resort to using large bandgap metal oxide semiconductors, such as anatase TiO_2 , or SrTiO_3 , and forcing conditions of high temperature and/or reduced pressure to observe both hydrogen and oxygen generation. The early reports of a "bifunctional catalyst", $\text{RuO}_2/\text{TiO}_2/\text{Pt}$, which photocleaved water efficiently ($\Phi(\text{H}_2) = 0.3$ was reported; presumably $\Phi(\text{O}_2) = 0.15$, but the latter is usually not observed under ambient conditions, remain unsubstantiated and, with hindsight, doubtful.⁹ Indeed, it has now been suggested that any oxygen observed on irradiation of the $\text{RuO}_2/\text{TiO}_2/\text{Pt}$ bifunctional catalyst probably "leaked in from outside". The claims that CdS can be used as a sensitizer for the photocleavage of water are highly dubious given the well-recognized tendency of CdS to undergo photoanodic corrosion; certainly a number of major research groups have failed to reproduce these findings. All the semiconductors listed in Table 2.3 are excellent sensitizers for the photoreduction of oxygen; it seems most likely that, under ambient conditions, if the photodissociation of water does occur it will not be sustainable, since any oxygen generated will be photoreduced and so short circuit the overall process.

It is worth making the following general points about semiconductor-sensitized systems for water photocleavage. Clearly, the observation of hydrogen evolution alone in such systems does not imply water cleavage and the concomitant generation of a stoichiometric amount of oxygen must not be assumed. Great care must be taken when working on such systems, since hydrogen can be photogenerated using most semiconductors if a sacrificial electron donor is present; likely sources of this

sacrificial agent include electron donors, such as methanol or formaldehyde, used in the deposition of the PGM redox catalyst onto the surface of the semiconductor (repeated washing of such a treated photocatalyst does not ensure that all the electron donor is removed) and any polymer support used if the semiconductor is in colloidal form. Even the observation of the evolution of oxygen can be the result of air leaks; the oxygen/nitrogen ratio must not be taken as a guide to assess how much of the oxygen observed is photogenerated. With all of these problems, it follows that many of the reports on semiconductor particlesensitized systems for water cleavage should be viewed with a high degree of skepticism. A sustainable, reproducible, semiconductor particle-based sensitized system for water cleavage is still to be achieved.

Table 2.3: Examples of semiconductor-sensitized systems for the photoreduction- (a), photo-oxidation (b) and photodissociation (c) of water (after ref. 3)

Semiconductor-sensitized systems for the photoreduction of water (a)			
Semiconductor	Sacrificial donor	Hydrogen catalyst	$\Phi(\text{H}_2)$
TiO ₂	Biomass (including grass, wood, algae, seaweed)	Pt (4%)	0.02-0.004
TiO ₂	Methanol, propanol	Pt (10%-0.05%)	-
TiO ₂	EDTA	Pt (0.1 %-2%)	0.03
CdS	EDTA	Pt	-
CdS	S ²⁻	RuO ₂ .xH ₂ O	-

Semiconductor-sensitized systems for the photo-oxidation of water (b)			
Semiconductor	Sacrificial acceptor	Oxygen catalyst	$\Phi(\text{H}_2)$
TiO ₂	Fe(III) ions	None, or Rh, Ru, Ir, Au, Co	-
TiO ₂	[PtCl ₆] ²⁻	None	-
WO ₃	Fe(III) ions	None, or Pt, Rh, Ru,	0.03
CdS	[PtCl ₆] ²⁻	RuO ₂ .xH ₂ O Pt	-
CdS	[PtCl ₆] ²⁻	RuO ₂ .xH ₂ O	-

Semiconductor-sensitized systems for the photodissociation of water (c)			
Semiconductor	Hydrogen catalyst	Oxygen catalyst	$\Phi(\text{H}_2)$
TiO_2	Pt	None	-
TiO_2	Pt	$\text{RuO}_2 \cdot x\text{H}_2\text{O}$	0.3
SrTiO_3	Pt, Ir, Pd, Os, Ru, Re or Co	None	-
TiO_2	Pt	None	-
CdS	Pt	$\text{RuO}_2 \cdot x\text{H}_2\text{O}$	0.005
CdS	Pt, Rh or Ir	$\text{RuO}_2 \cdot x\text{H}_2\text{O}$ with $[\text{Ru}(\text{OH})(\text{EDTA})_2\text{O}_2]$	-

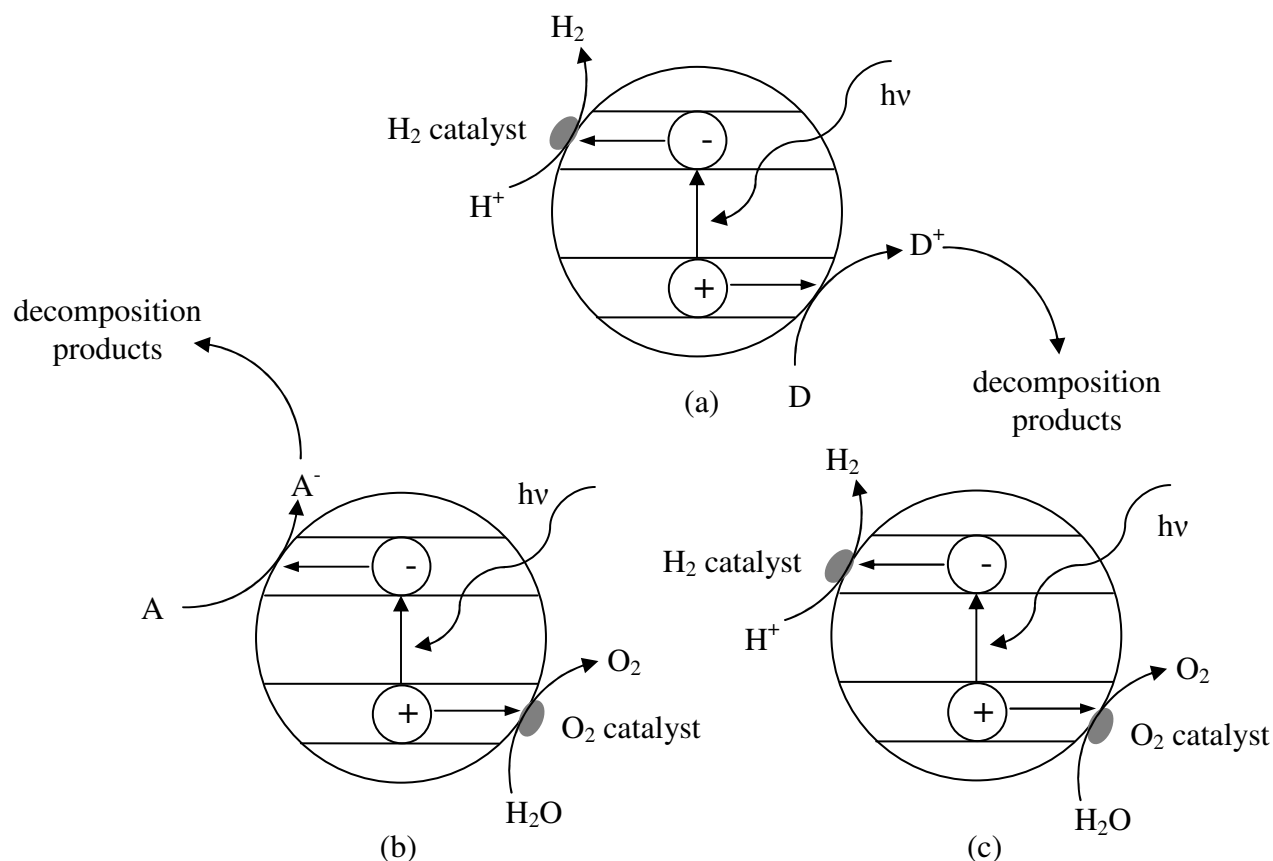


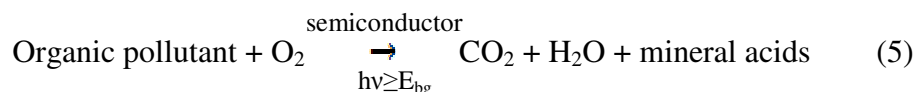
Illustration 2.5: Valence schematic Illustration of the common form of typical systems for the following semiconductor-sensitized reactions: (a) photoreduction of water by a sacrificial electron donor, such as ethylenediaminetetraacetic acid (EDTA), enhanced by the presence of a hydrogen catalyst, such as platinum, on the semiconductor's surface; (b) photo-oxidation of water by a sacrificial electron acceptor, such as persulphate, possibly enhanced by the presence of an oxygen catalyst, such as ruthenium dioxide, on the semiconductor's surface; (c) photodissociation of water, which appears to be unlikely unless carried out under forced conditions.

2.6.2 Semiconductor particles as photocatalysts for the removal of organic and inorganic pollutants

The first example in Table 2.3 is the oxidation of biomass with the concomitant reduction of water to hydrogen, i.e.



If experiments with this system had been carried out in aerated, rather than nitrogen-purged, solution, the reaction under study would have been one of the first, well-documented examples of the semiconductor-sensitized photomineralization of organic substrates by oxygen. The latter process may be summarized as follows:



The energetics and primary processes associated with the semiconductor-sensitized photomineralization of organic substrates by oxygen, i.e. reaction (5), are shown in Illustration 2.6.

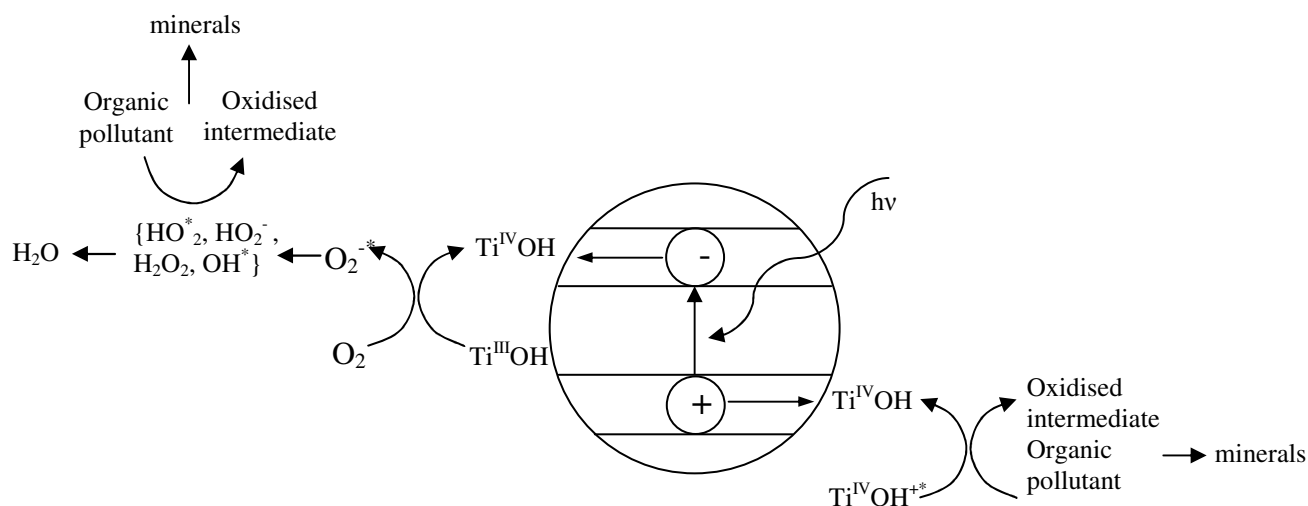
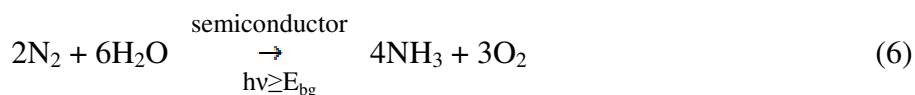


Illustration 2.6: Energetics and major general processes for the photo-oxidative mineralization of organic pollutants in aqueous solution by dissolved oxygen, sensitized by semiconductor particles. Many of the different chemical species which result from the reduction of oxygen, such as HO_2^* , HO_2^- , H_2O_2 and, possibly, OH^* radicals, play a major role in the oxidation of the organic substrate; it is already generally recognized that the trapped photogenerated hole species, $\text{Ti}^{\text{IV}}\text{OH}^{*+}$, is very important in the latter process.

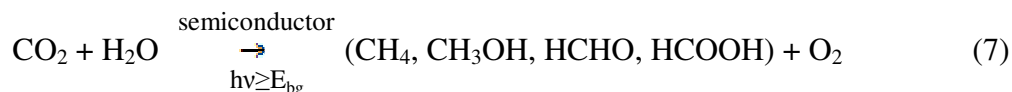
2.6.3 Semiconductor particles as sensitizers for the photoreduction of nitrogen and carbon dioxide

The photocatalytic synthesis of ammonia and oxygen from nitrogen and water, i.e.



was first claimed in 1977 by Schrauzer and Guth using water vapour and generating gaseous ammonia. Over the last 20 years, a plethora of semiconductor-sensitized photosystems for reaction (6), usually using liquid phase water and purporting to generate dissolved ammonia, have been described [21]. Various semiconductors have been used, including TiO_2 , SrTiO_3 , Fe_2O_3 , $\text{FeO}(\text{OH})$, WO_3 and CdS ; however, in all the systems studied, invariably the yields of ammonia have been very low, typically nanomoles, and around the limit of detection.

The photocatalytic reduction of carbon dioxide by semiconductor particles, under ambient conditions of temperature and pressure, to reduced carbon products, such as methanol, methane, formaldehyde and formic acid, in water, with the concomitant oxidation of water to oxygen, i.e.



has been less well studied compared with the reduction of nitrogen. However, the few reports of reaction (7) which do exist have the common features of very low yields and the real possibility of contamination.

2.6.4 Semiconductor particles as sensitizers for organic photosynthetic processes

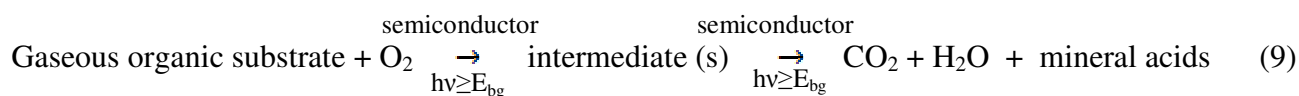
The use of semiconductors as sensitizers for various organic photosynthetic processes stems from the early work of Kraeutler and Bard on the use of platinized TiO_2 as a sensitizer for the conversion of acetic acid to methane and carbon dioxide: an alternative photoinduced Kolbe reaction. These workers were able to show subsequently that the conventional Kolbe reaction involving acetic acid could be photoinduced using a rutile TiO_2 photo anode.



It was quickly recognized that, if water was used as the solvent, reaction (5), the complete oxidative mineralization of the organic substrate, would usually predominate due to the generation of highly oxidizing hydroxyl radicals. Thus most work in the area of semiconductor-sensitized organic photosynthesis has been carried out either in an inert solvent, such as acetonitrile (MeCN), or in the neat organic substrate. The semiconductor-sensitized organic photosynthetic reactions which have been carried out to date can be fitted into the following broad categories: oxidations and oxidative cleavages, reductions, isomerizations and polymerizations.

2.6.5 Semiconductor particles and films as sensitizers for the destruction of gaseous and thin film organic pollutants

The use of semiconductors as sensitizers for organic photosynthetic reactions in the condensed phase has also been extended to work in the gas phase. For example, Djeghri and Teichner reported the details of the oxidation of 2-methylbutane by oxygen, sensitized by TiO_2 , in which the main initial products were carbon dioxide (15%), ethanol (16%), acetone (36%), butanone (12%) and 3-methylbutanone (10%). However, in this work, only 2% of the initial substrate was converted. Many more studies have investigated the initial selectivity of TiO_2 as a sensitizer for the photo-oxidation of gaseous organic substrates by oxygen. In most of the systems studied to date, although a relatively stable intermediate (or intermediates) is (are) often generated, eventually all the initial gaseous organic substrate is completely degraded to carbon dioxide, water and mineral acids, i.e.



2.6.6 Semiconductor particles as sensitizers for the photodestruction of cancer cells, bacteria and viruses

In photodynamic therapy (PDT), dye sensitizers, such as haematoporphyrin, are used, which ideally localize selectively in the cancerous tumor. Typically, the triplet state of the dye sensitizer can react directly with the biological material associated with the cancerous tumor, or transfer its electronic excitation energy to oxygen to form singlet oxygen, which can then react with and damage such biological material. A cancer cell will die if its membrane is damaged or the oxidation-reduction agents needed in the cell for the production of adenosine triphosphate (ATP), such as reduced glutathione, reduced nicotinamide adenine dinucleotide phosphate, coenzyme A (CoA) and flavine adenine dinucleotide, are depleted or exhausted. We have seen that semiconductors, such as TiO₂, can sensitize the photogeneration of OH^{*} and O₂^{*-} (or OOH^{*}) radicals, as well as hydrogen peroxide, and such species should be able to cause oxidative damage similar to that found in traditional PDT, leading to death of cancerous cells.

2.7 Conclusion

The field of heterogeneous photocatalysis is very diverse. Some of the earlier work on semiconductor photosystems has proved to be highly irreproducible; this has not helped the subject to develop as rapidly as it might have done and may have generated some degree of skepticism in the scientific community about subsequent developments in the field. However, as the research has moved away from systems a number of research themes have emerged which offer real potential for commercial development and merit much greater research. Of particular promise are the areas of:

- i) dye-sensitized nanocrystalline photoelectrochemical cells
- ii) semiconductor particles as photocatalysts for the removal of organic pollutants
- iii) semiconductor particles and films as sensitizers for the destruction of gaseous and thin film organic pollutants
- iv) semiconductor particles as sensitizers for the photodestruction of bacteria and viruses

The field of semiconductor photocatalysis is vibrant and involves many research groups throughout the world; it is one of the fields in photochemistry to be working in and, after a shaky start, appears to be going from strength to strength.

Chapter 3: Synthesis of Semiconducting Porous Metal Oxides (POX)

3.1 Introduction

To address the possibility of making new semiconductor photocatalysts that address limitations of previous works, two different types of porous metal oxides or POX, namely HTiNbO_5 and HNb_3O_8 were made from KTiNbO_5 and KNb_3O_8 respectively. The block diagram of overall synthesis process is given below and the stepwise synthesis process is discussed in this chapter.

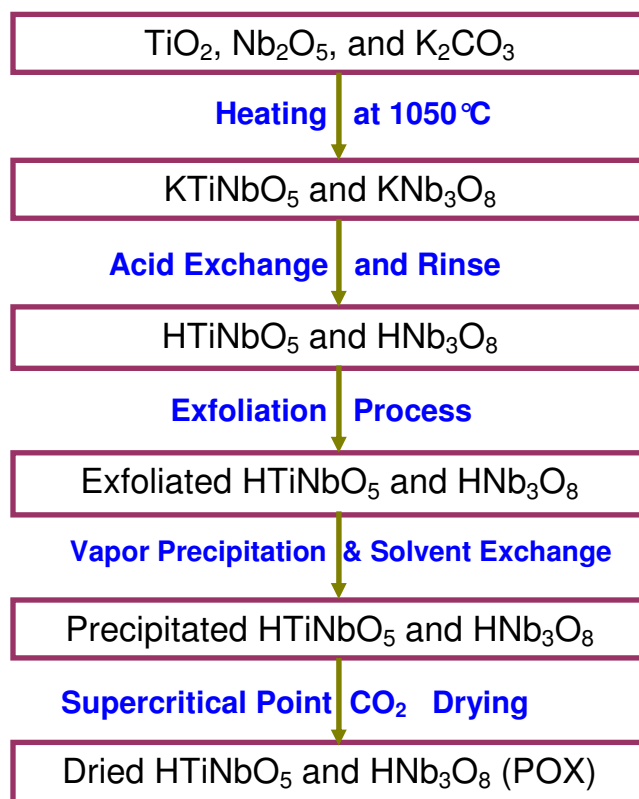


Illustration 3.1: Block diagram showing the synthesis process of porous metal oxides (POX)

3.2 Synthesis of KTiNbO_5 and KNb_3O_8

The synthesis of the semiconductors potassium titanium niobium pentoxide (KTiNbO_5) and potassium triniobium octoxide (KNb_3O_8) were prepared by a conventional solid state synthesis method^{25,35} at high temperature around 1050 °C. Reagent grade potassium carbonate, titanium dioxide and niobium (V) pentoxide were obtained from the GFS chemicals (Columbus, Ohio, USA) and used as

received, KTiNbO_5 and KNb_3O_8 were prepared by grinding stoichiometric amounts of K_2CO_3 , TiO_2 and Nb_2O_5 into a fine powder with a motor and pestle and mixed thoroughly. A 5% excess of K_2CO_3 was used to counteract loss of potassium as an oxide vapor during the heating cycle.

Table 3.1 Masses of K_2CO_3 , TiO_2 and Nb_2O_5 needed for preparation of KTiNbO_5

Reagent	Chemical formula	Mass needed in grams for KTiNbO_5
Potassium carbonate	K_2CO_3	7.0
Titanium dioxide	TiO_2	8.0
Niobium(V) oxide	Nb_2O_5	13.3

Table 3.2 Masses of K_2CO_3 , and Nb_2O_5 needed for preparation of KNb_3O_8

Reagent	Chemical formula	Mass needed in grams for KNb_3O_8
Potassium carbonate	K_2CO_3	3.5
Niobium(V) oxide	Nb_2O_5	20.0



Figure 3.1: High temperature furnace

3.2.1 Programming furnace for solid state reaction

The mixture was taken in an alumina crucible and then heated for 20 hours in a high temperature furnace (Lindburg/Blue M, BF51800 series, Asheville, NC, USA in Figure 3.1). The Illustration 3.2 shows two ramps and two dwells in the temperature program for the furnace. Segment 1 ramps slowly to 120 °C at a rate of 10 °C per minute, segment 2 dwells at 120 °C for about 30 minutes, segment 3 ramps to 1050 °C at a rate of 10 °C per minute, segment 4 dwells for 20 hours at 1050 °C and segment 5 is a fast return to a set point of 25 °C (close to ambient).

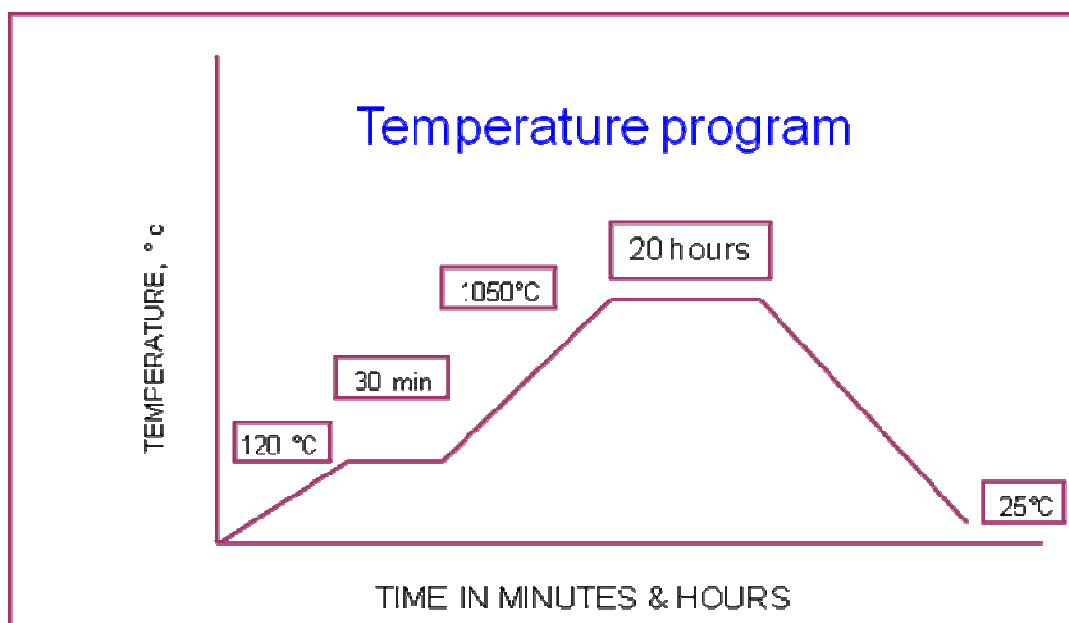
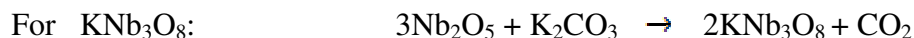
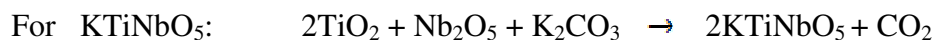


Illustration 3.2: Schematic of temperature program for heating ingredients in the furnace

The following are the reactions between materials during the synthesis of KTiNbO_5 and KNb_3O_8 in the furnace:



The results of these experiments were checked using powder X-ray diffraction analysis.

3.3 Acid exchange of KTiNbO_5 and KNb_3O_8

KTiNbO_5 and KNb_3O_8 have layered structures with exchangeable potassiums between layers of metal oxides. Conversion of these layered materials to the protonated lamellar compounds (HTiNbO_5 , HNb_3O_8) was accomplished by doing cation exchange reactions in strong acid solutions.

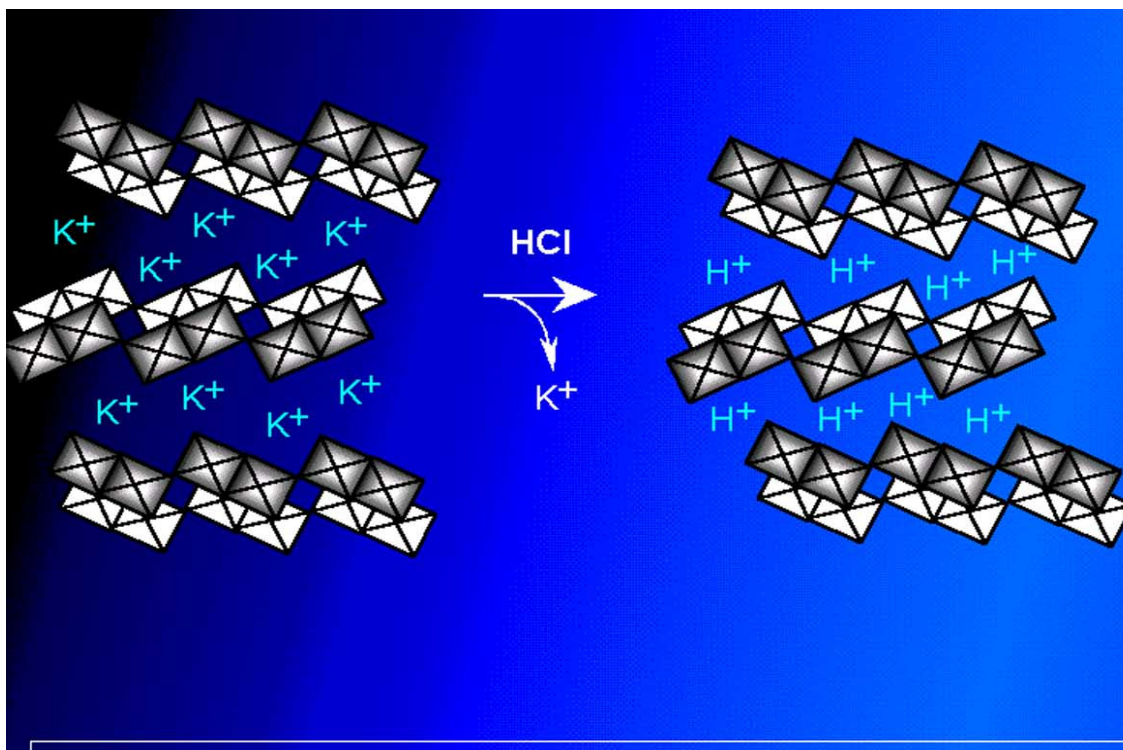


Illustration 3.3 KTiNbO_5 and KNb_3O_8 have layered structures with exchangeable cations

3.3.1 Procedure

Step 1: Five grams of KTiNbO_5 layered powder were placed in a 500 mL flask with 250 mL of DI water. About 100 mL of concentrated hydrochloric acid (12 M) was then added to the flask which was stirred for one day with no heat using a stirrer (Corning stirrer/hot plate, Acton, Massachusetts, USA).

Step 2: The slurries were centrifuged at 3000 rpm for 10 minutes by using Allegra X-12R Centrifuge (Beckman Coulter, Inc., Brea, California, USA) and the supernatant liquid was decanted. The solid acid exchanged material in the bottom of the centrifuge tube was recovered using DI water and the suspension was placed back in the flask.

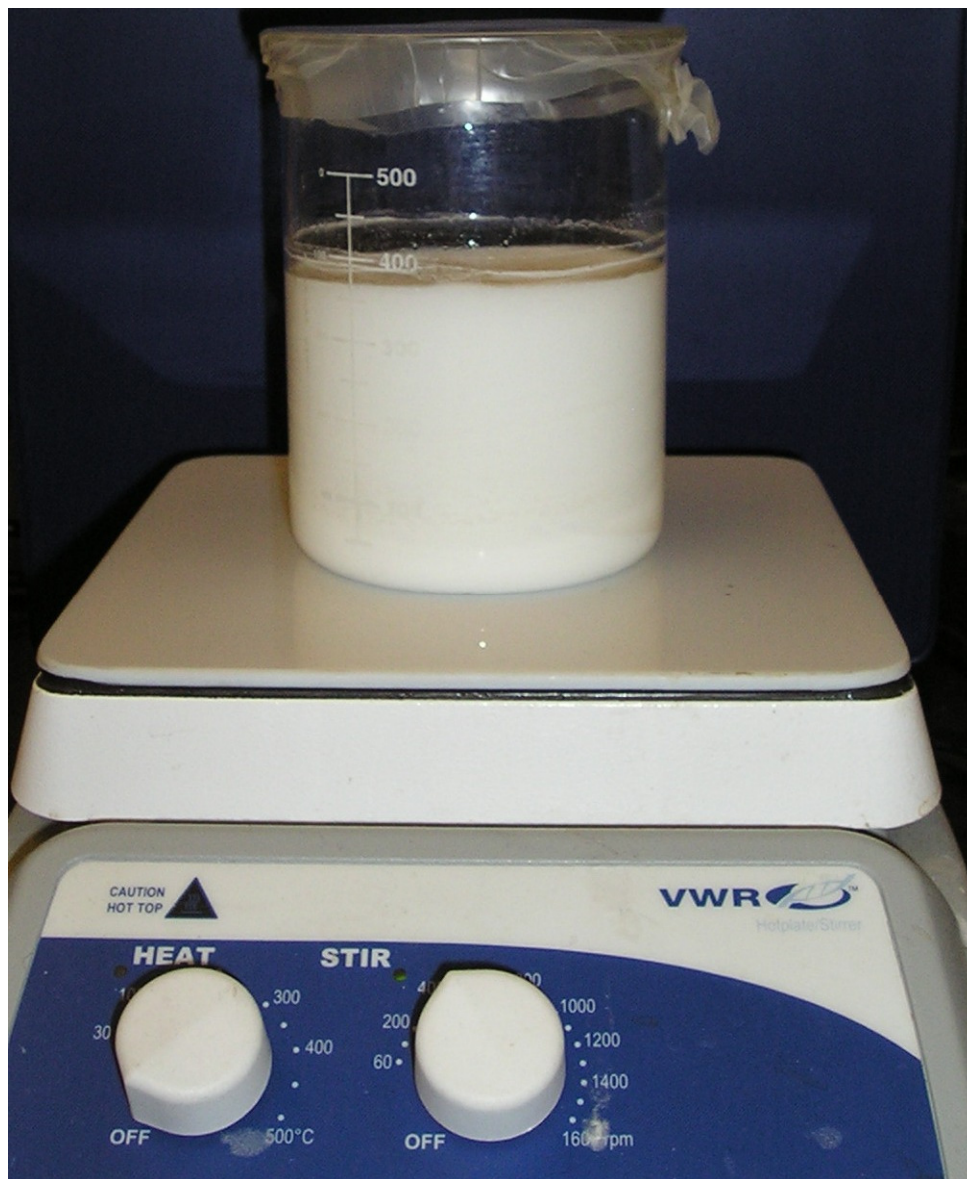


Figure 3.2: Stirring powders of KTiNbO_5 in acid solutions produces HTiNbO_5

Step 3: Steps one and two were repeated every 24 hours for three days for a total of four acid exchanges, to ensure a complete acid exchange. The suspension was again centrifuged and the solid sample was recovered with methanol, and the suspension was then transferred to a Petri dish and

allowed to dry at room temperature. The acid exchange reaction procedure for KNb_3O_8 to produce HNb_3O_8 was exactly same as the procedure for making HTiNbO_5 .

3.4 Preparation of single lamellar sheet colloids: Exfoliation

Chemical transformation of lamellar metal oxides into single sheet colloids or individual metal oxide sheets occurs when the suspension of HTiNbO_5 or HNb_3O_8 reacts with TBAOH (tetrabutyl aluminum hydroxide) by an acid base neutralization reaction.²⁷⁻³¹ This neutralization reaction forces bulky TBA^+ cations into the layers. These layered TBA^+ cations expand and hydrate the interlayer spaces, resulting in the exfoliation of individual metal oxide sheets. These exfoliated metal oxide sheets ($\text{TiNbO}_5^- / \text{Nb}_3\text{O}_8^-$) are negatively charged and have associated TBA^+ counter ions on their surfaces.

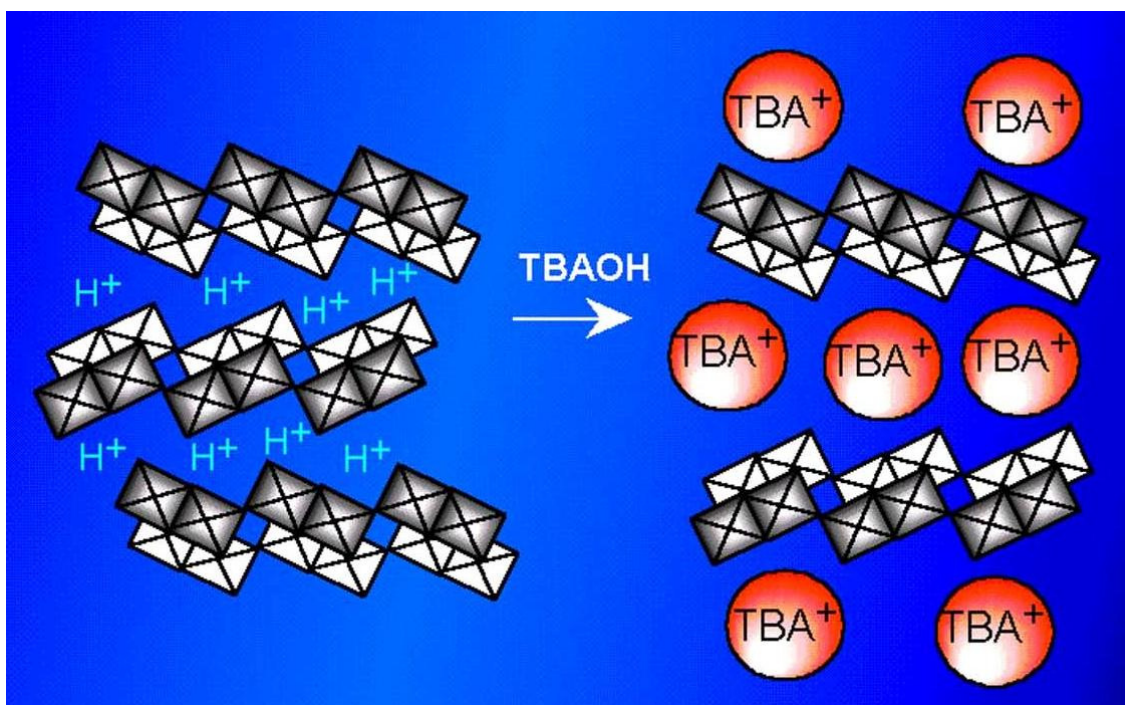


Illustration 3.4: Acid base neutralization reactions between HNb_3O_8 and TBAOH

TiNbO_5^- and Nb_3O_8^- lamellar colloids were obtained by adding 40 % tetra (n-buthylammonium) hydroxide (TBA^+OH^-) (Alfa Aesar, New Hampshire, USA) solution to 100 mL of distilled water

containing 2.0 g of HTiNbO_5 or HNb_3O_8 . TBAOH solution was added to the suspension and the pH was maintained around 9.5. The resulting colloidal sheet suspension was turbid and very stable. Settling of the layer particles occurred over a period of days, but the suspension was easily restored by shaking. These exfoliated sheets were regarded as two dimensional (2D) nano sheets.

Table 3.3: Amounts of acid exchanged material and TBAOH used

Reactant	Amount used	Amount of TBAOH added
HTiNbO_5	2.0 gram	2.4 mL
HNb_3O_8	2.0 gram	5.9 mL



Figure 3.3: Addition of TBAOH to HTiNbO_5 produces exfoliated individual sheets

3.5 Synthesis of Porous Metal Oxides

3.5.1 Vapor precipitation

Nano sheet colloids were precipitated with acid to form ultra-porous, stable, transition metal oxides. Small cations, such as H^+ (charge density much higher than that of TBA^+) were introduced into colloidal sheet suspensions. The small cations, driven by electrostatic forces, displace the large TBA cations from the surface of the sheets. At higher concentrations, these small cations destroy the mechanism that stabilizes the colloid and causes particle flocculation.

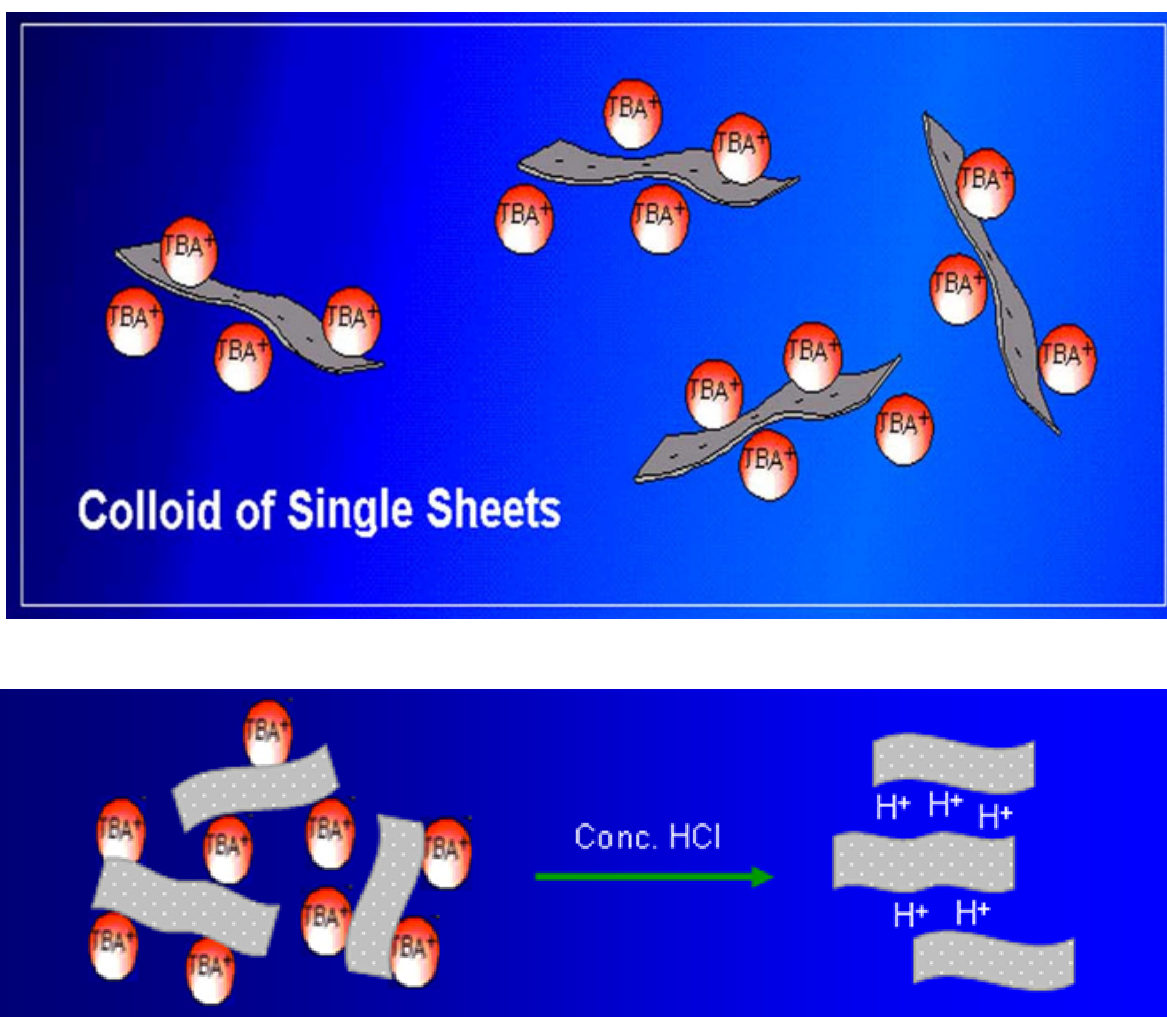


Illustration 3.5: (a) shows exfoliated colloidal single sheets and (b) shows exposure to acid vapor makes sheets precipitate.

Nanosheets of the titaniumniobate and triniobate were precipitated into porous aggregates by the HCl vapor precipitation method. First 4 mL of colloids were mixed with 20 mL of alcohol (Reagent, GFS Chemicals) in a 30 mL borosilicate glass vial. The vial was then placed in a 500 mL beaker that contained 2 mL of concentrated hydrochloric acid. The beaker was covered by parafilm, so that vapors from hydrochloric acid diffused into the solution in the vial. The sample was allowed to sit in acid vapors for two days.



Figure 3.4: Vapor precipitation of metal oxide sheets.

3.5.2 Solvent replacement

After precipitating the colloidal nanosheets into porous aggregates, the vial was placed in a 500 mL beaker filled with enough acetone to cover the vial, and the acetone outside the vial was stirred for four days. The beaker was covered with parafilm. Each day the solvent was replaced with fresh acetone. In this way the solvent exchange was done for a total of four days. On the fifth day the sample vial was

placed in a different 500 mL beaker containing silica beads soaked in acetone. The beaker was covered with aluminum foil and placed on a hot plate (Corning stirrer/hot plate, Acton, Massachusetts, USA) for two days at a temperature of 40 °C.



(a)



(b)

Figure 3.5: Solvent exchange- (a) use of acetone and stirrer and (b) use of acetone, silica beads with a moderate heat.

3.5.3 Solvent replacement

Supercritical carbon dioxide refers to carbon dioxide that is in a fluid state while also being at or above both its critical temperature and pressure, yielding rather uncommon properties. Carbon dioxide usually behaves as a gas in air at STP (Standard Temperature and Pressure) or as a solid called dry ice when frozen. If the temperature and pressure are both increased from STP to be at or above the critical point for carbon dioxide, it can adopt properties midway between a gas and a liquid. More specifically, it behaves as a supercritical fluid above its critical temperature (31.1 °C) and critical pressure

(72.9 atm/7.39 MPa), expanding to fill its container like a gas but with a density like that of a liquid. Supercritical CO₂ is becoming an important commercial and industrial solvent due to its role in chemical extraction in addition to its low toxicity and environmental impact. The supercritical point CO₂ drying process allows samples to be dried without any surface tension, thus reducing the likelihood of capillary force or solvent surface tension. The relatively low temperature of the process and the stability of CO₂ also allows most compounds to be extracted with little damage or denaturing.

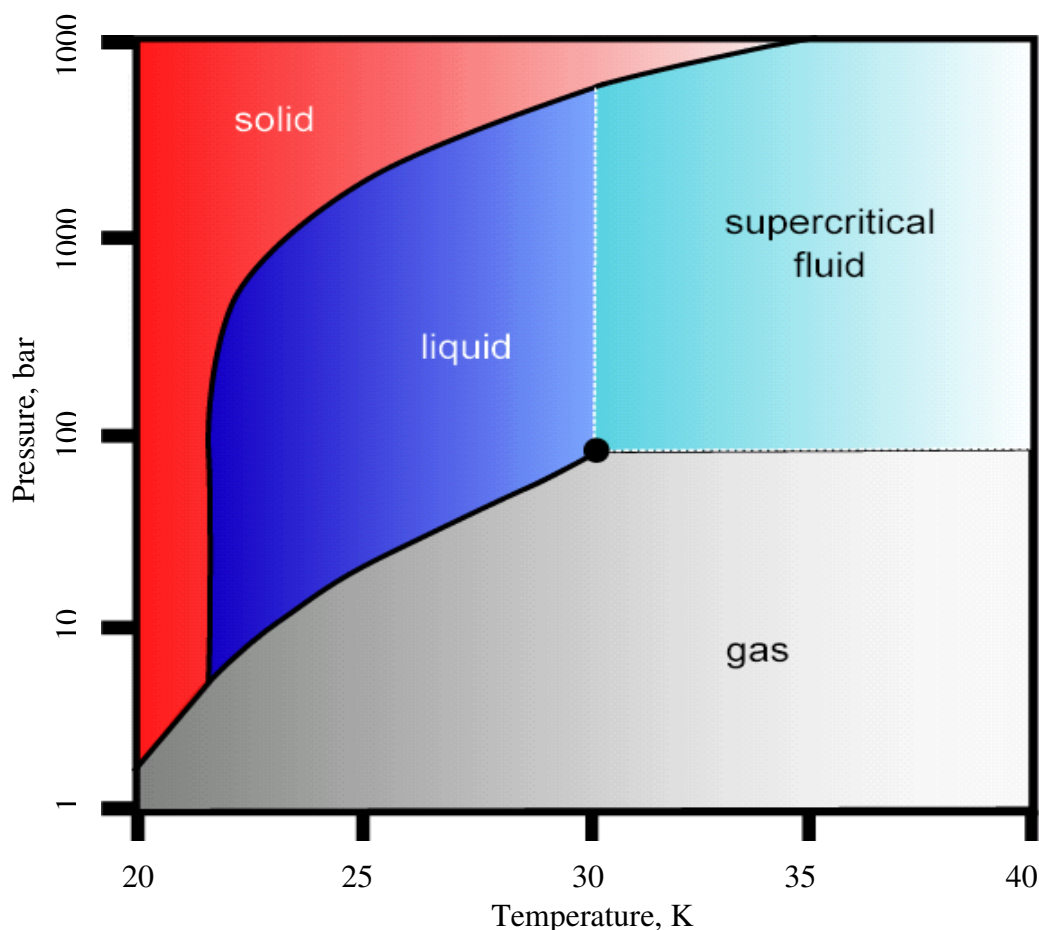


Illustration 3.6: Phase diagram of carbon dioxide

3.5.4 Drying procedure

Supercritical CO₂ drying process was done using a drying system made by Quorum Technologies, East Sussex, U.K. Stepwise drying process is described below.



Figure 3.6: Supercritical point CO₂ chamber

The drying chamber was cleaned and cooled to 15-19 °C by circulating cold water and then filled half with dry acetone. The sample vial was placed in the chamber while the vial was encased with copper screen to allow the passage of solvent and then the chamber door was closed. The chamber inlet valve was opened enough to begin letting in liquid CO₂, taking care that the rate of influx did not disturb the sample particles. While the CO₂ inlet was open, the acetone in the chamber was flushed by releasing acetone rich solvent out from bottom outlet. After a short while, there was an acetone/CO₂ phase line, which moved down as pure CO₂ come in. The chamber was filled and emptied for three times with occasional agitation (to promote the mixing). Finally the chamber was filled to $\frac{3}{4}$, all chamber valves were gently closed and the cold pump was turned off. The chamber temperature was raised to 30 °C by a circulating hot water. It was noticed that the fluid expanded slightly inside the chamber. At this point the

hot water circulation was stopped and the chamber was kept at 30 °C for 20 minutes. The chamber was cooled again to 15-19 °C by circulating cold water and the CO₂ inlet valve was opened to let in fresh CO₂ and lower outlet valve was opened to flush the chamber. This flushing was carried on for 10 mins and finally the chamber was filled to 2/3 and closed inlet and outlet valves. The chamber was heated again by circulating hot water until it reached 40 °C. During this heating step at around 34-35 °C, the CO₂ reached supercritical phase. Once the chamber reached 40 °C, the chamber was kept at that condition for 15 minutes without heating it anymore. Then the top venting valve was opened and the gas was slowly released at about 20 PSI/min. The chamber was opened when pressure reached atmospheric.



Figure 3.7: Dried Porous Metal Oxides (POX) are very light-weight low density materials

3.6 Topotactic dehydration

Dried POX materials have ionic connection between the layers and protons (H⁺) act as a bridge between them. It is believed that electronic conduction will be better if the layers have some sort of covalent association. When the POX materials were heated at 450 °C for 2 hours in furnace, produced topotactic dehydrated POX by vaporizing H₂O (Illustration 3.7).



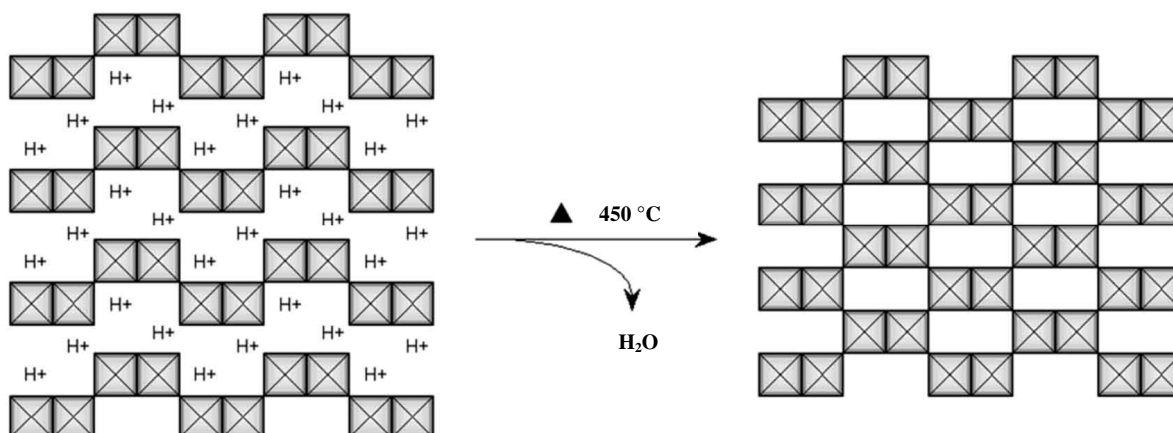


Illustration 3.7: Heating POX materials (a) at 450 °C produces topotactic dehydrated materials (b).

3.7 Conclusion

The layered materials KTiNbO_5 and KNb_3O_8 were used to prepare dried porous aggregates. KTiNbO_5 and KNb_3O_8 were prepared by a conventional solid state reaction method. These transition layered materials have layered structure with exchangeable cations. Conversion of KTiNbO_5 and KNb_3O_8 to the protonated compounds HTiNbO_5 and HNb_3O_8 was accomplished by doing cation exchange reactions in strong acid solutions. Chemical transformation of lamellar metal oxides into single sheet colloids or nanosheets occurred when the suspension of HTiNbO_5 or HNb_3O_8 reacted with TBAOH in an acid base neutralization reaction. This neutralization reaction forced bulky TBA^+ cations into the layers. These layered TBA^+ cations expand and hydrate the interlayer spaces, resulting in the exfoliation of individual metal oxide sheets. Two dimensional nano sheets were precipitated in acidic conditions to form ultra-porous, stable, transition metal oxide material. Supercritical point CO_2 drying was used to get the dried porous aggregates, super critical point CO_2 drying process allowed the samples to be dried without any surface tension, thus reducing the likelihood of collapsing the porous structure.

Chapter 4: Characterization of POX

4.1 Introduction

Synthesized porous metal oxide (POX) materials were characterized by different techniques available in the university. The BET and Langmuir surface areas, pore volumes, pore sizes, and pore size distribution of the POX aggregates were measured by using the Accelerated Surface Area and Porosity system (ASAP 2020) by Micromeritics Instrument Corporation (Georgia, USA) which uses N_2 adsorption. Structural characterizations were carried out by powder x-ray diffraction studies (XRD) using a XRD system (D8 Discover, Bruker Axs Inc., WI, USA). Diffraction data was collected for the starting materials ($KTiNbO_5$ and KNb_3O_8), acid exchanged materials ($HTiNbO_5$ and HNb_3O_8), POX ($HTiNbO_5$ and HNb_3O_8) and topotactic dehydrated POX ($Ti_2Nb_2O_9$ and Nb_6O_{15}). The surface morphologies of POX materials were studied by scanning electron microscopy (S-4800, Hitachi, Japan) and transmission electron microscopy (H-9500, Hitachi, Japan). The band gap of the porous aggregates was measured by a reflectance UV-Vis scanning spectrophotometry (Shimadzu Kyoto, Japan). The absorbance was measured over the wavelength range of 200 nm to 600 nm, and the onset of absorbance was determined by extrapolating the steep part of the rising absorption curve down to the wavelength X-axis. Elemental analysis (C, H, and N) was done by Quantitative Technologies, Inc (Washington D.C., USA) and Inductively Coupled Plasma-Optical Emission Spectroscopy (Optima 4300 DV, Perkin Elmer, Norwalk, CT, USA).

4.2 BET surface area analysis

The ASAP 2020 analyzer is equipped with two independent vacuum systems, one for sample preparation and one for sample analysis. Having two separate systems, as well as separate preparation ports, allows sample preparation and sample analysis to occur concurrently without interruption. Compressed gases are required for analyses (nitrogen and helium) of the samples in the ASAP 2020 porosity system.

4.2.1 Analysis technique

The basics of the analytical technique used in these porosity systems were simple. A sample contained in an evacuated sample tube was cooled to cryogenic temperature, and then was exposed to the analysis gas at a series of precisely controlled pressures. With each incremental pressure increase, the number of gas molecules adsorbed on the surface increased.

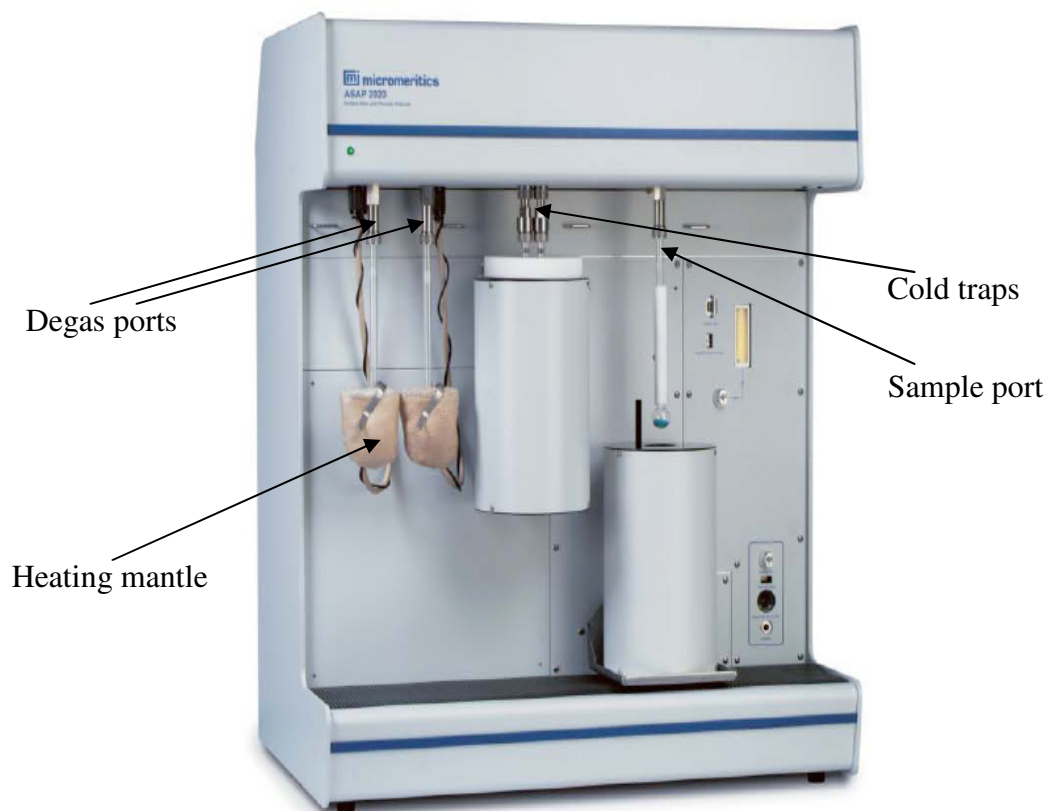


Figure 4.1: Front view of ASAP2020 porosity system

As adsorption proceeded, the thickness of the adsorbed film increased. Any micropores in the surface were quickly filled, then the free surface became completely covered, and finally larger pores were filled. Then desorption process began, in which pressure was systematically reduced resulting in liberation of the adsorbed molecules. As with the adsorption process, the changing amount of gas on the solid surface was quantified.

4.2.2 Sample preparation

Long stem sample tubes were used to analyze dried porous samples. Sample tubes were plugged into a degassing port and a heating mantle was attached to it. The parameters for degassing, adsorption, analysis and final report were chosen, and the analysis was started.

4.2.3 Degassing condition

0.06 gm of porous materials samples were analyzed. Pretreatment of the POX was done to each sample in a degassing process. The typical parameters we choosen for all samples are as follows. The temperature ramp rate was 10 °C/min; the target temperature was 90 °C; evacuation rate was 5mm Hg/s; the unrestricted evacuation began at from 5mmHg/s; vacuum set point was 10µmHg and the evacuation time was 30 min. For the heating phase, the ramp rate was 10 °C/min, the holding temp was 150 °C for two hours. The relative pressure (P/Po) range was 0.03 to 0.5, and nitrogen gas was used as a backfill gas. Figure 4.2 shows the parameters for degassing. It takes usually three hours to complete the degassing process.

ASAP 2020 V1.04

File Unit 1 Reports Options Windows Help

C:\2020\PARAMS\SI-AL.DEG

Degas Conditions

Description: HTiNb05 - Non Topo - Masud Replace...

Evacuation Phase

Temperature ramp rate: 10.0 °C/min

Target temperature: 90 °C

Evacuation rate: 5.0 mmHg/s

Unrestricted evac. from: 5.0 mmHg

Vacuum setpoint: 10 µmHg

Evacuation time: 30 min

Heating Phase

Ramp rate: 10.0 °C/min

Hold temp: 150 °C

Hold time: 180 min

Evacuation and Heating Phases

Hold pressure: 100 mmHg

☒ Backfill sample tube

Save Close

Figure 4.2 Parameters for degassing the porous metal oxides in ASAP porosity system.

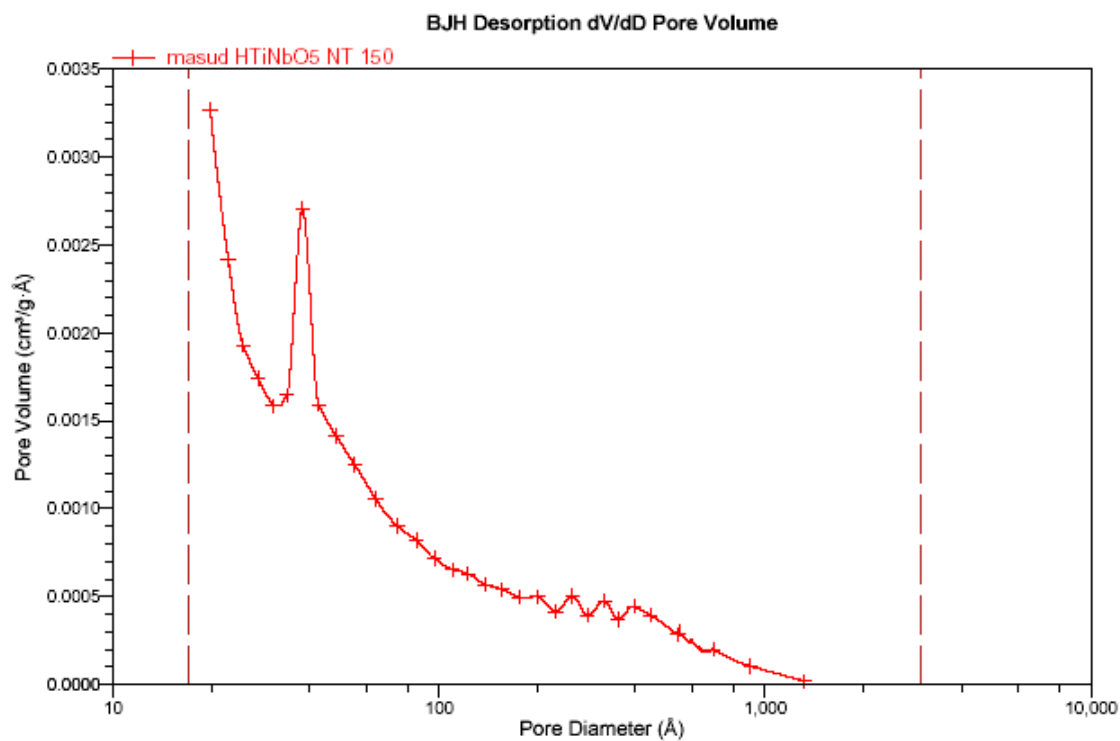


Figure 4.3: BJH desorption dV/dD pore volume graph of POX – HTiNbO₅.

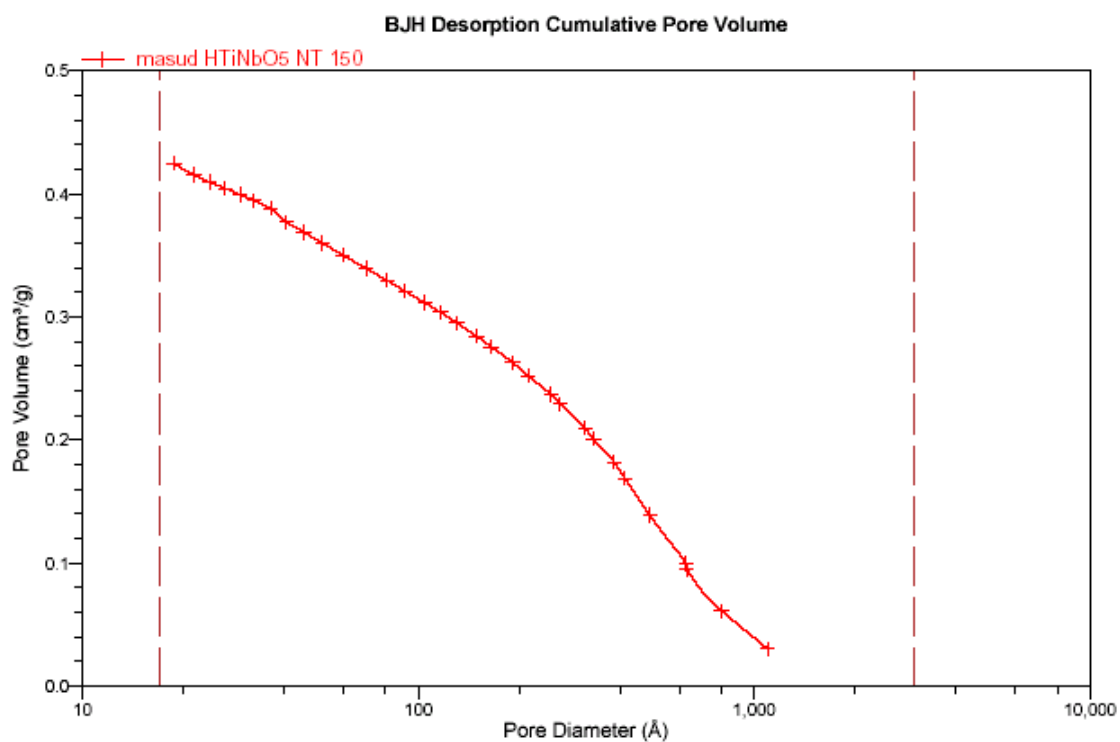


Figure 4.4: BJH desorption cumulative pore volume of POX – HTiNbO₅.

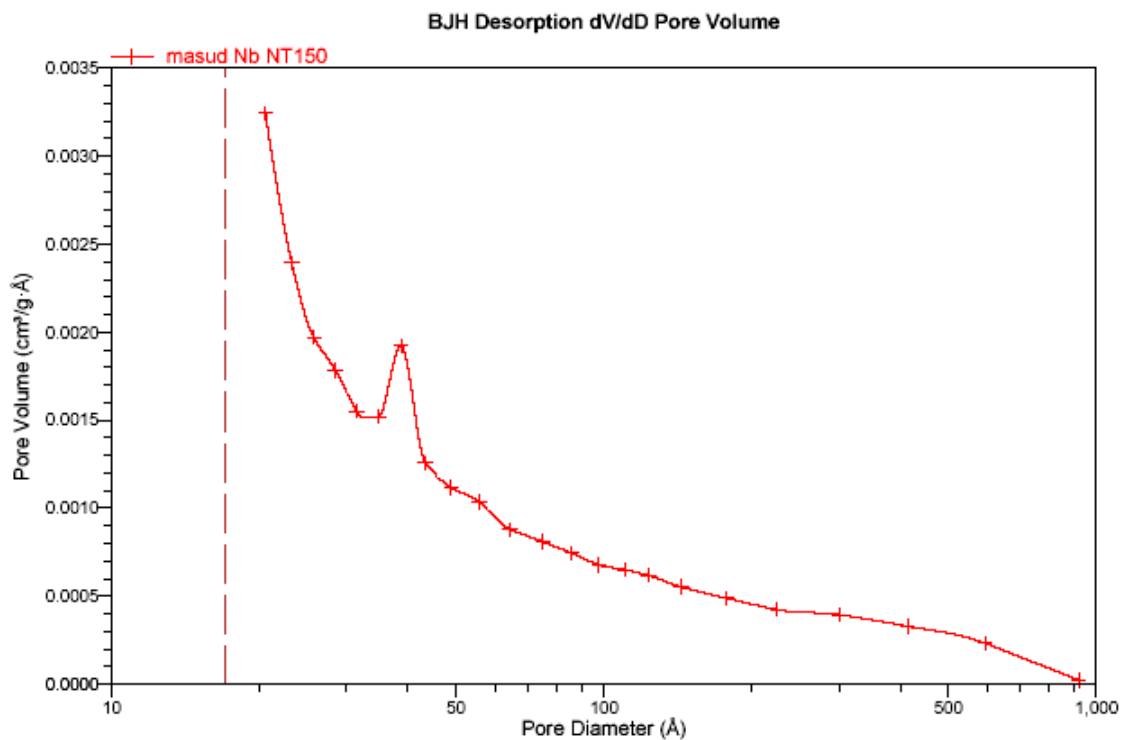


Figure 4.5: BJH desorption dV/dD pore volume graph of POX – HNb₃O₈.

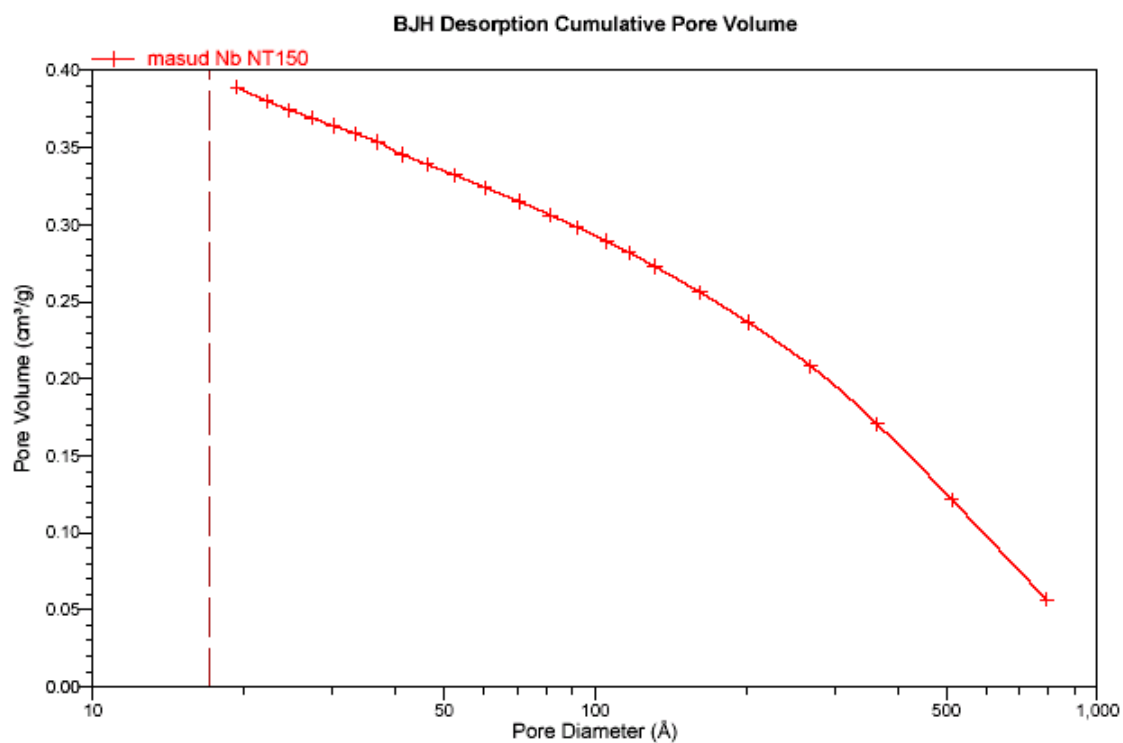


Figure 4.6: BJH desorption cumulative pore volume graph of HNb₃O₈.

4.2.4 Sample analysis

Degassed sample was placed in sample port and the corresponding sample file was selected to start the analysis (Figure 4.7). It takes usually ten hours to complete the measurements. Figure 4.3 and 4.4 show the pore volume measurements corresponding to the pores of POX-HTiNbO₅ and Figure 4.5 and 4.6 show the pore volume measurements corresponding to the pores of POX-HNb₃O₈. A random pore size distribution was observed in both POX materials, with a large fraction of the pore volume coming from very large pores. A common peak was found at about 40 Å which was most likely to be from the hollows along the folds of the sheets. The POX-HTiNbO₅ material gave a BET surface area of 140 m²/g with an average pore diameter of 114 Å and the POX-HNb₃O₈ material gave BET surface area of 155 m²/g with an average pore diameter of 115 Å (Table 4.1).

ASAP 2020 V1.04

File Unit 1 Reports Options Windows Help

Analysis (Unit 1 - S/N: 357)

View: Operation Browse

Sample: Nb NT 150

Mass: 0.0517 g

Analysis Conditions: Run Conditions

Adsorptive Properties: Nitrogen @ 77.35 K

Report Options: Report Options

Po: 760.000 mmHg

Bath temperature: 77.300 K

Warm free space: 16.0000 cm³

Cold free space: 45.0000 cm³

Report After Analysis...

<< Prev Start Cancel Close

Preliminary		Analysis				Termination	
Sample	Stage	Last Point	P (mmHg)	P/Po	Q (cm ³ /g STP)	Po (mmHg)	Run Time
NBNT9158	Idle						
Details:							

Figure 4.7: Sample analysis in ASAP porosity system.

Table 4.1: BET surface area measurements of POX materials

Sample	Single point surface area, m ² /g	BET surface area, m ² /g	Langmuir surface area, m ² /g	BJH desorption pore volume, cm ³ /g	BJH desorption average pore diameter, Å
POX-HTiNbO ₅	131.91	139.97	228.23	0.42	113.99
POX-HNb ₃ O ₈	106.10	109.64	272.42	0.32	138.78

4.3 X-ray diffraction analysis

Degree of crystallinity of POX materials were measured with X-ray diffractometer (Cu-K α radiation) in the department of Metallurgical and Materials Engineering at UTEP. Parent materials (KTiNbO₅ and KNb₃O₈), unexfoliated (acid exchanged) materials (HTiNbO₅ and HNb₃O₈) and topotactic dehydrated materials (Ti₂Nb₂O₈ and Nb₆O₁₅) were compared with POX materials.

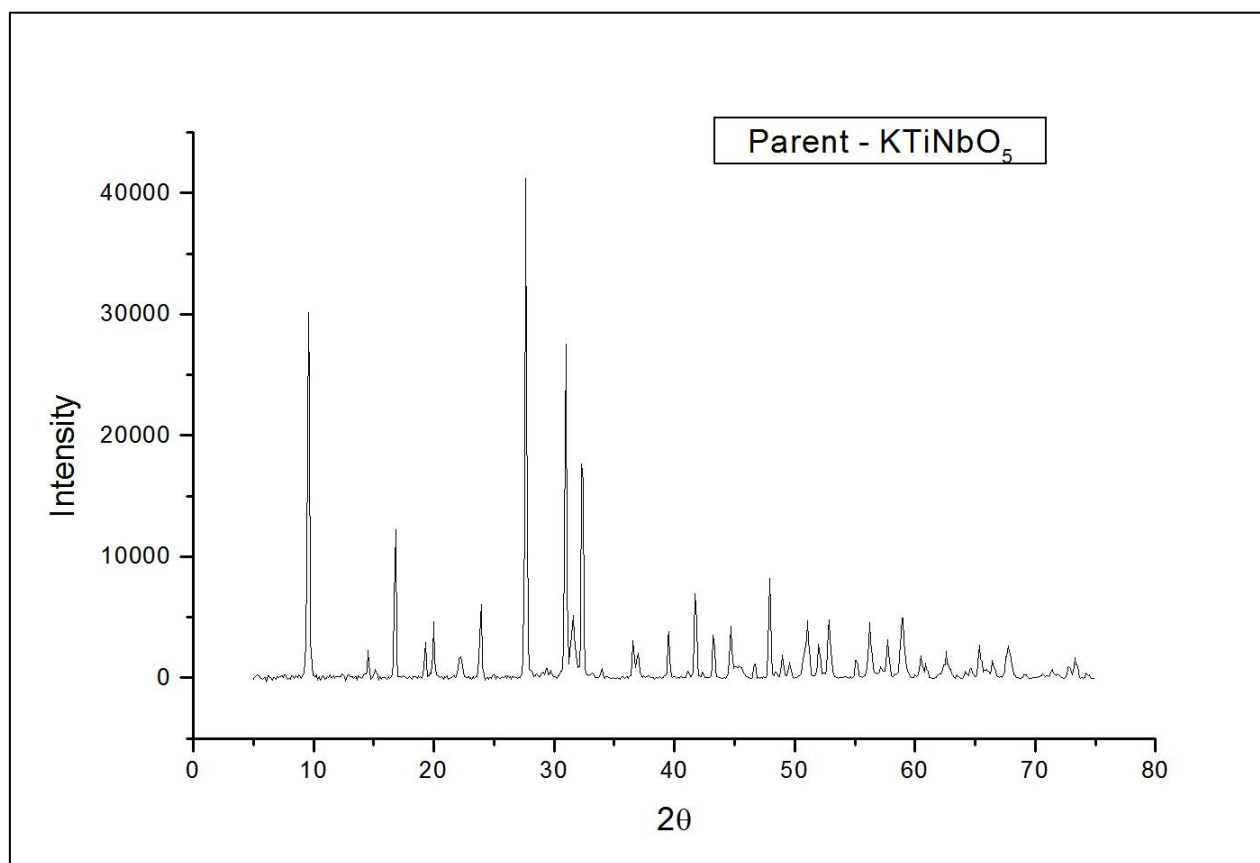


Figure 4.8: X-ray diffraction of parent material – KTiNbO₅

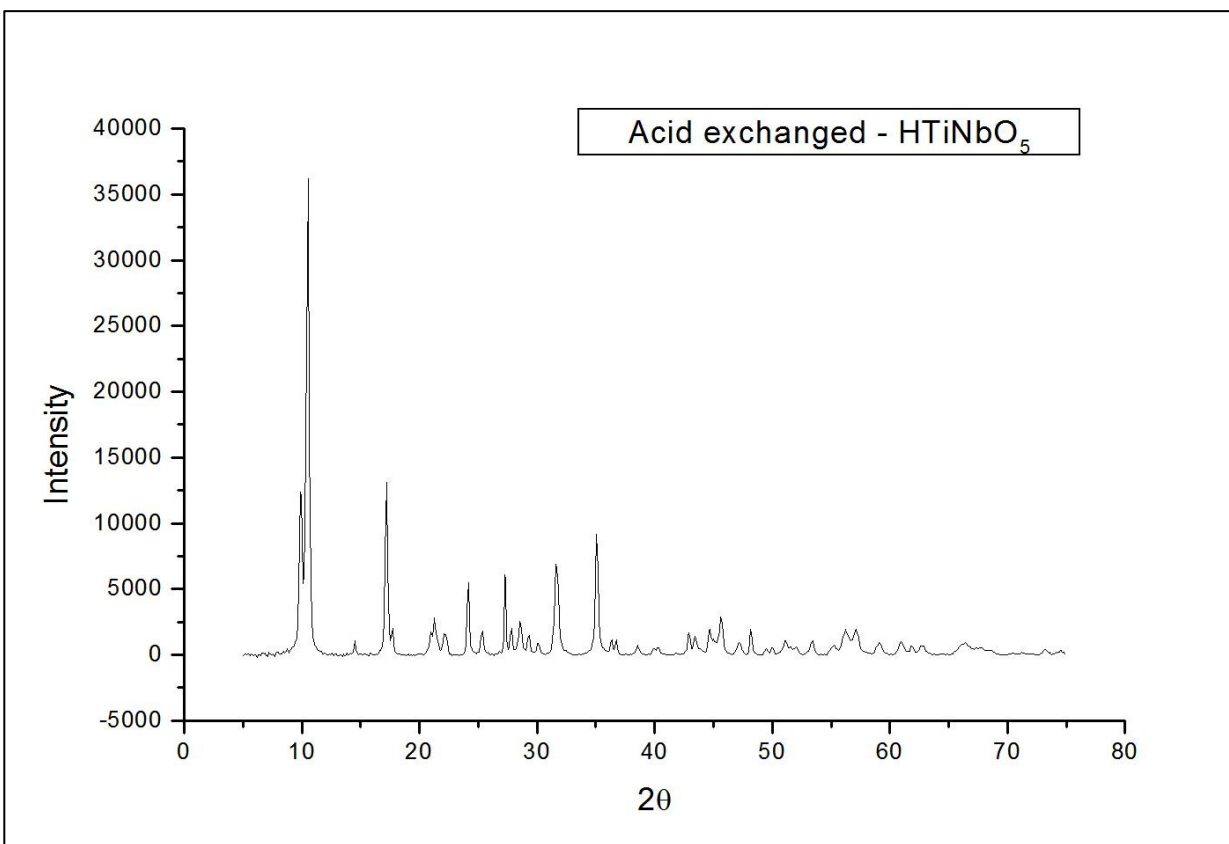


Figure 4.9: X-ray diffraction of unexfoliated material – HTiNbO_5

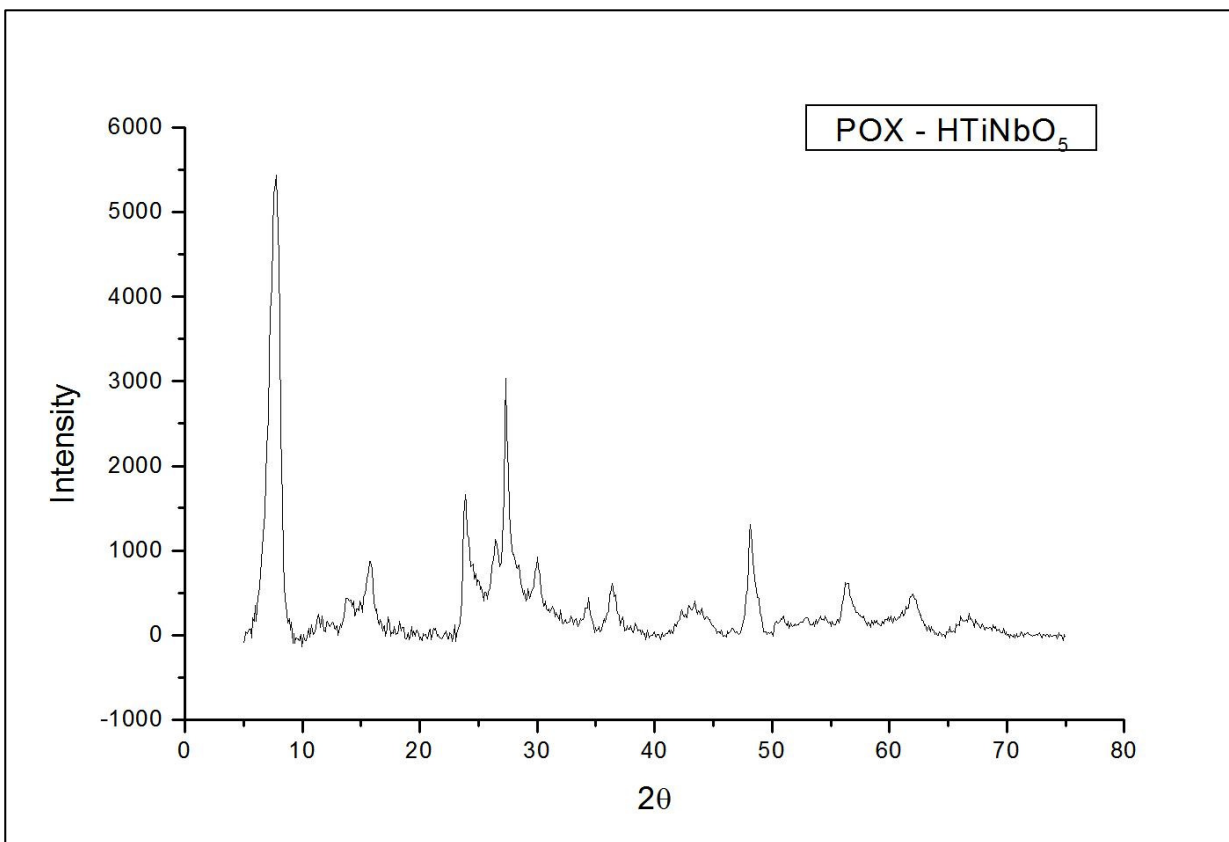


Figure 4.10: X-ray diffraction of $\text{POX} - \text{HTiNbO}_5$

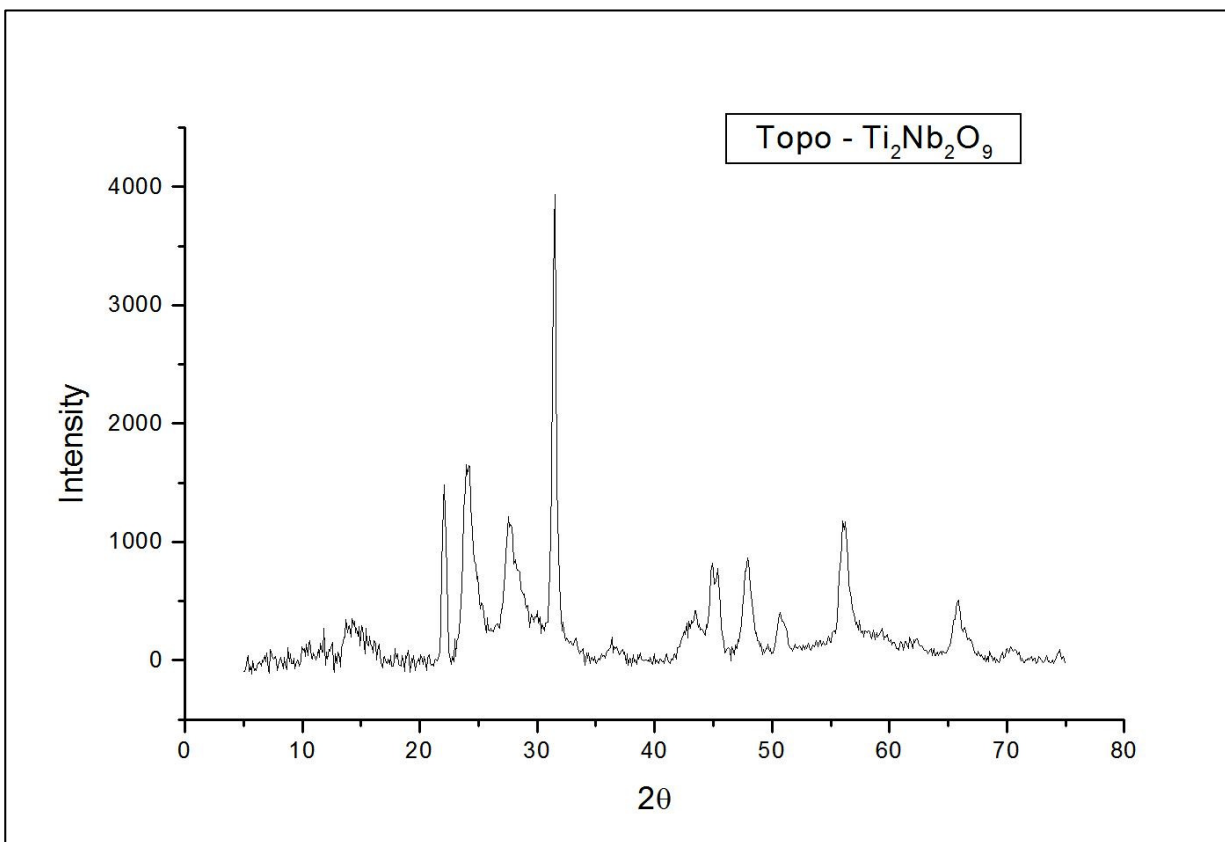


Figure 4.11: X-ray diffraction of topotactic dehydrated materials – $\text{Ti}_2\text{Nb}_2\text{O}_9$

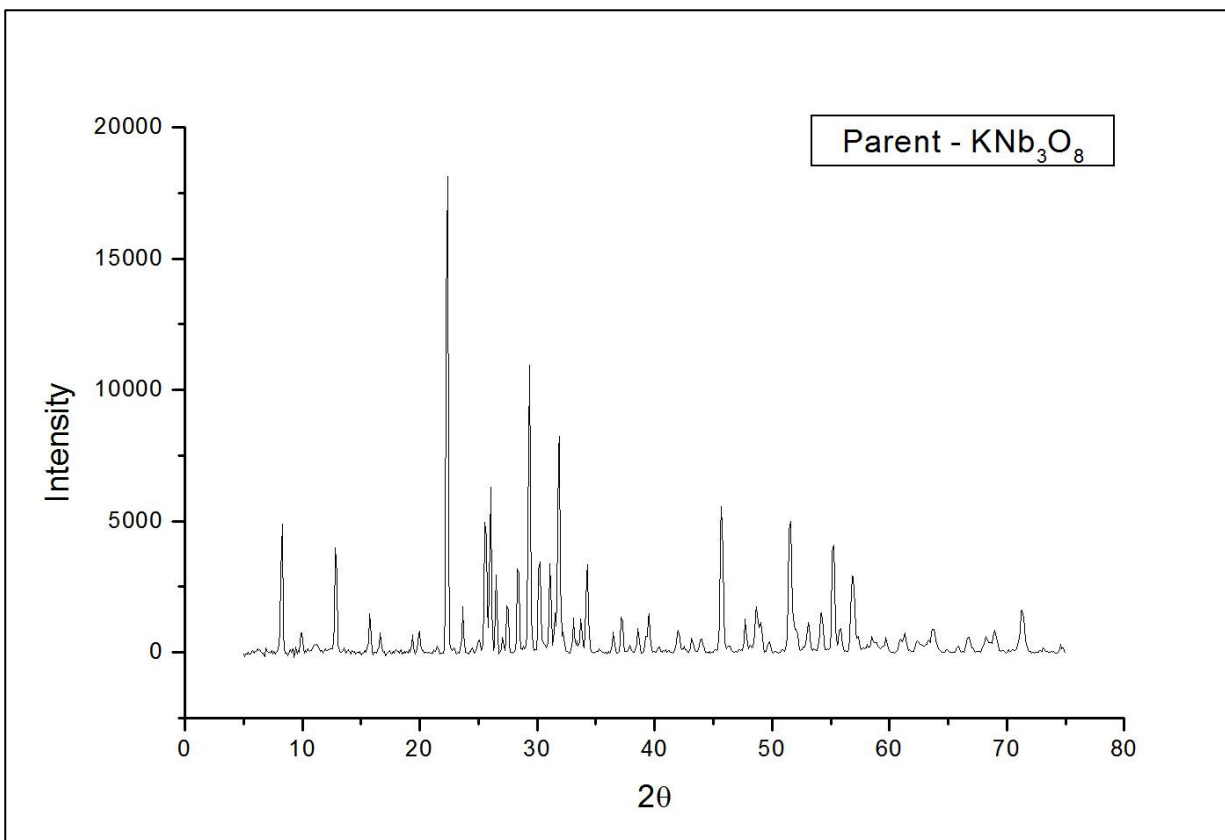


Figure 4.12: X-ray diffraction of parent material – KNb_3O_8

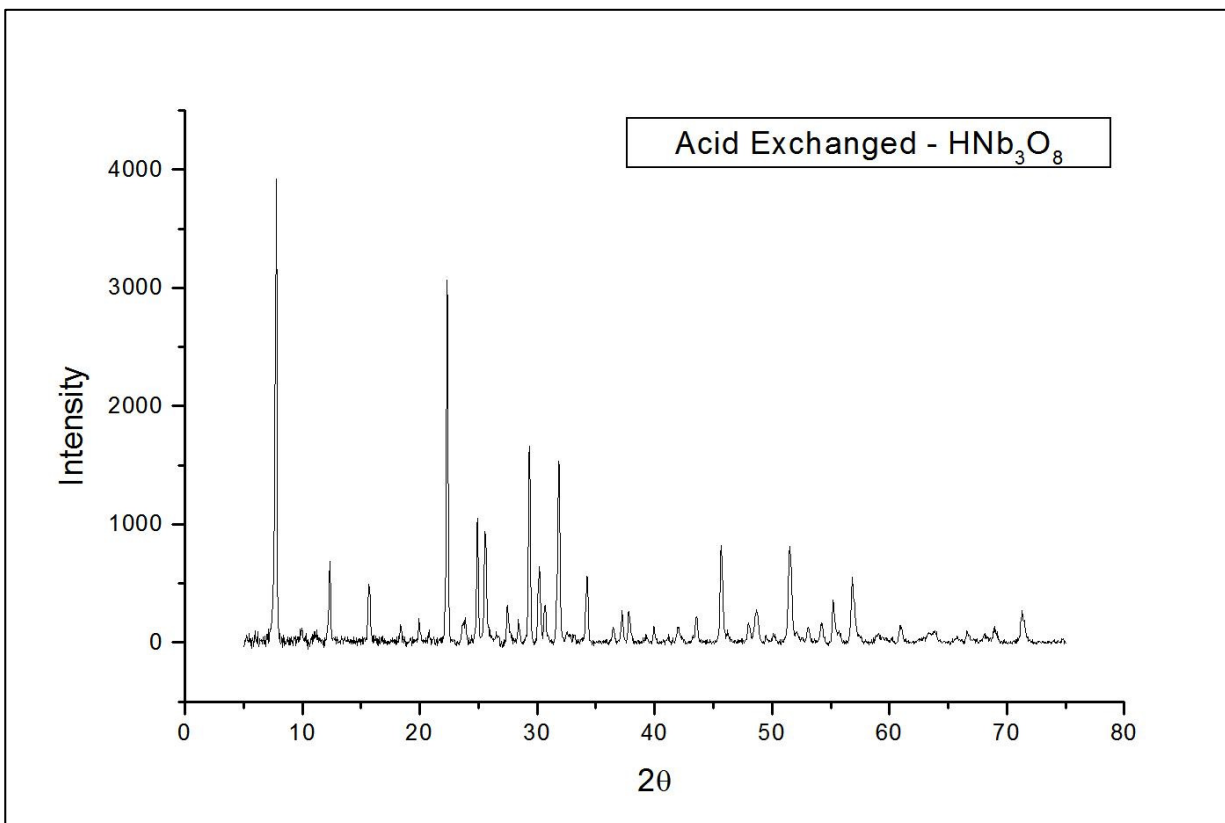


Figure 4.13: X-ray diffraction pattern of unexfoliated material – HNb_3O_8

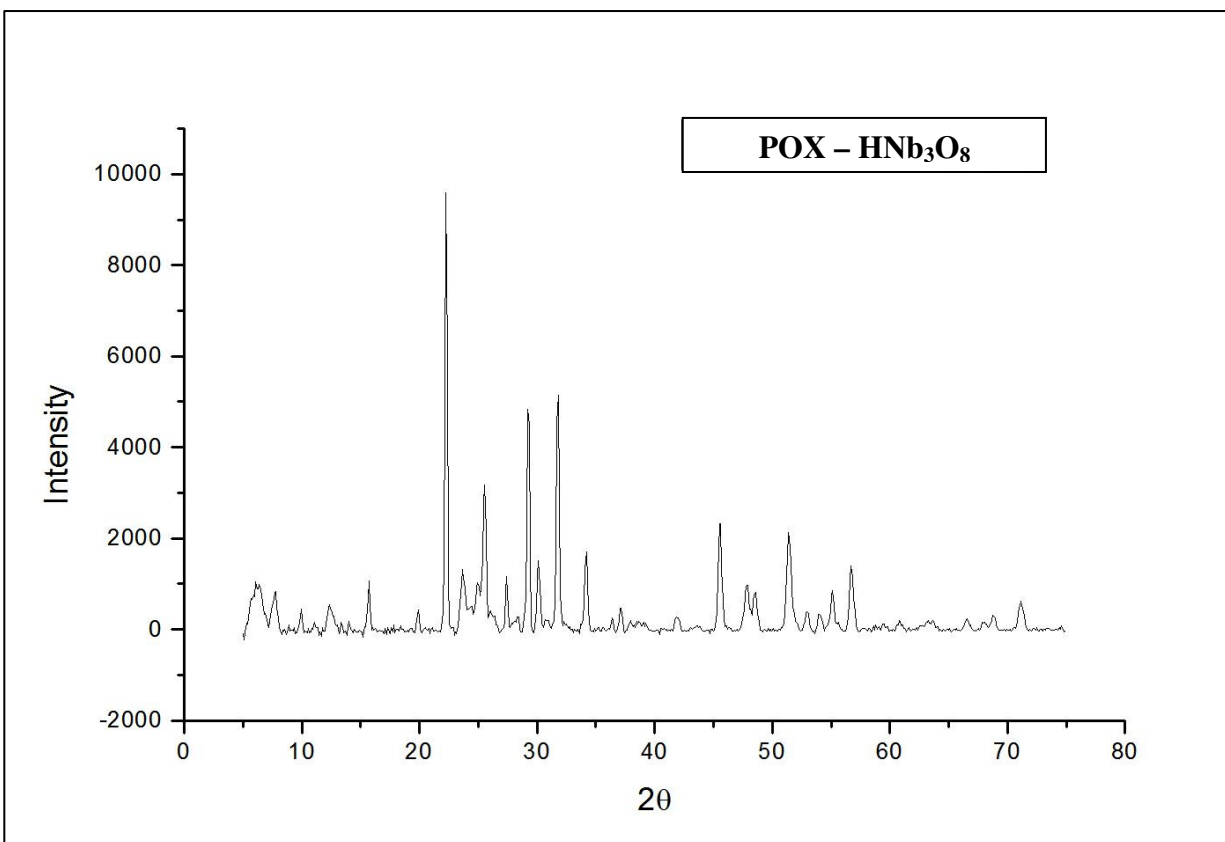


Figure 4.14: X-ray diffraction pattern of POX – HNb_3O_8

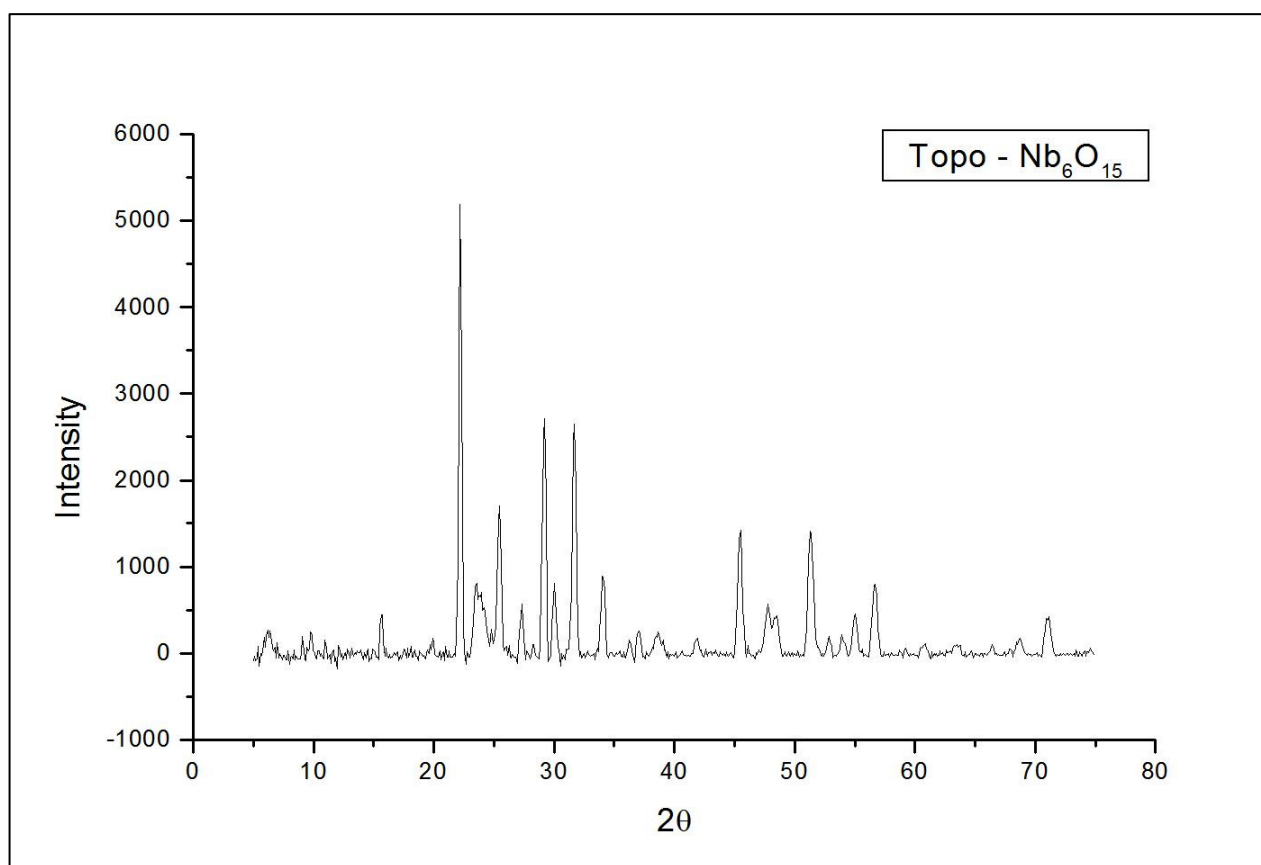


Figure 4.15: X-ray diffraction pattern of topotactic dehydrated materials – Nb_6O_{15}

X-ray diffraction patterns showed that the crystallinity of the precursor materials was preserved in the synthesized parent, acid exchanged, POX and topotactic dehydrated materials. The peaks at about 9° , 17° and 23° 2θ in Figure 4.8 correspond to the layer spacing. In the acid exchange reaction where K^+ ions were replaced with H^+ ions, the distances between the layers were shorter, due to the size difference of the cations. Consequently the layer-line reflections in the XRD pattern move to the right in the acid exchanged materials. Figure 4.9 shows the layer peaks at 10° , 17° and 24° 2θ . In the POX materials, restacking layer peaks are also visible (Figure 4.10) however the intensity of the peaks are much lower compared to those in the parent and acid exchanged materials. This is due to the fact that POX materials have high degrees of randomness of metal oxide sheets, which means no registry of the in-plane atoms with the other sheets. The layer spacing was eliminated during the topotactic dehydration process. So the

topotactic dehydrated materials do not show any prominent peak at low 2θ (Figure 4.11 and 4.15). Layer restacking peaks are visible in KNb_3O_8 and HNb_3O_8 (Figure 4.12 and 4.13).

4.4 UV-visible reflectance spectrometry

Absorption bands of both HTiNbO_5 and HNb_3O_8 based materials were checked at different stages (acid exchanged, POX, topotactic and wet POX) of their synthesis process by using a reflectance UV-Vis scanning spectrophotometer (Shimadzu Kyoto, Japan) in Dr. Dirk's lab in the Department of Chemistry at UTEP. Wet POX materials are the precipitated exfoliated colloids.

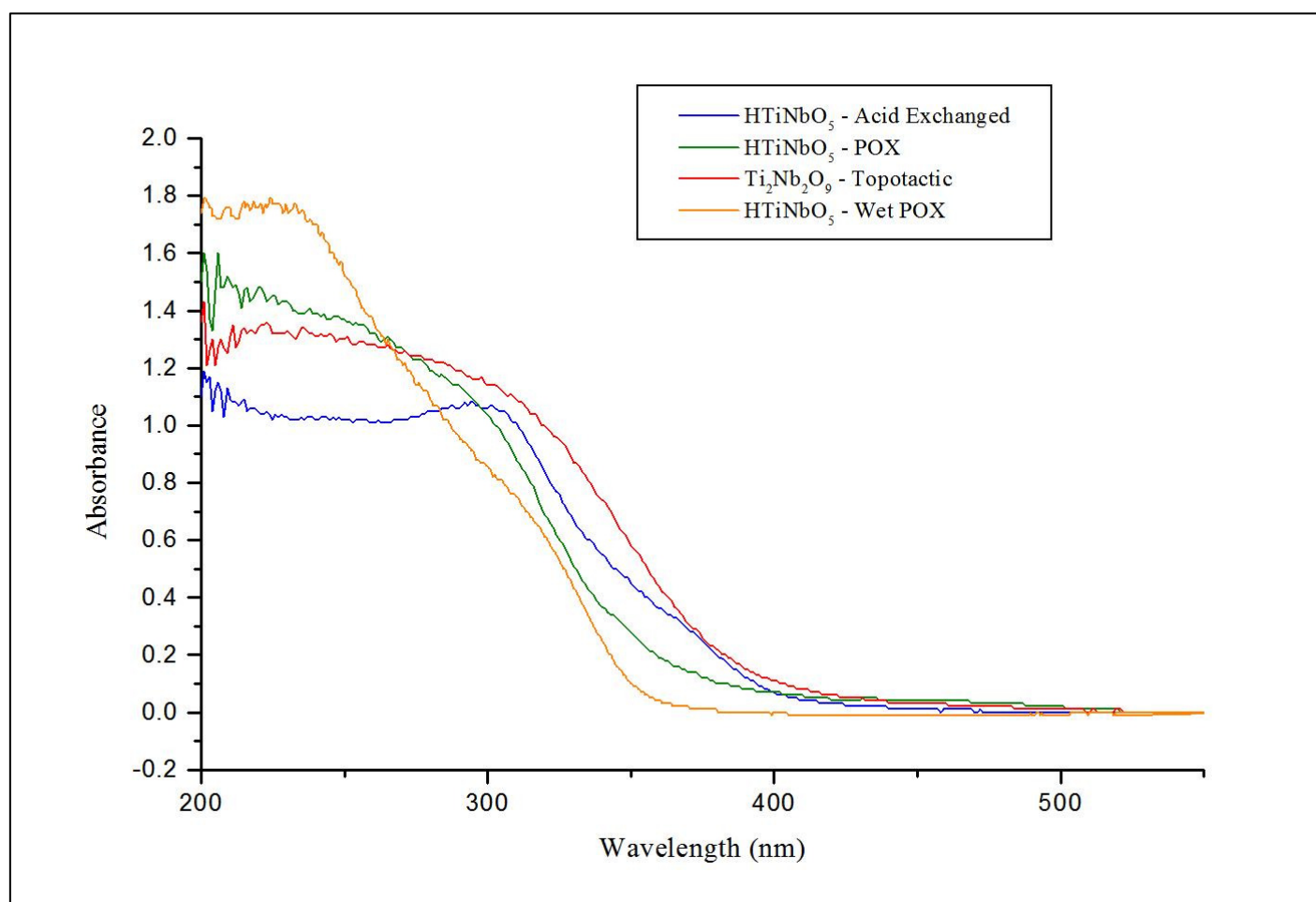


Figure 4.16: UV-VIS reflectance graph for HTiNbO_5

In topotactic dehydrated materials, the metal oxide sheets behave as if they were glued together like the bulk materials, similar to acid exchanged materials, and provide a red shifted absorption. However the POX materials have random metal oxide sheets connected by ionic bonds. So they have

less bulky properties in compare to acid exchanged materials or topotactic dehydrated materials. In wet POX the metal oxide sheets have very loose connection between themselves and presence of plenty water molecules allows them high degrees of movement which lead them to a state as if they were nanoparticles. Consequently, wet POX shows the most blue shifted absorption compare to others which follows by POX materials and then acid exchanged or topotactic dehydrated materials (Figure 4.16 and 4.17).

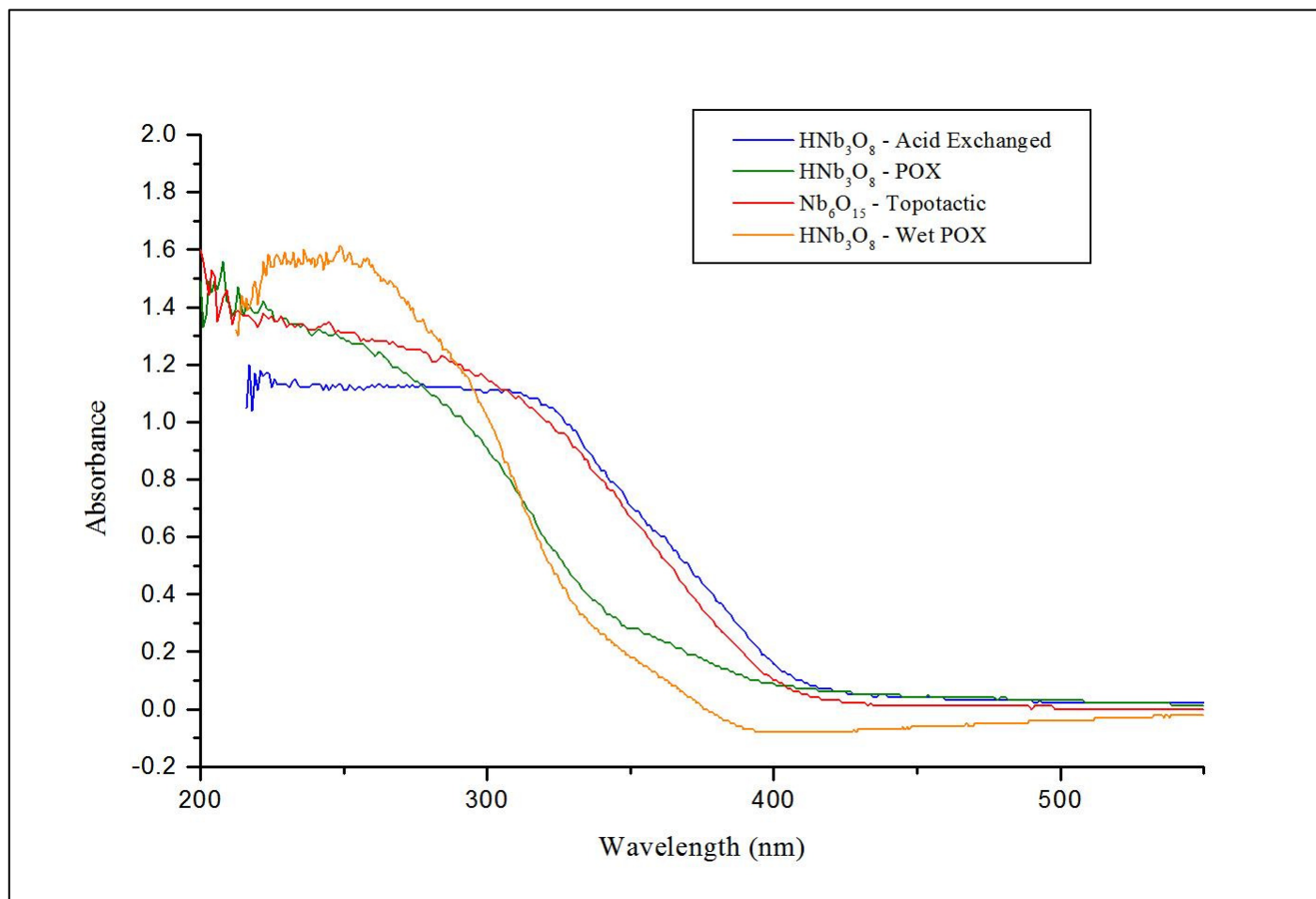


Figure 4.17: UV-VIS reflectance graph for HNb_3O_8

4.5 X-ray fluorescence spectrometry

X-ray fluorescence spectrometry of POX materials were done by XDAL, Fischerscope X-ray system (Västra Frolunda, Sweden) in Dr. Gardea's lab in the Department of Chemistry at UTEP. Measurements show the peaks for the presence of Ti and Nb elements in the POX materials (Figure 4.18 and 4.19).

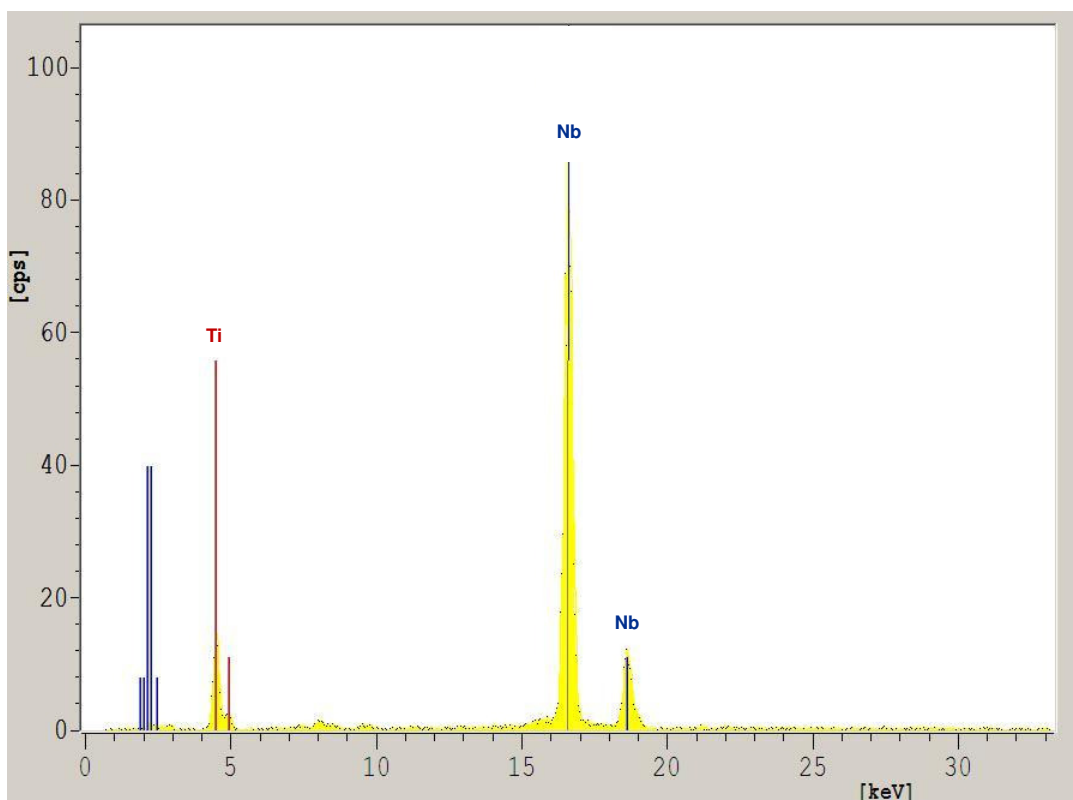


Figure 4.18: X-ray fluorescence image of POX-HTiNbO₅.

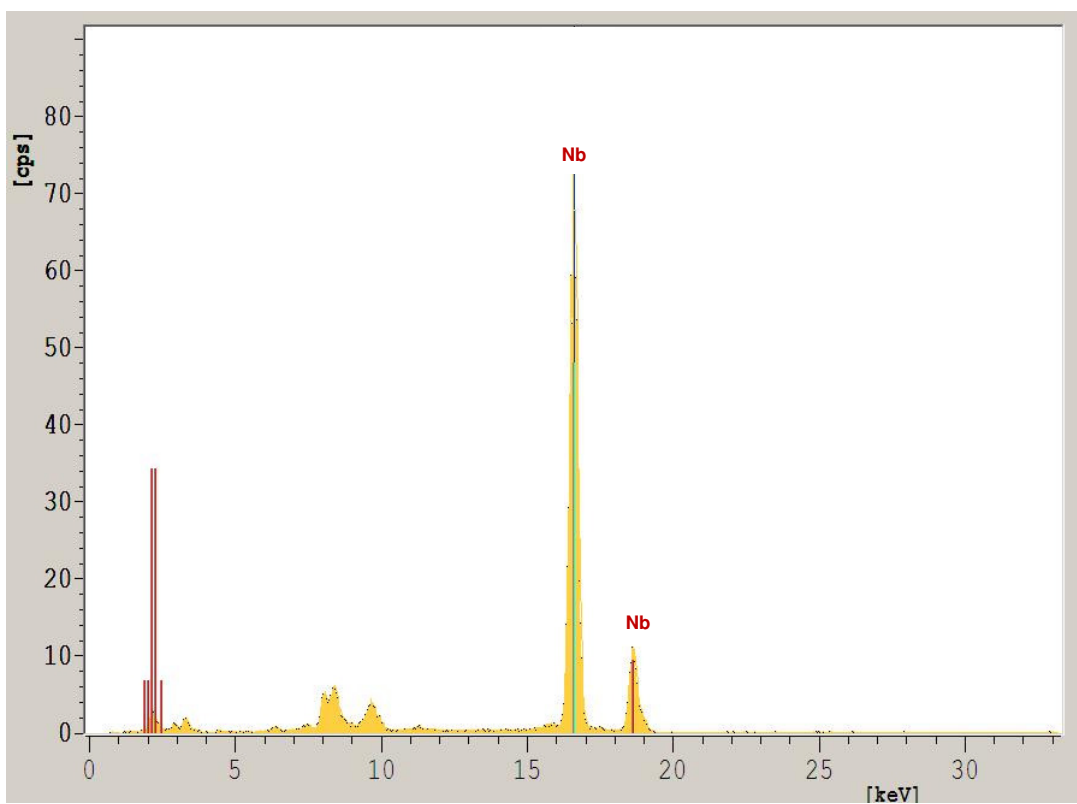


Figure 4.19: X-ray fluorescence image of POX-HNb₃O₈.

4.6 Scanning electron microscopy

The morphology of POX materials was studied using a shared scanning electron microscope system (S-4800, Hitachi, Japan) housed in the Department of Metallurgical and Materials Engineering at UTEP.

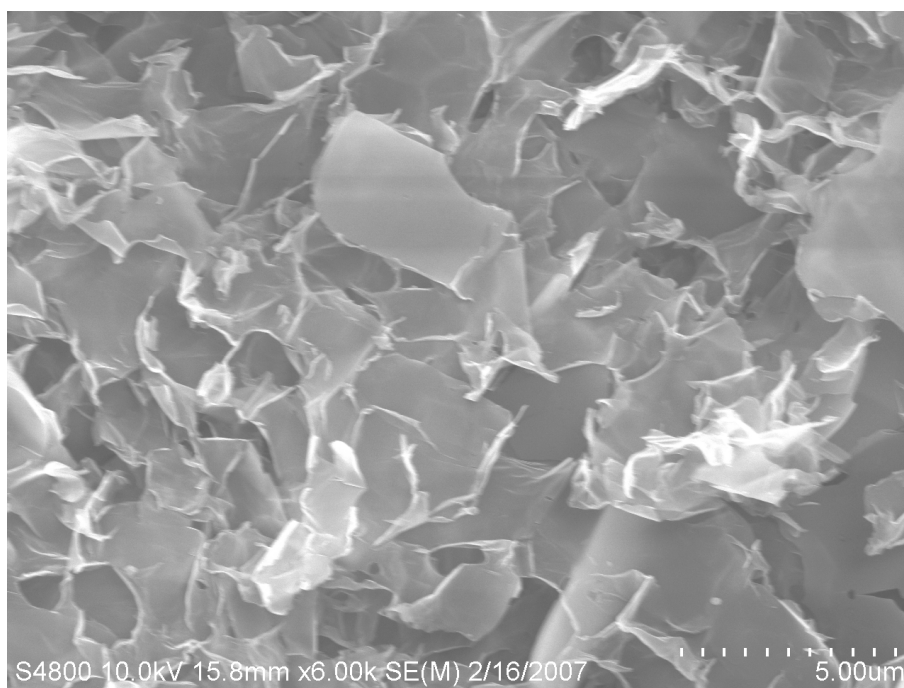


Figure 4.20: SEM image of POX-HTiNbO₅.

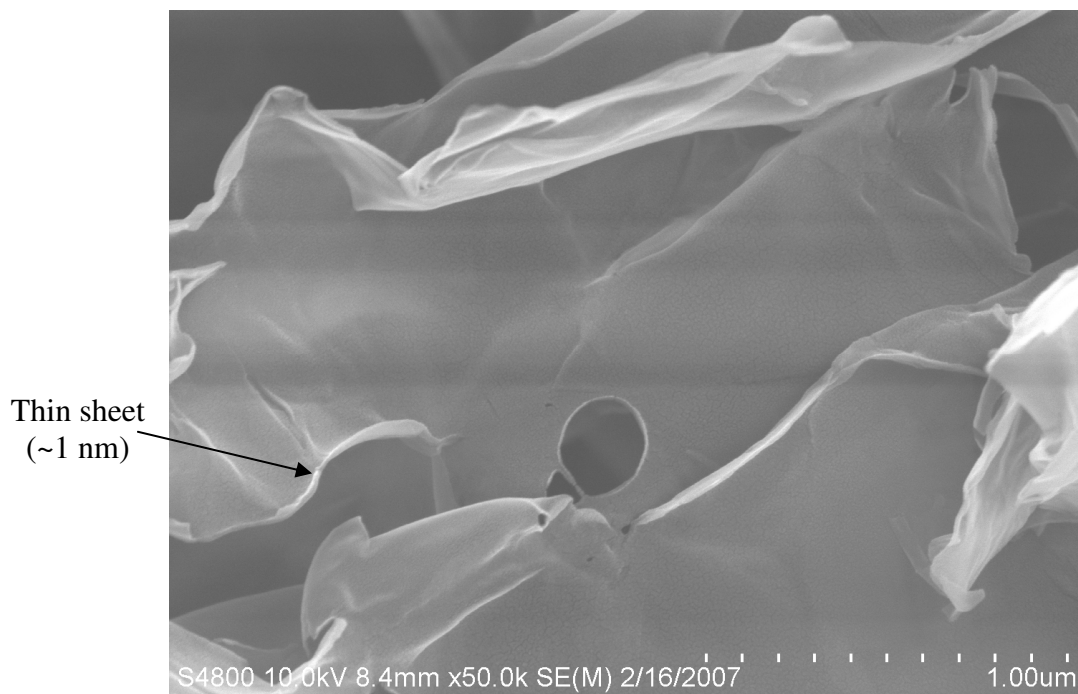


Figure 4.21: SEM image of POX-HTiNbO₅.

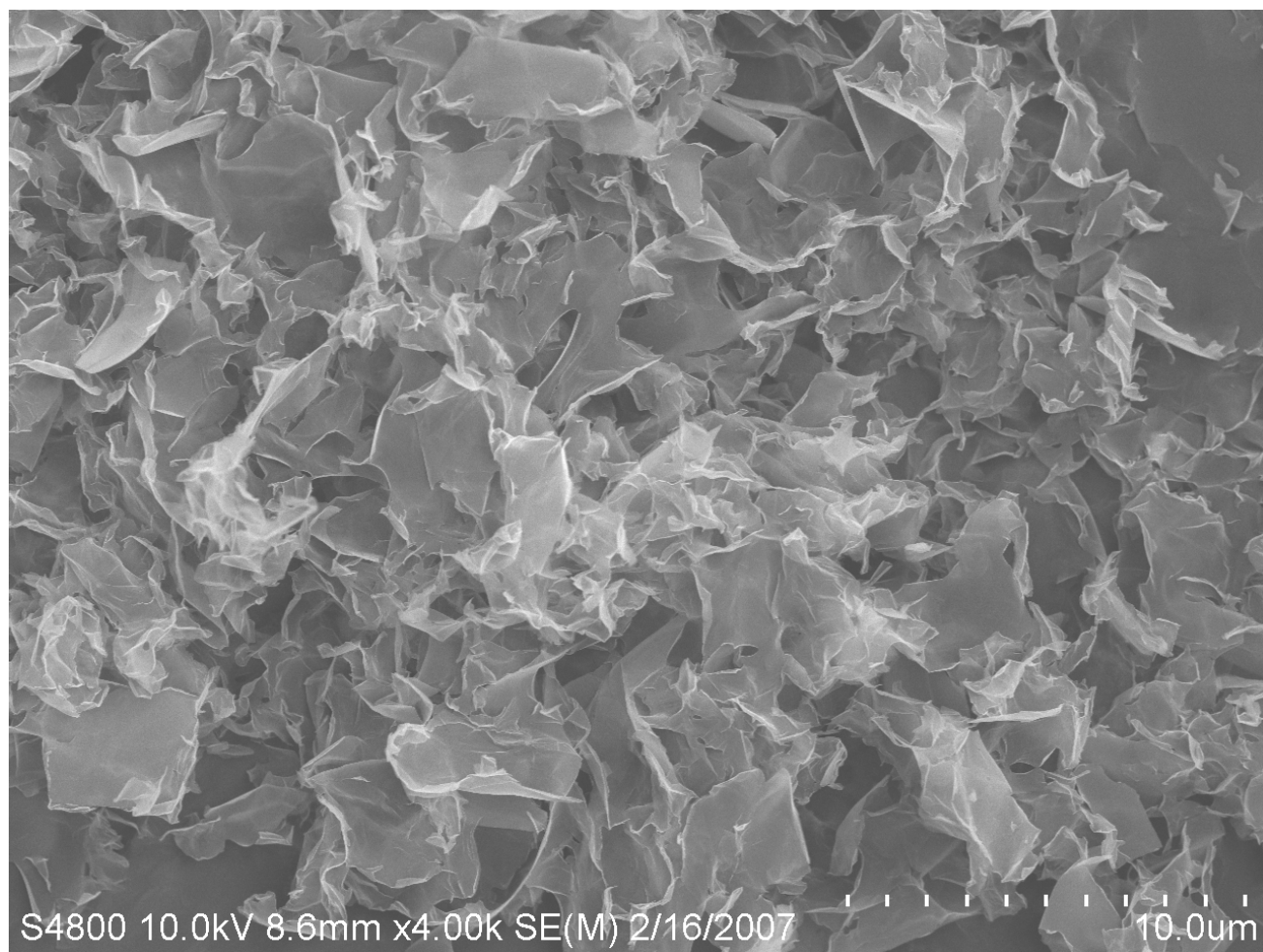
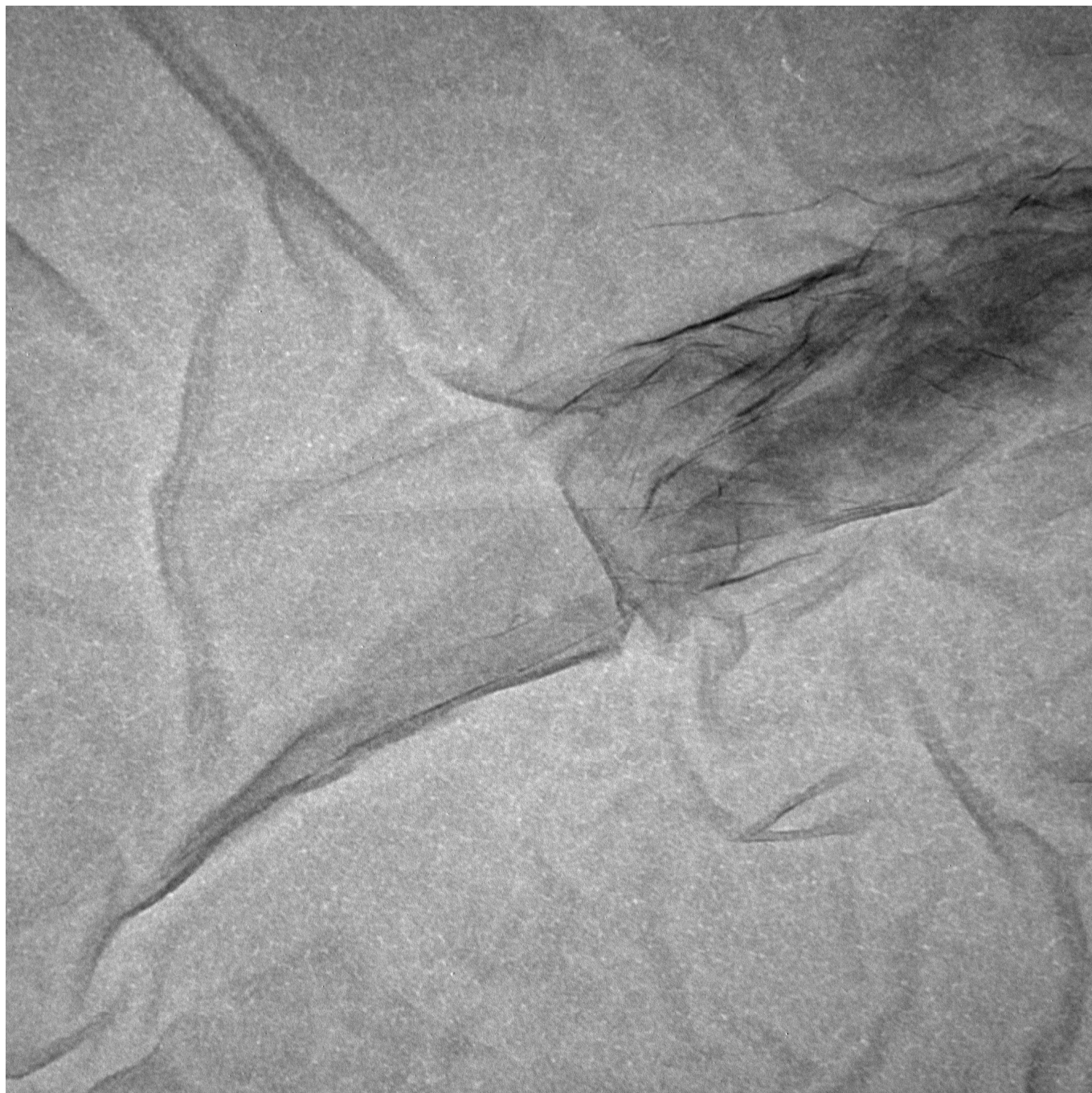


Figure 4.22: SEM image of POX-HNb₃O₈

The SEM analysis reveals that the POX materials have a high surface area open frame structure, with large pores and very thin pore walls (Figure 4.20 – 4.22), giving the materials a very unique characteristics. The SEM images also show that the thin sheets are aggregated to make porous metal oxide composites. Sheet thickness was estimated to about 1 nm (Figure 4.21).

4.7 Transmission electron microscopy

Transmission electron microscopy of the POX materials were done using shared TEM system (H-9500, Hitachi, Japan) housed in the department of Metallurgical and Materials Engineering at UTEP. TEM samples were prepared by diluting exfoliated colloidal HTiNbO₅ and HNb₃O₈ materials.



Masud.007

Print Mag: 259000x @ 8.3 in

2:03:02 p 12/09/09

TEM Mode: Imaging

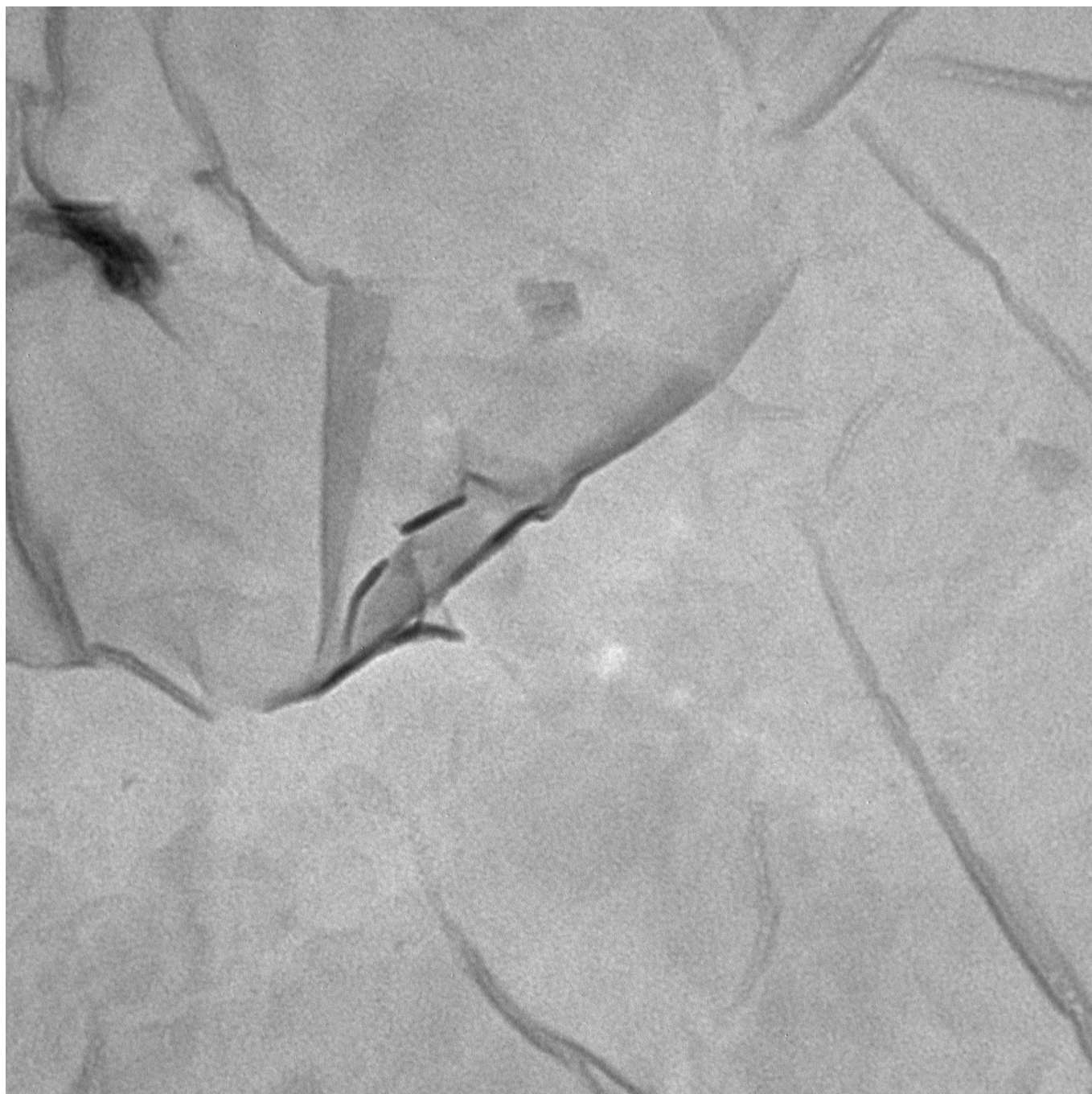
100 nm

HV=300.0kV

Direct Mag: 30000x

AMT Camera System

Figure 4.23: TEM image of exfoliated colloidal HTiNbO₅ materials.



Masud.032

Print Mag: 138000x @ 8.3 in

2:48:31 p 12/09/09

TEM Mode: Imaging

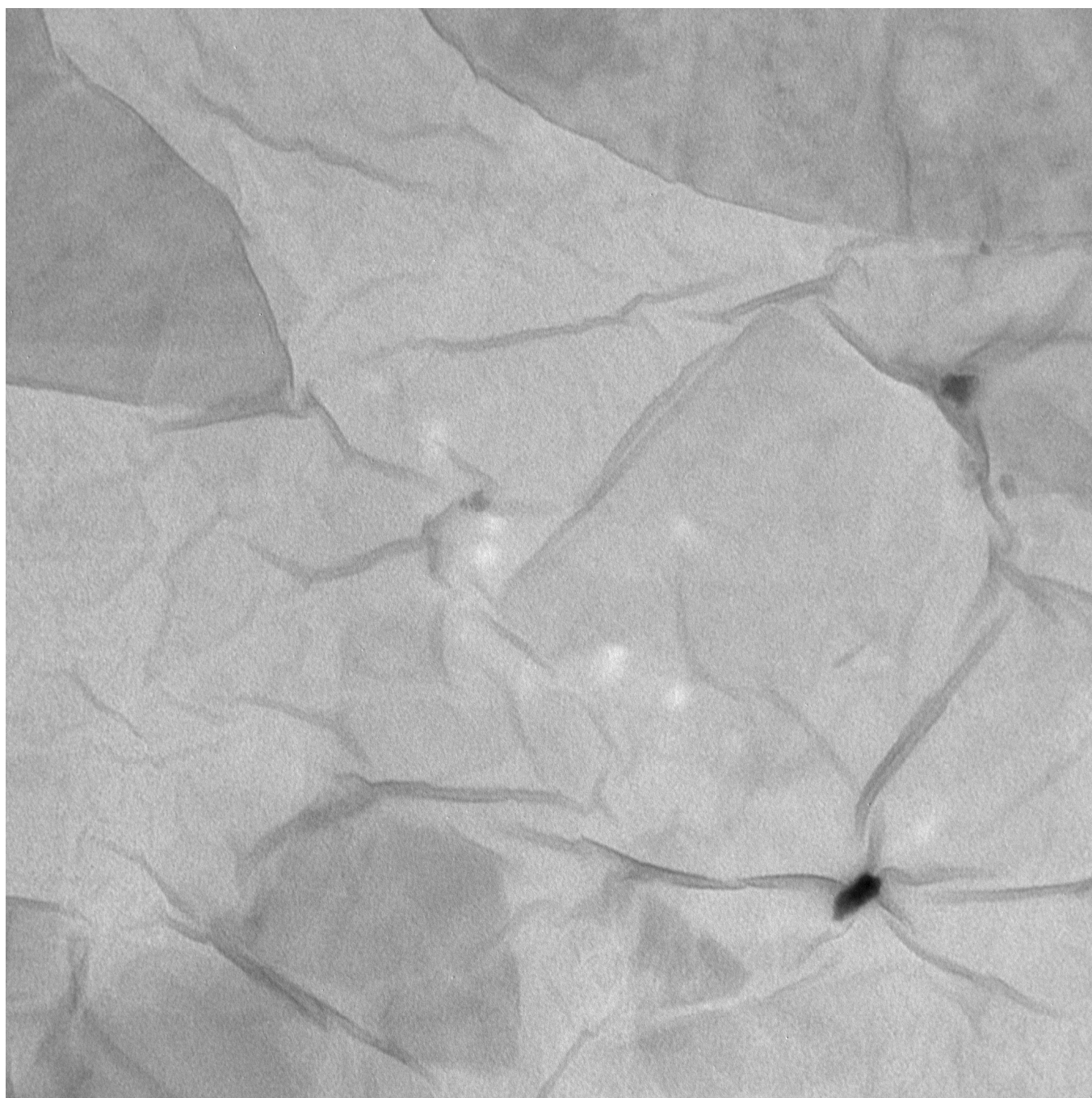
100 nm

HV=300.0kV

Direct Mag: 15000x

AMT Camera System

Figure 4.24: TEM image of exfoliated HNb_3O_8 materials.



Masud.039

Print Mag: 92900x @ 8.3 in

2:59:50 p 12/09/09

TEM Mode: Imaging

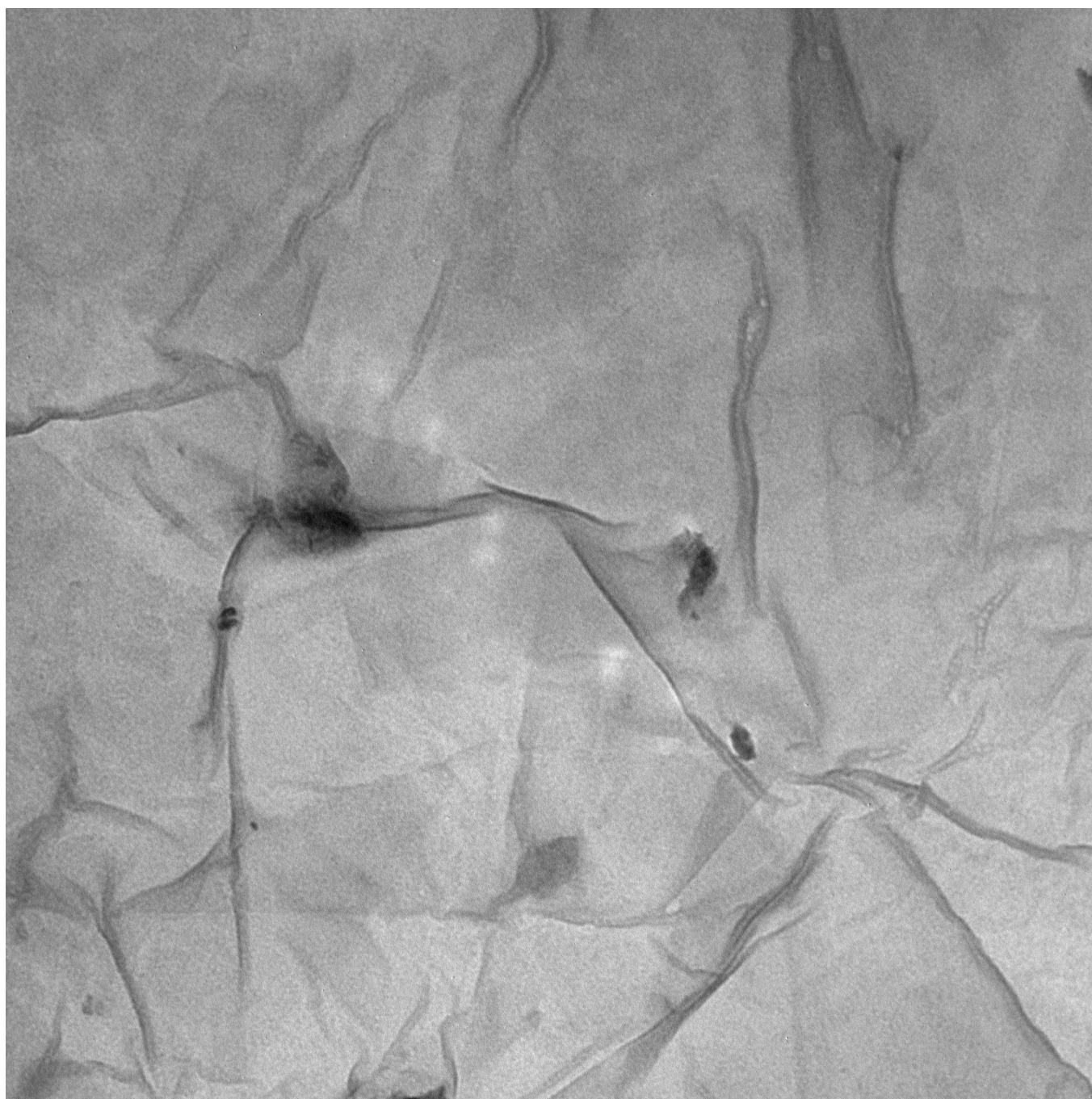
500 nm

HV=300.0kV

Direct Mag: 10000x

AMT Camera System

Figure 4.25: TEM image of exfoliated colloidal HNb₃O₈ materials.



Masud.041

Print Mag: 92900x @ 8.3 in

3:02:17 p 12/09/09

TEM Mode: Imaging

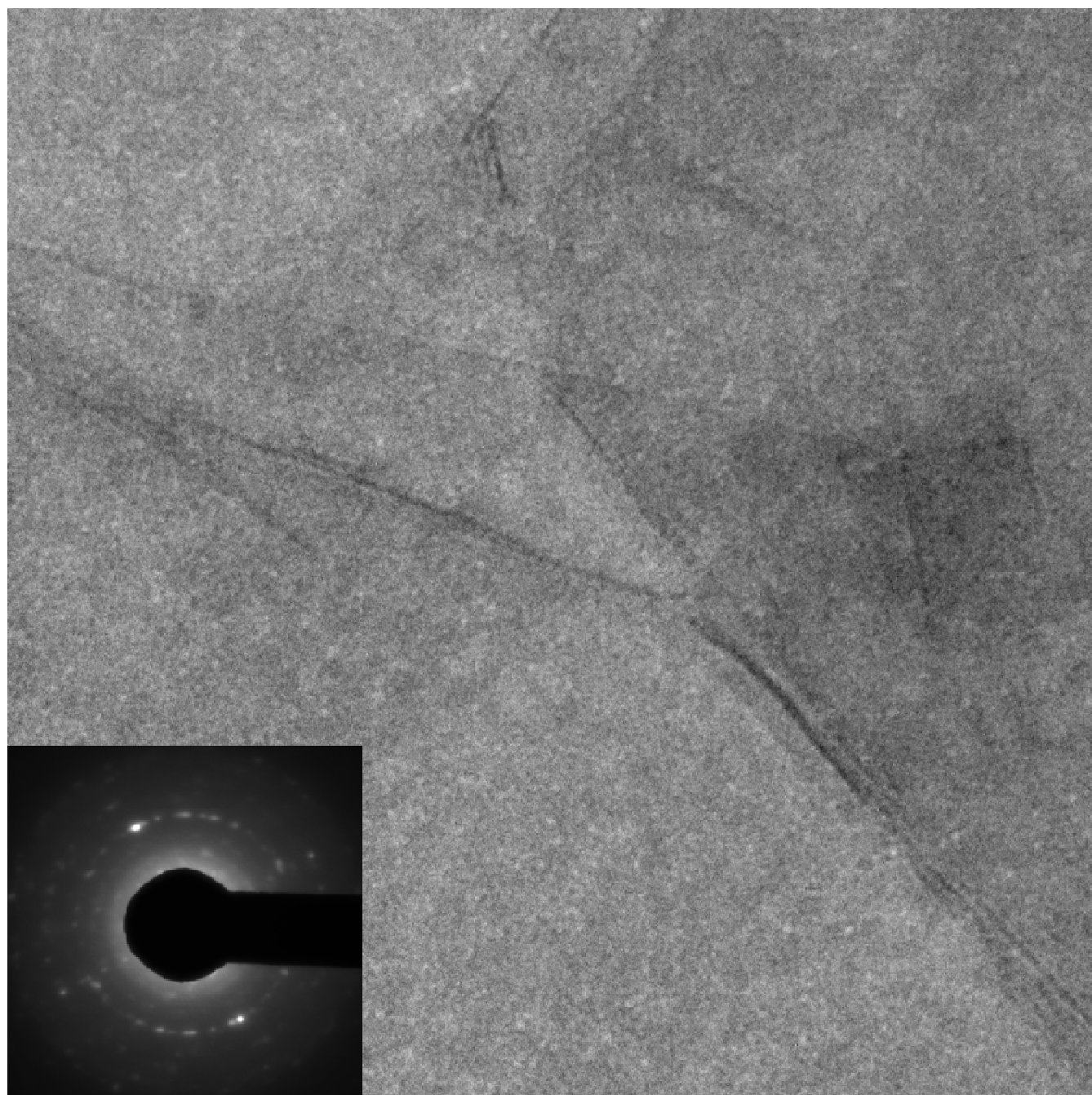
500 nm

HV=300.0kV

Direct Mag: 10000x

AMT Camera System

Figure 4.26: TEM image of exfoliated colloidal HNb₃O₈ materials.



5 Angstroms

HV=300.0kV

Cam Len: 0.25 m

AMT Camera System

TEM Mode: Diffraction

Masud.044

Print Mag: 676000x @ 8.3 in

3:10:53 p 12/09/09

TEM Mode: Imaging

20 nm

HV=300.0kV

Direct Mag: 60000x

AMT Camera System

Figure 4.27: TEM image of exfoliated colloidal HNb_3O_8 material at high magnification. An electron diffraction pattern is shown in the inset.

TEM analysis of the exfoliated colloidal materials shows that the sheets are aggregated, folded, folded and wrinkled which lead to random porosity of the materials (Figure 4.23 – 4.27). Sometimes the unexfoliated particles help to make wrinkles (Figure 4.25 and 4.26). At high magnification the sheet thickness was estimated to at about 1 nm (Figure 4.27). The diffraction pattern shows that the materials are composed of polycrystalline materials (Figure 4.27).

4.8 ICP-OES analysis

The metal oxide catalysts were characterized by ICP-OES instrument. The presence of Ti, Nb and K elements were verified and the ratios of Nb to Ti were calculated to check whether their atomic proportion remains same in the catalyst as it is in the molecule. The POX samples were dissolved in HF and diluted for analysis in the Inductively Coupled Plasma-Optical Emission Spectroscopy.

Table 4.2: ICP-OES analysis of metal oxide catalysts

Types of Sample	Ti (ppm)	Nb (ppm)	K (ppm)	Nb/Ti
HNb ₃ O ₈ -POX	0	1.25	0.015	-
HTiNbO ₅ -POX	2.089	4.17	0.028	1.96
HTiNbO ₅ -Topo	1.66	3.24	0.016	1.94
HNb ₃ O ₈ -Topo	0	2.74	0.024	-

ICP analysis of POX materials shows that there is some potassium present in the samples although there have been four consecutive batches of acid exchange done on the parent KTiNbO₅/KNb₃O₈ materials to get HTiNbO₅/HNb₃O₈. In one molecule of HTiNbO₅, the ratio of Nb to Ti is 1.94 and ICP analysis reveals that the ratio of Nb to Ti is 1.94-1.96.

4.9 Elemental analysis

The elemental analysis of POX materials was done by Quantitative Technologies, Inc (NJ, USA) to check the presence of C, H and N. Two different types of samples were analyzed. HTiNbO₅/ HNb₃O₈-POX samples are regular samples that are dried using critical point CO₂ dryer and HTiNbO₅/ HNb₃O₈-wet samples are dried in air.

Table 4.3: Elemental analysis of metal oxide catalysts

Types of Sample	% C	% H	% N
HNb ₃ O ₈ -POX	1.76	0.89	0.09
HTiNbO ₅ -POX	1.80	1.07	0.06
HTiNbO ₅ -wet	0.29	0.4	<0.05
HNb ₃ O ₈ -wet	0.53	0.68	<0.05

The elemental analysis shows that there are some C and N present in both POX and wet samples. The TBA (tetra butyl ammonium hydroxide) was used to exfoliate HTiNbO₅/ HNb₃O₈ sheets during the synthesis process of POX. Some residue of TBA may contribute to these numbers for C and N.

4.10 Conclusion

Characterization of metal oxide catalysts at different stages of its synthesis process was done to assess their functionality and useful structure. It also helped to verify the samples, their chemical constituents, and physicochemical behaviors.

Chapter five: Metal reduction and hydrogen production under UV light

5.1 Introduction

The POX materials were investigated for their photocatalytic activity in ultraviolet light by photoreducing metals out of their solution. Two different metals ions, Pt^{+4} and Au^{+3} from solutions of H_2PtCl_6 and HAuCl_4 respectively, were reduced into their metallic states and deposited onto the surfaces of the POX materials. The kinetic study of these reduction processes helped compare the photocatalytic behavior of two different POX materials: HTiNbO_5 and HNb_3O_8 , reduction potentials of Pt^{+4} over Au^{+3} , observe the electronic conduction pattern of the materials, and understand the active sites of the POX materials.

5.2 Experimental setup

Photochemical metal reduction was done by placing 0.015 g of POX-HTiNbO_5 or $\text{POX-HNb}_3\text{O}_8$ and the required amount of aqueous 100 ppm (varied for different percent loading) platinum or gold solution (EM Science, USA, 1000 ppm ICP standard) into a 16 cm long customized quartz tube. 1.0 mL of anhydrous ethanol (Sigma-Aldrich, St. Louis, MO, USA) was added as an electron donor and then the tube was sealed at the top with a rubber septum (Chemglass, Vineland, NJ, USA). The solution mixture's pHs prior to irradiations were found to be 1.5-2.0. Argon gas was used to purge the solution and head space gasses for 15 minutes to remove any dissolved oxygen, using needles through the septum. A Penray (UVP LLC, USA) Hg light bulb (UV pen lamp, model 35C-9, rated 5.4 mW/cm^2 @19 mm @254 nm) was used to irradiate the samples with UV light at 20 mm distance (face of bulb to face of quartz tube).

Metal reduction onto the surfaces of the POX materials occurred during the UV irradiation experiments, and the amount of metal removed from solution was taken to indicate the amount of metal deposited. Quantification of metal reduction and deposition kinetics was done using inductively coupled plasma optical emission spectroscopy (ICP-OES, Perkin Elmer, Optima 4300 DV, Norwalk, CT, USA) and flame atomic absorption spectroscopy (FAAS, Perkin Elmer 5100 C, USA) using standard

protocols. Scanning electron microscopy (SEM, S-4800, Hitachi, Japan) was used to determine the particle size of the reduced metal and the metal deposition pattern. Optical absorption spectroscopy in diffuse reflectance mode (UV-Vis, UV-3101 PC, Shimadzu, Japan) was used to check for plasmon absorption bands from the metals on the oxides. The amount of hydrogen evolved during metal reduction by POX materials was measured using a gas chromatograph (series 350, thermal conductivity detector, Gow-Mac Instrument Company, Bethlehem, PA, USA). A sample lock syringe (Gastight-1750, Hamilton Company, Nevada, USA) was used to withdraw gas samples from the quartz tube. A data acquisition instrument (USB-1208FS, Measurement Computing, MA, USA) was used to convert analog signal into digital values to be plotted as a computer generated graph and a customized amplifier was placed between gas chromatograph and data acquisition instrument to amplify the signal.

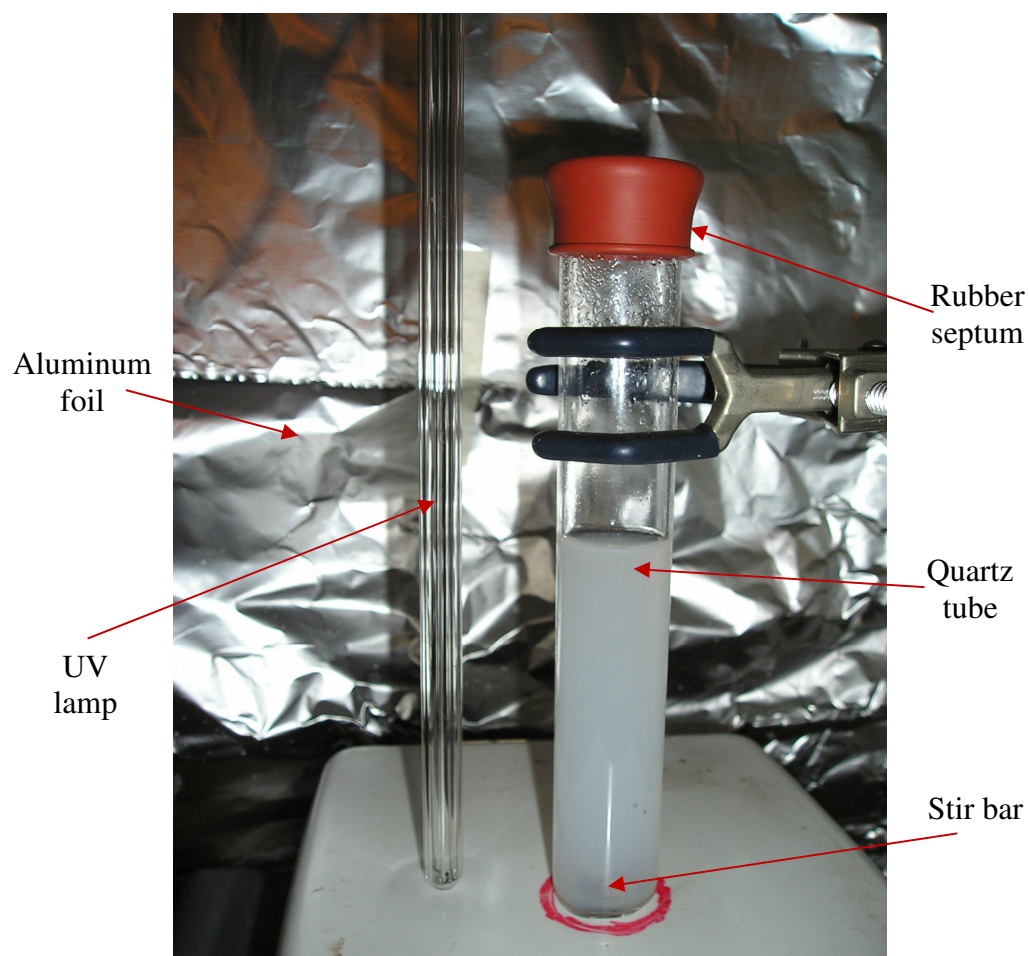


Figure 5.1: Experimental setup for UV light assisted H_2 evolution and metal reduction.

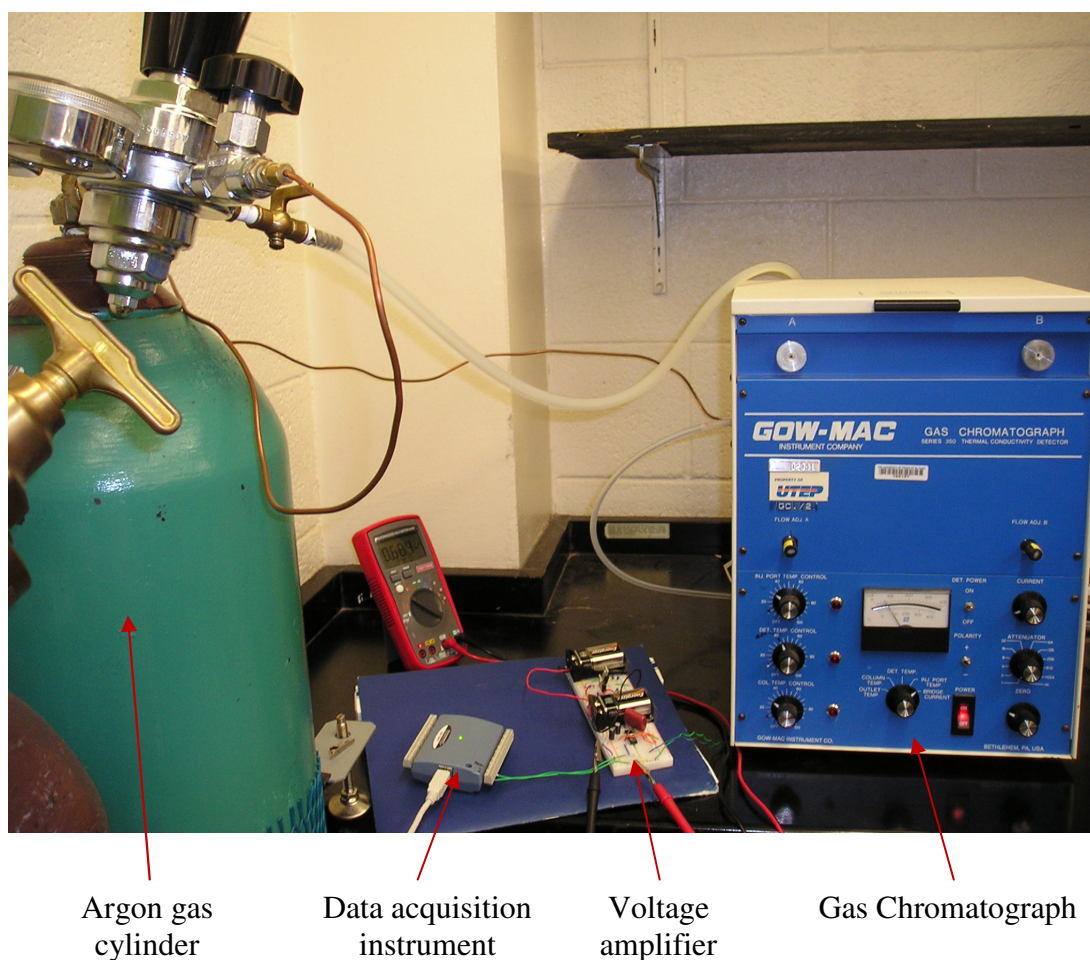


Figure 5.2: Gas chromatograph setup for measuring evolved H₂.

5.3 Metal reduction

Au⁺³ and Pt⁺⁴ metal ions were reduced to their metallic states and deposited onto the surfaces of POX materials. POX-HTiNbO₅, POX-HNb₃O₈ and topotactic dehydrated Nb₆O₁₅ and Ti₂Nb₂O₉ were tested for their ability to reduce these metal ions. Kinetic study of metal reduction process was done by flame atomic absorption spectroscopy (FAAS, Perkin Elmer 5100 C, U.S.A.) in the Department of Chemistry at UTEP. Periodically 4 mL samples were withdrawn from the quartz tube, centrifuged and the liquid phase was separated to measure unreduced metal ions and solid phase was rinsed and centrifuged twice and dissolved in hydrofluoric acid (HF) to measure deposited metals. A portion of solid phase was kept to analyze in scanning electron microscope to measure the metal particle size distribution, deposition pattern and preference of metal deposition in POX materials.

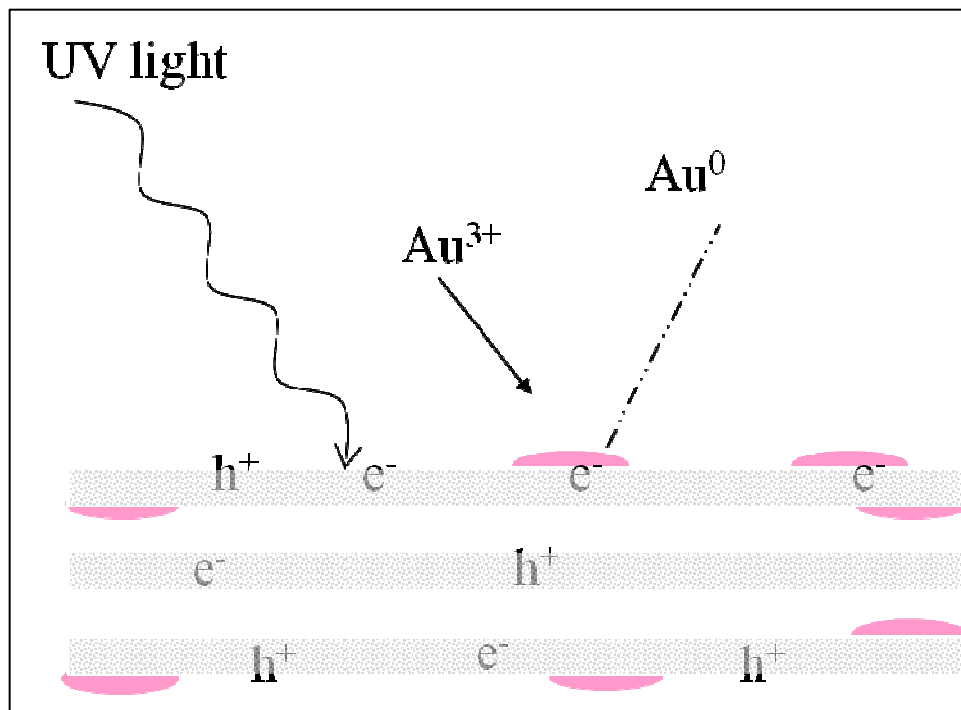


Illustration 5.1: Au metal reduction under UV light.

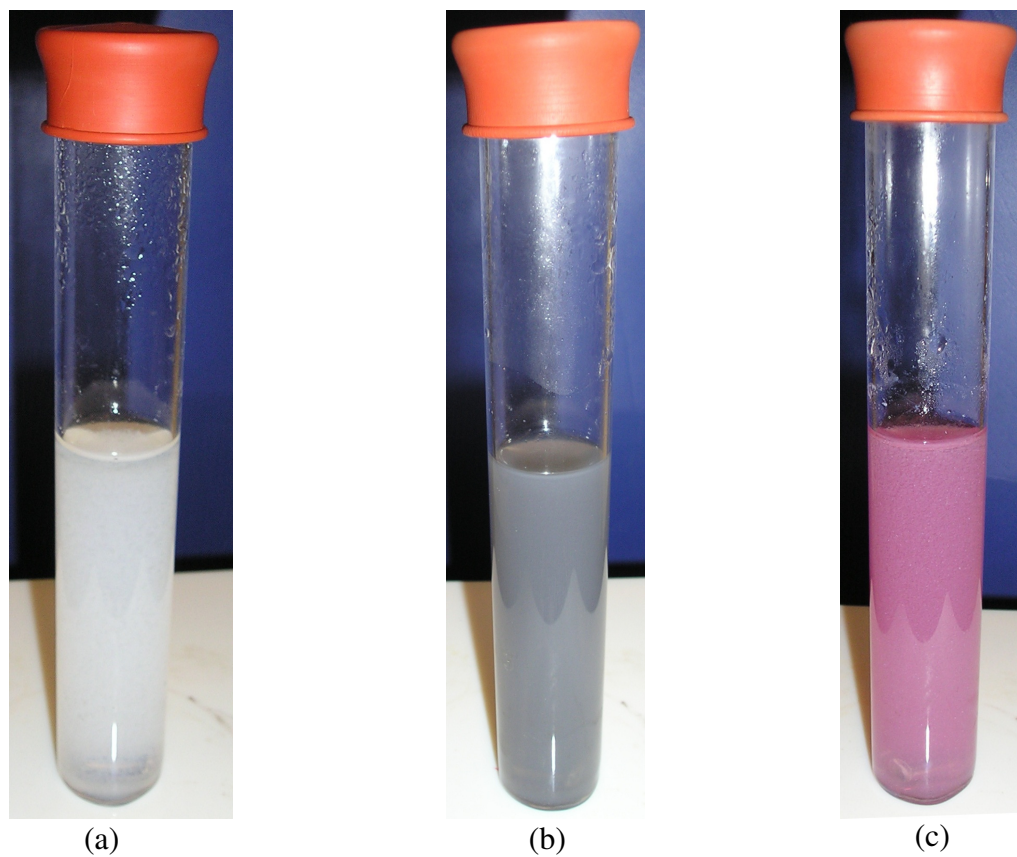


Figure 5.3: Metal reduction under UV light – (a) white POX materials before metal reduction, (b) dark grey POX materials after Pt reduction and (c) pink/red POX materials after Au reduction.

5.3.1 Kinetics of metal reduction

Kinetic studies of metal reduction by POX and topotactic dehydrated materials were done for 5% metal loading condition. 7.5 mL of 100 ppm ICP standard HAuCl_4 and H_2PtCl_6 solution was added with 0.015 gm of materials and then 22.5 mL of 0.2% HNO_3 was added to get the recipe of 5% gold metal loading and 5% platinum metal loading respectively. 1.0 mL of anhydrous EtOH was added as an electron donor.

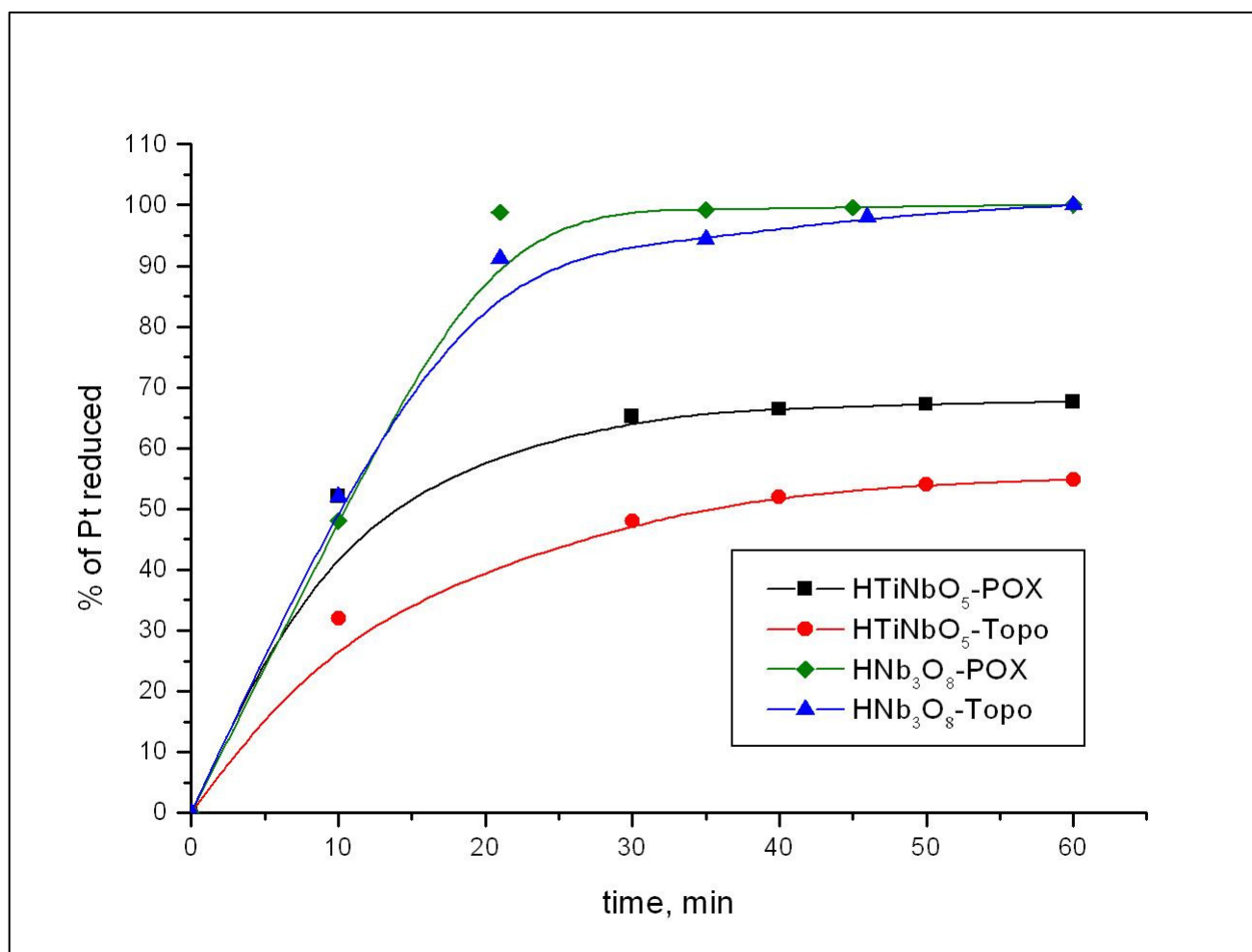


Figure 5.4: Kinetic study of Pt metal reduction under UV light

Figure 5.4 shows that Pt is more readily reduced in HNb_3O_8 materials compared to HTiNbO_5 materials which may be because of the band gap difference between these two types of materials. Within 30 minutes most of the available Pt cations were reduced on HNb_3O_8 materials, whereas in 60 minutes

Pt reduction was not more than 50-60% complete on HTiNbO₅. Topotactic dehydrated materials appear to be less sensitive for Pt reduction compared to POX ones.

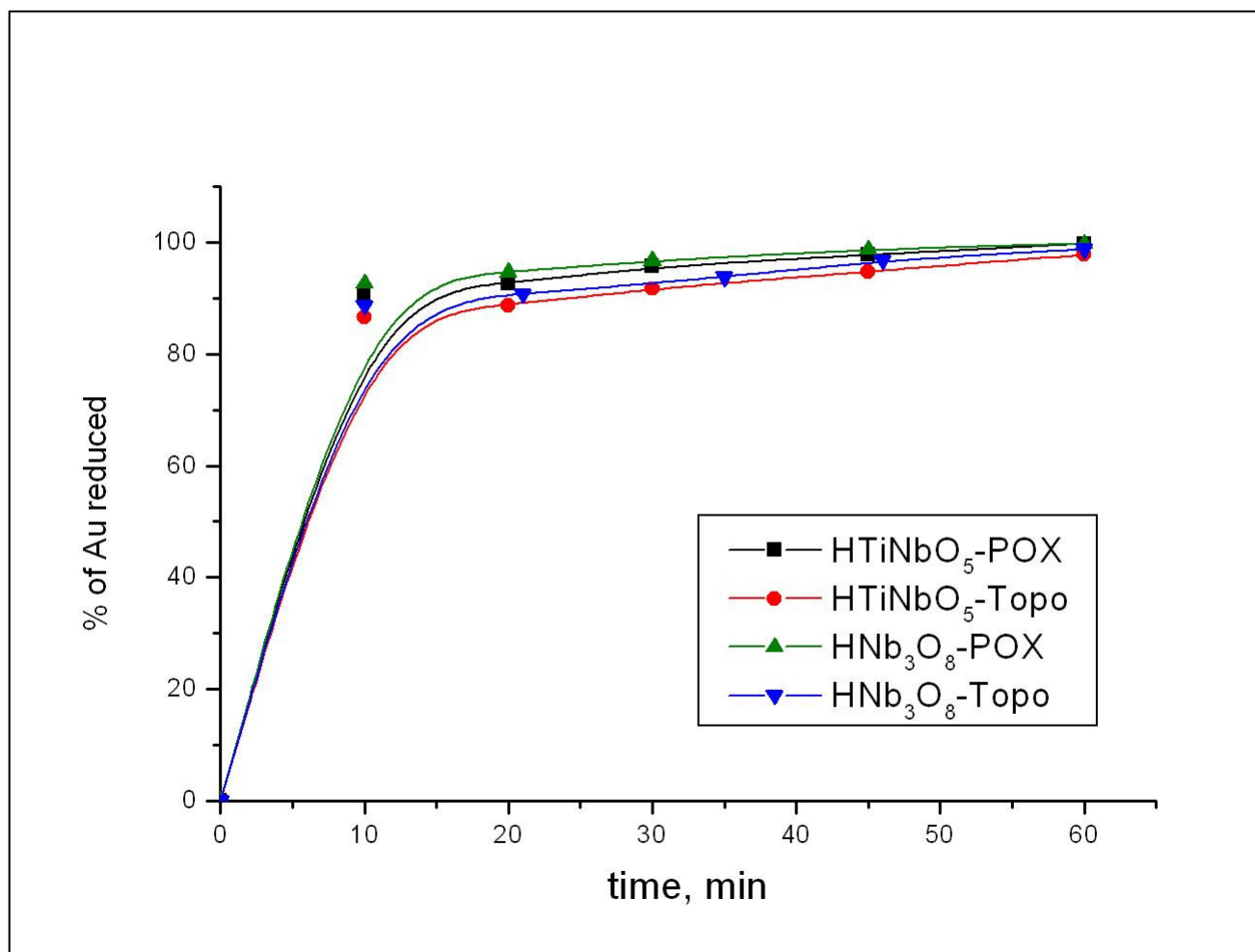
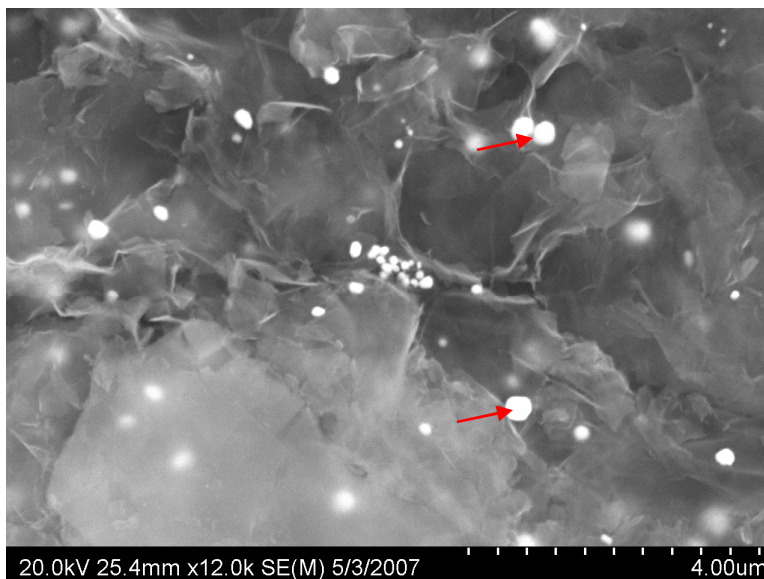


Figure 5.5: Kinetic study of Au metal reduction under UV light

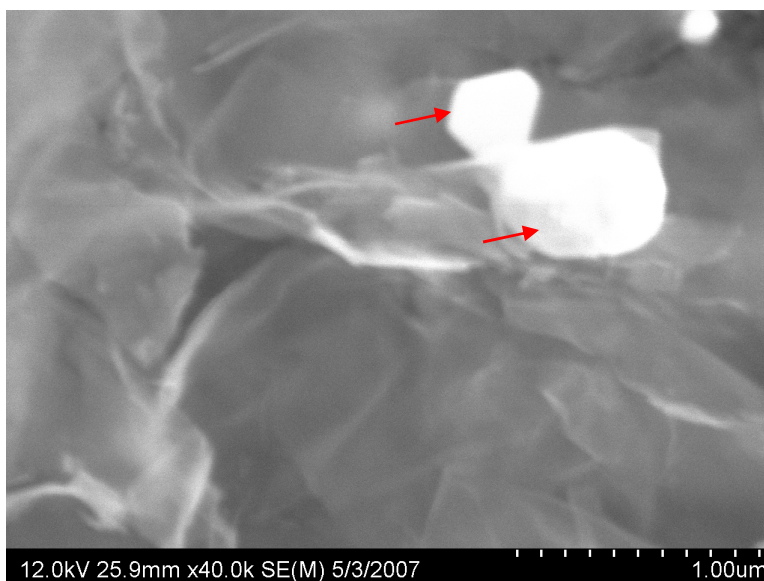
Figure 5.5 shows that Au is very quickly reduced over both HTiNbO₅ and HNb₃O₈ materials and within 15 minutes 90% of Au is reduced. Au³⁺ in HAuCl₄ solution has higher reduction potential (1.002V vs. NHE) compared to Pt⁴⁺ (0.68V vs. NHE) in H₂PtCl₆ solution.⁴ This is the reason why Au reduction is faster and more complete than the Pt reduction. The UV-VIS-NIR reflectance spectroscopic analysis revealed that HNb₃O₈ (3.10 eV) has higher band gap than the HTiNbO₅ (3.03 eV) materials and probably this is the reason for Pt reduction was more complete by HNb₃O₈ materials than its counterpart HTiNbO₅ materials.

5.3.2 SEM analysis of metal deposited solid materials

Pt and Au deposited POX materials were rinsed with water, dried in air and examined in scanning electron microscope to determine the metal particles size distribution, deposition pattern and preference.

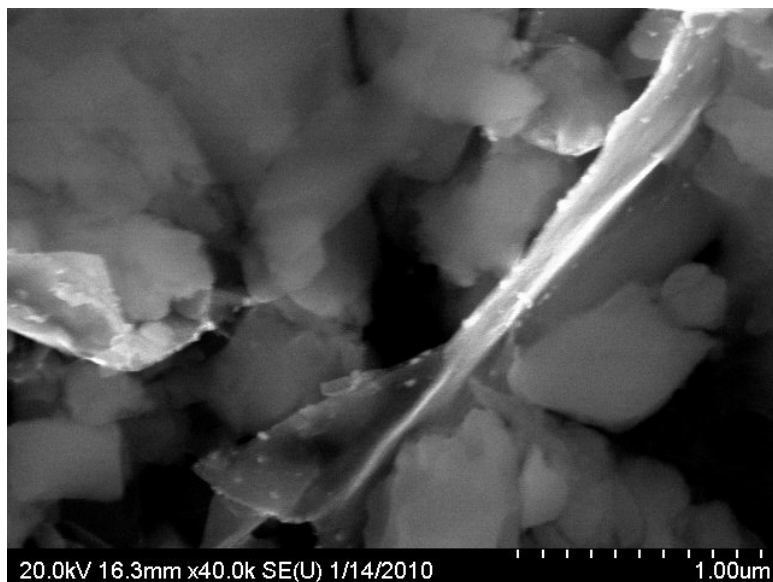


(a)

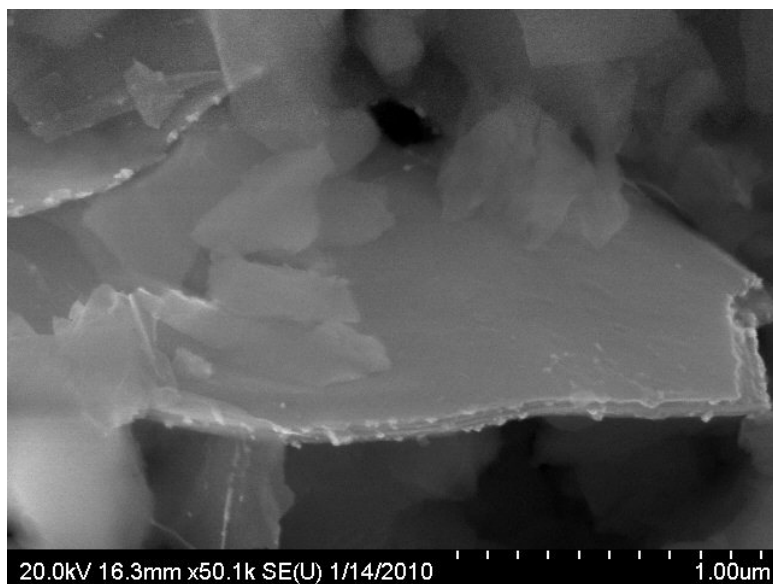


(b)

Figure 5.6: SEM analysis of Au deposited HTiNbO₅. (a) Au reduces without any preferences and (b) reduced gold particles grow and make nice facet.



(a)



(b)

Figure 5.7: (a) and (b) SEM analysis of Pt deposited HTiNbO₅. Pt prefers edges of the sheets.

SEM analysis shows that gold gets reduced and deposited without any preferences however platinum reduction and deposition is preferred along the edges of the sheets. Consequently gold reduced fast and deposits everywhere and then grows the particle size. On the contrary platinum reduction is slow and once it is deposited along the edges then goes elsewhere. Reduced metal particle size distribution is 50-200 nm and 5-50 nm for gold and platinum respectively.

5.4 Hydrogen evolution

Evolved H_2 under UV light metal reduction process was measured using gas chromatograph system. 0.25 mL gas sample from headspace of quartz tube was withdrawn through rubber septum by sample lock syringe.

5.4.1 Calibration curve for H_2 measurement

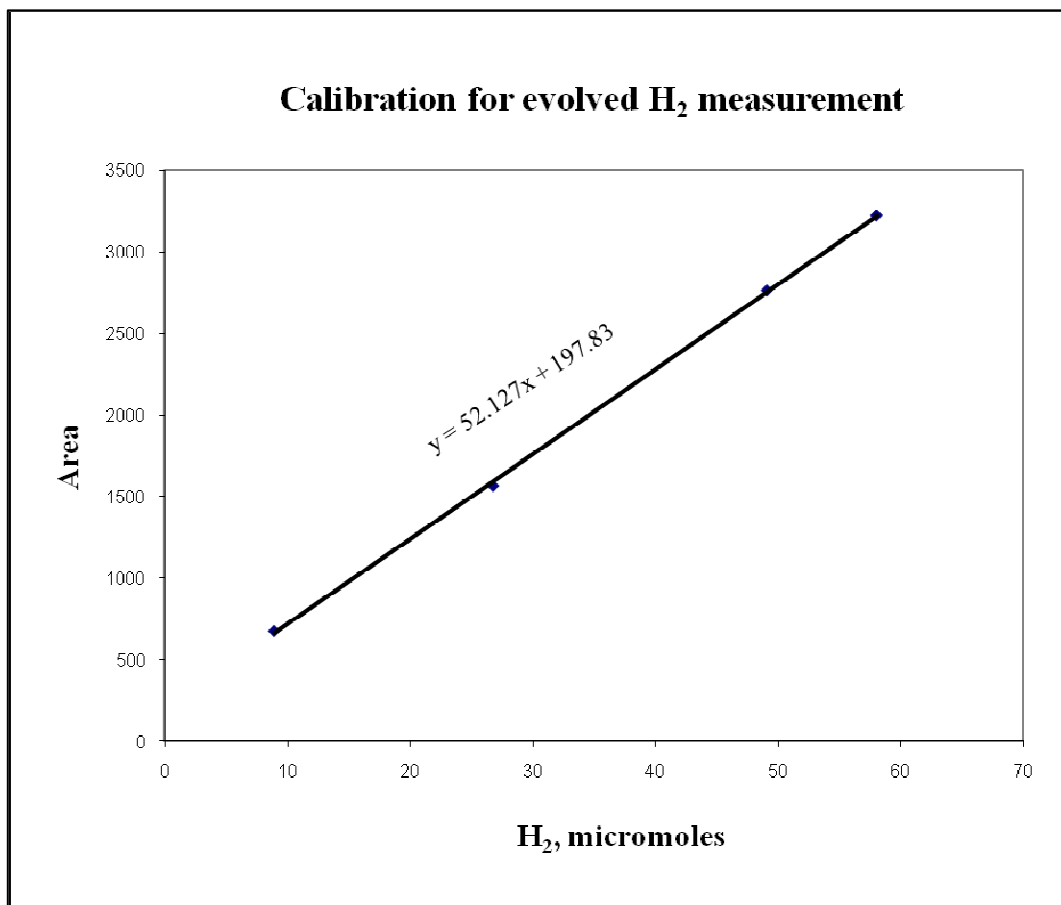


Figure 5.8: Calibration curve for evolved hydrogen gas measurement

Gas chromatograph system was calibrated using standard concentrations of pure H_2 gas. The quartz used for metal reduction under UV light is purged with carrier gas argon to remove air and then standard concentrations of H_2 gas was added. A volume of 0.25 mL was withdrawn through rubber septum for each of the different H_2 concentration.

5.4.2 H₂ evolution by HTiNbO₅ and HNb₃O₈ materials

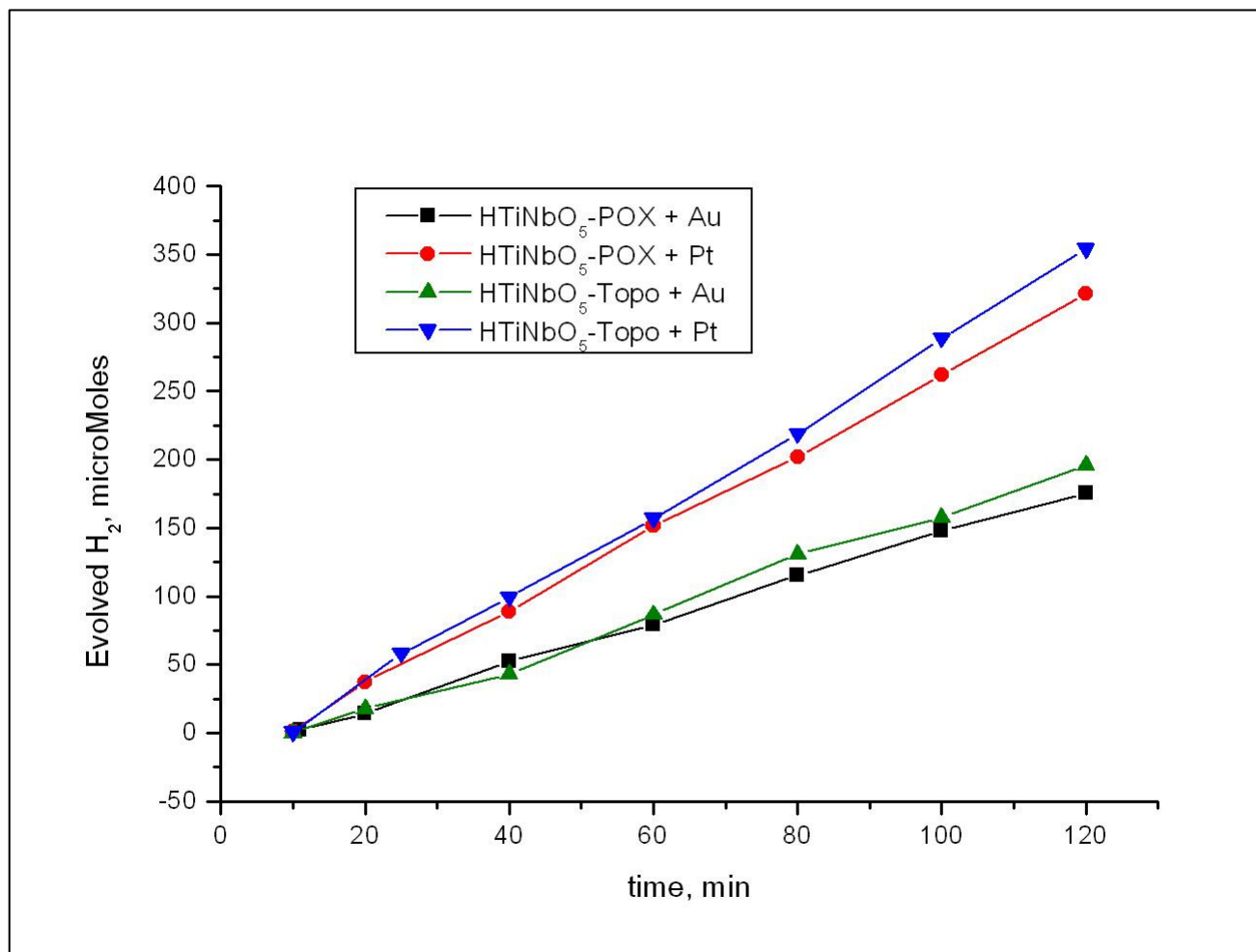


Figure 5.9: Hydrogen evolution by HTiNbO₅ materials under UV light

Figure 5.9 and 5.10 shows that Pt deposited materials are better in hydrogen evolution compare to the Au deposited materials, although Au reduction and deposition was faster and more complete than Pt reduction and deposition (Figure 5.4 and 5.5), which means that although the amount of Pt deposition was lower than the Au deposition, Pt deposited particles acted more efficiently than the Au particles. Pt is a well known catalyst for hydrogen production. So incorporation of Pt particles with POX materials made it a good catalyst composite for hydrogen generation. HNb₃O₈-POX is superior to HTiNbO₅-POX about in two folds. After 120 minutes of UV irradiation, HTiNbO₅-POX produces 321.43 μmol of hydrogen and HNb₃O₈-POX produces 585.46 μmol of hydrogen during the reduction of Pt. This is because of the fact that HNb₃O₈-POX has higher band gap than the HTiNbO₅-POX materials. The

materials characterization experiments by UV-VIS-NIR reflectance spectroscopy showed that the band gap of HNb_3O_8 -POX and HTiNbO_5 -POX is 3.10 eV and 3.07 eV respectively.

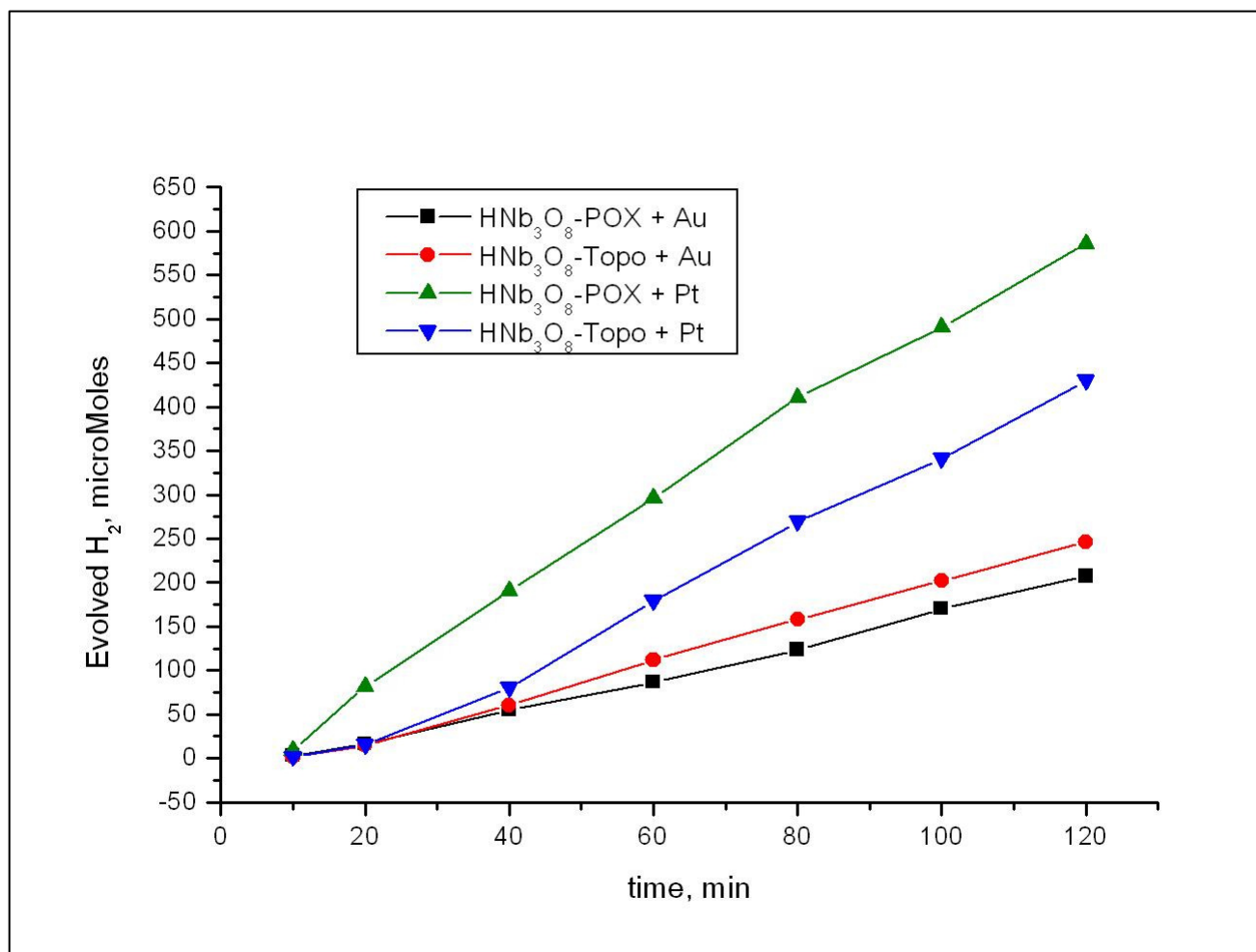


Figure 5.10: Hydrogen evolution by HNb_3O_8 materials under UV light

Topotactic dehydration of POX materials makes a covalent connection between the sheets, which means there is a better electronic conduction. So when an electron is produced in POX materials, due to UV excitation or when an electron is injected by a donor, the electron has limited area of movement due to the two-dimensional nature of the sheets. However, in the topotactic dehydrated structure, the electron can travel from one area to another, in the crystal. Figure 5.9 shows that HTiNbO_5 -Topo materials are better than the HTiNbO_5 -POX materials for both hydrogen production in Pt and Au reduction experiments under UV. However, Figure 5.10 shows that HNb_3O_8 -Topo materials

are better than HfNb_3O_8 -POX materials only for hydrogen production in Au reduction experiments but not for Pt reduction experiments.

5.5 Influence of metal loading on H_2 evolution

Different weight percentage of metal loading (20%, 10%, 7%, 5%, 3%, and 1%) was tested for hydrogen evolution which helped us to determine the optimum metal loading condition. To test a new approach, exfoliated HfNb_3O_8 colloids were also used instead of HfNb_3O_8 -POX materials. Dry HfNb_3O_8 -POX materials are prepared from HfNb_3O_8 colloids and that is already described.

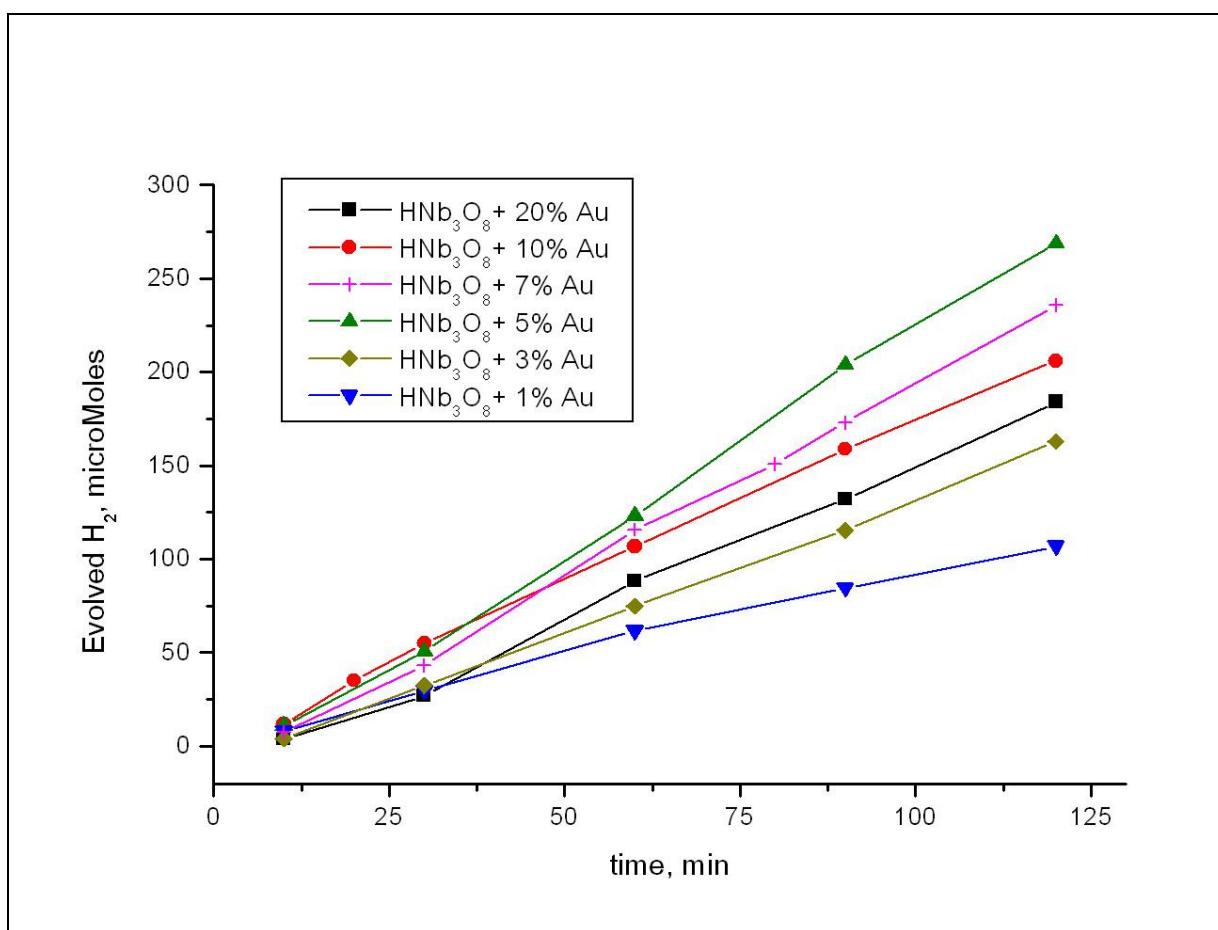


Figure 5.11: Hydrogen evolution at different loading percentage of gold

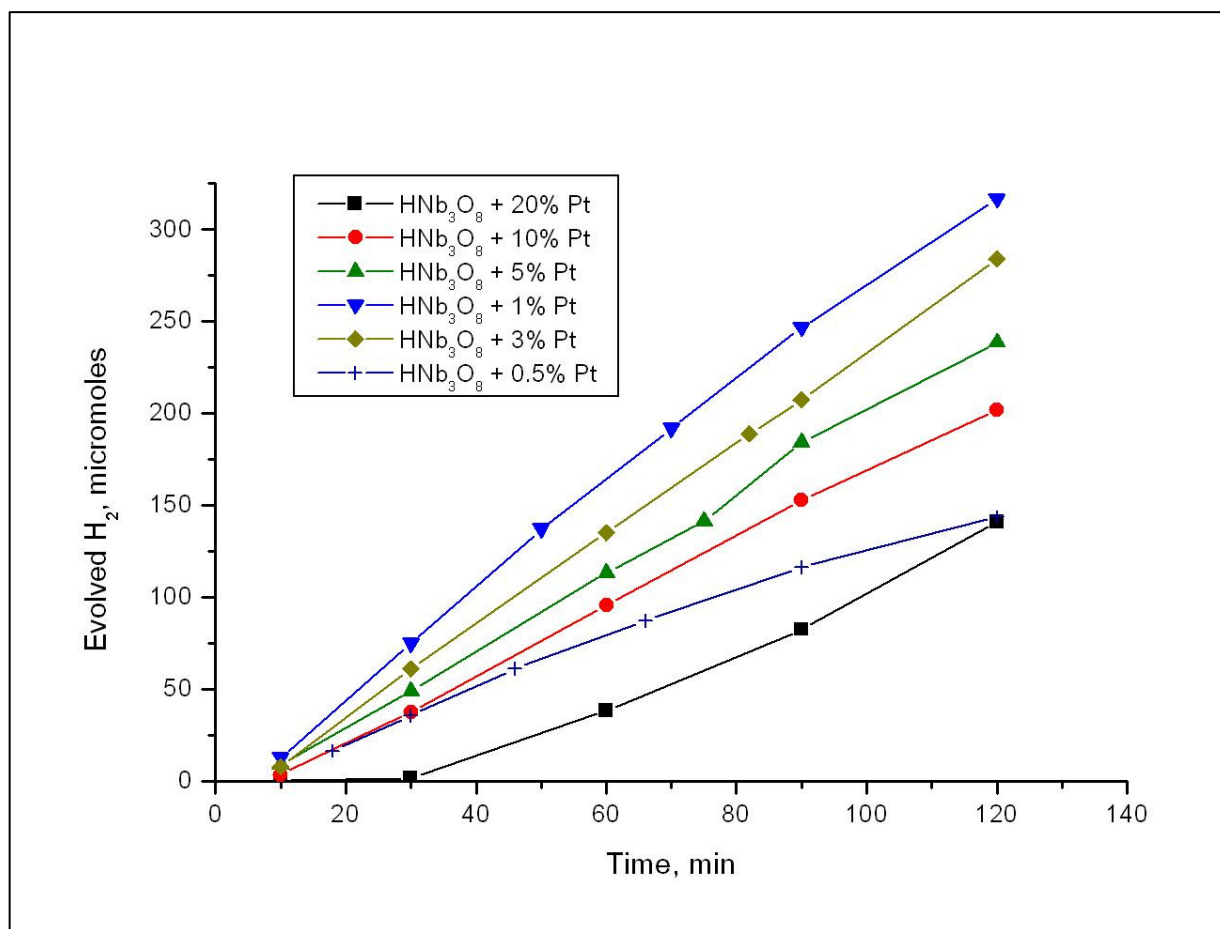


Figure 5.12: Hydrogen evolution at different loading percentage of platinum

A measured volume of 0.75 mL of exfoliated HNb_3O_8 materials was mixed with different percentage of HAuCl_4 and H_2PtCl_6 solution and then 1 mL of EtOH was added to it before UV irradiation. For instance, the procedure to get a 5% Pt loading on HNb_3O_8 materials is as follows: 0.75 mL of exfoliated HNb_3O_8 colloid is mixed with 7.5 mL of 100 ppm H_2PtCl_6 solution, 21.75 mL of HNO_3 (0.2%) and 1.0 mL of EtOH. The density of the colloid is found 0.02 gm/mL.

5% metal (for both Au and Pt) loading was found to be optimum loading for hydrogen evolution under UV light excitation (Figure 5.11 and 5.12). Usually Pt loaded HNb_3O_8 was better than Au loaded HNb_3O_8 for hydrogen evolution; however, at 20% loading condition Au loaded HNb_3O_8 seemed better than Pt loaded HNb_3O_8 , and at 10% loading condition they both appeared similar. A loading condition that is lower than 10% favored more Pt loaded samples than Au loaded samples. Pt loading makes

samples dark grey. So higher Pt loading (i.e., 20%) blocks the UV light from penetrating into the catalyst, which could be a reason for the decrease in activity. Higher Au loading (i.e., 20%) may not block UV light in the same ratio of Pt loading.

5.6 Influence of electron donor concentration on H₂ evolution

The presence of electron donor is needed for photocatalytic hydrogen evolution. Ethanol has been used as a good type of electron donor. It is necessary to optimize the amount of electron donor. Different amount of EtOH (0.5 mL, 1.0 mL, 1.5 mL and 2.0 mL) was used in Pt deposited HNb₃O₈ materials.

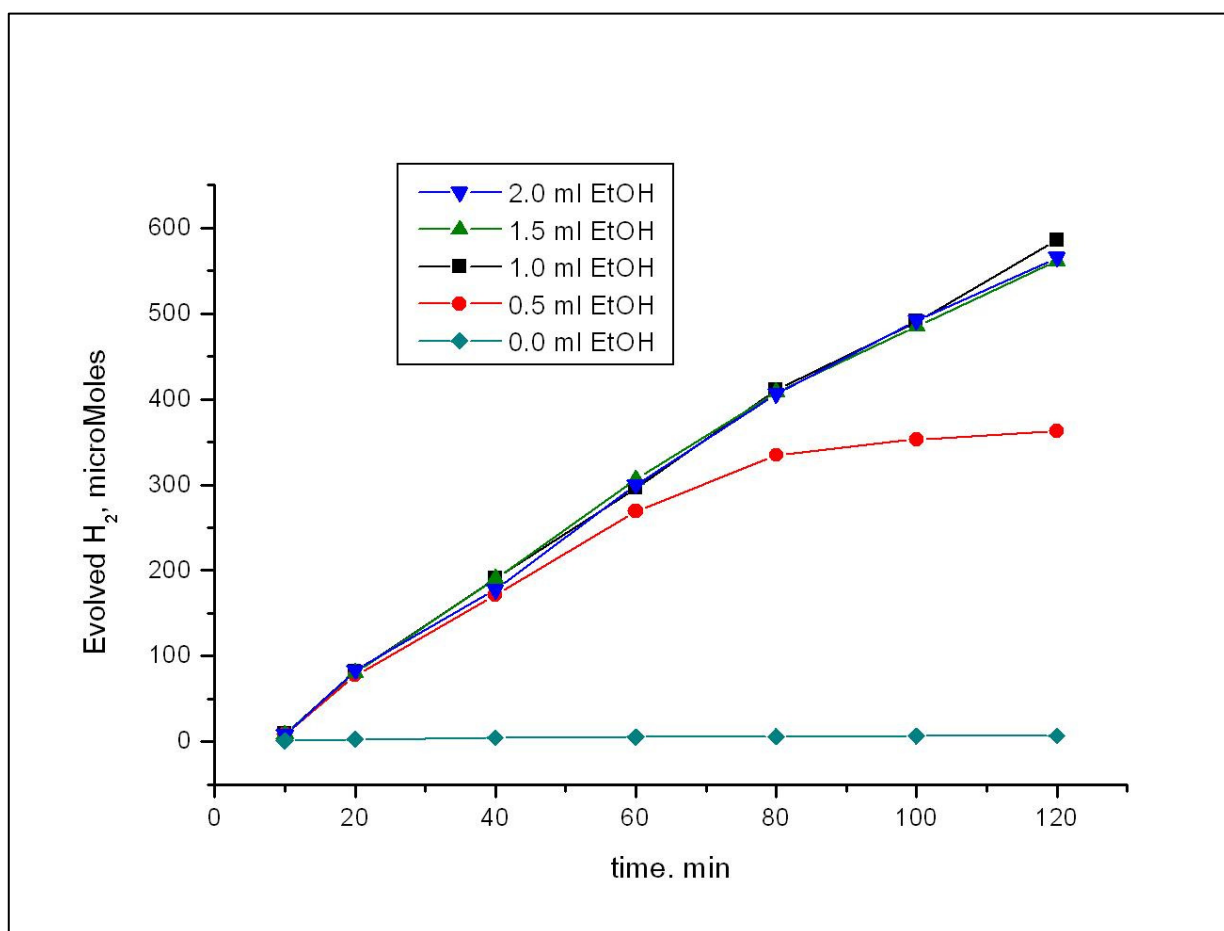


Figure 5.13: Effect of electron donor-EtOH amount in Pt deposited HNb₃O₈-POX system.

The optimum amount of EtOH as an electron donor in Pt deposited HNb₃O₈-POX system was found to be 1.0 mL (Figure 5.13). Additional amount of EtOH did not increase the amount of hydrogen evolution. Without EtOH the amount of hydrogen evolution was negligible.

5.7 Influence of metal deposition method on H₂ evolution

Different metal loading conditions were investigated to optimize the system. 20% metal loading was considered for all the cases. In method 1, exfoliated HNb₃O₈ colloids were precipitated using HAuCl₄ / H₂PtCl₆, rinsed with distilled water and then HAuCl₄ / H₂PtCl₆ and EtOH were added before UV irradiation. In method 2, exfoliated HNb₃O₈ colloids were precipitated using concentrated HCl, rinsed with distilled water and then HAuCl₄ / H₂PtCl₆ and EtOH were added before UV irradiation. Finally in method 3, exfoliated HNb₃O₈ colloids were precipitated using HAuCl₄ / H₂PtCl₆ and then EtOH was added before UV photolysis.

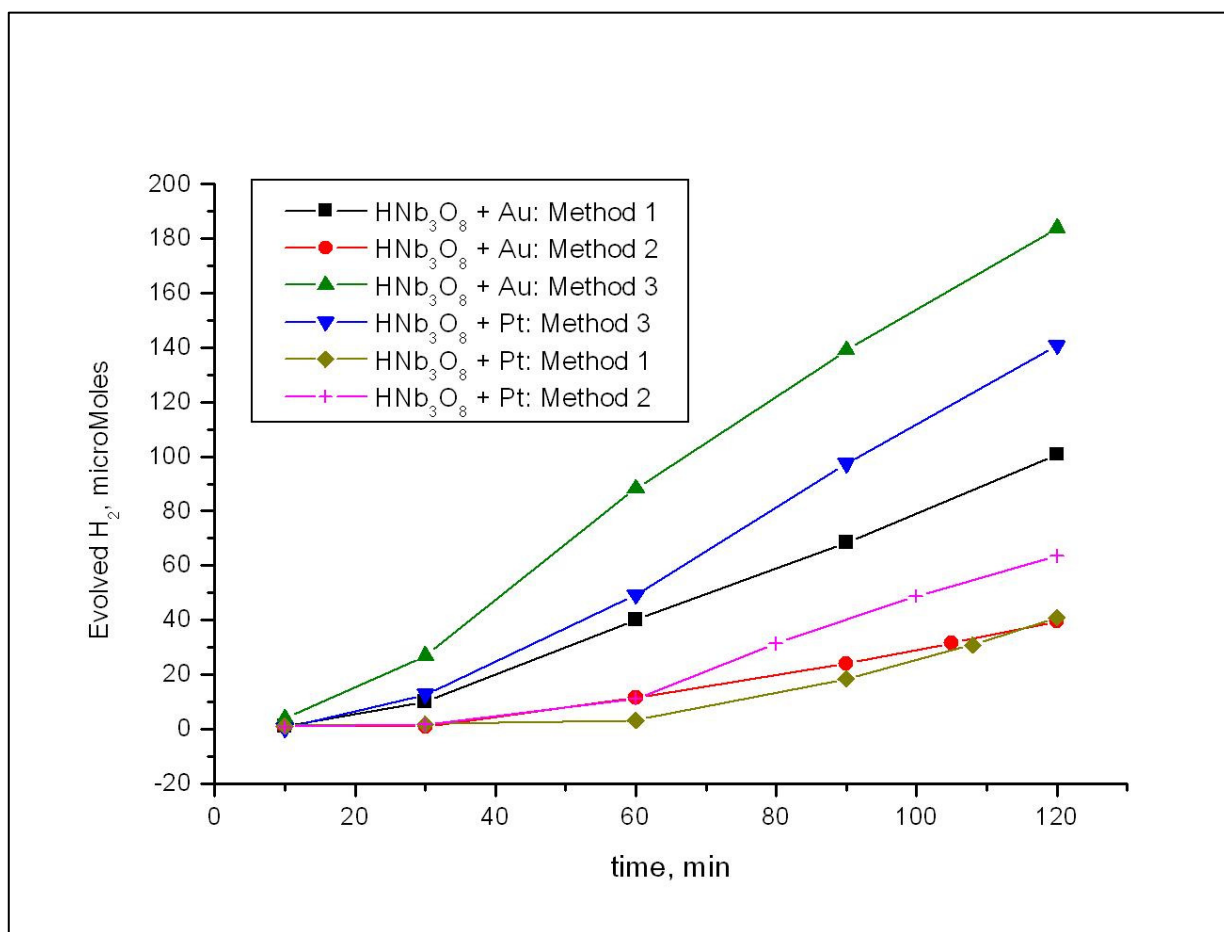


Figure 5.14: Different methods of metal deposition in HNb₃O₈ system.

Method 3 was found to be best for both Pt deposition and Au deposition in the HNb₃O₈ system (Figure 5.14). Au⁺³ or Pt⁺⁴ did not show any interaction without UV light (method 1), and precipitation

with concentrated HCl did not show better Au^{+3} or Pt^{+4} reduction under UV light. However, colloid precipitation with HAuCl_4 / H_2PtCl_6 followed by UV radiation, showed the best photolytic activity. So the result can be explained in this way. When the colloidal HNB_3O_8 sheets get precipitated due to pH drop by HAuCl_4 / H_2PtCl_6 solution, Au^{+3} or Pt^{+4} are trapped or stay in close proximity to the HNB_3O_8 sheets. Once the POX material gets enough UV energy, the electrons reduce the metals effectively and they get deposited on the surfaces of the HNB_3O_8 sheets. These metallic spots act as reactive sites for water photolysis.

5.8 Quantum efficiency of H_2 evolution

Number of photons involved in UV photocatalytic system was measured using a light power meter (PM 100, Thorlabs Inc., Newton, New Jersey, USA) in conjunction with a thermal sensor (S212A-10 W, Thorlabs Inc., Newton, New Jersey, USA). Quantum efficiency of H_2 evolution was then calculated using the following equation:

Apparent quantum yield (AQY),

$$AQY(\%) = \left(\frac{R}{I} \right) \times 100 \quad (1)$$

where R and I represent the initial rate at which H_2 molecules were evolved and the rate at which photons impinge on the sample, respectively.

Number of photons (n),

$$n = \frac{p\lambda}{hc} \quad (2)$$

where p, λ , h, and c are power of photons in watt, wavelength of UV light (254 nm), Plank's constant (6.626×10^{-34} joule.sec) and speed of light (2.99×10^8 m/sec) respectively.

With a power meter reading of 11.98 mW (sensor dia: 1.6 cm) gives 0.127 W for sample height of 8.5 cm which calculates the number of photon of 1.63×10^{17} /sec or 5.86×10^{20} /hr from equation 2. Pt deposited HNB_3O_8 -POX materials produced 296.09 μmoles of hydrogen in one hour. So the Apparent Quantum Yield (AQY) becomes to be 60.84% from equation 1. It is usually assumed that the maximum is $\frac{1}{2}$ H_2 produced per photon striking a sample.³⁴

5.9 Conclusion

In presence of UV light the synthesized photocatalysts, HTiNbO₅-POX and HNb₃O₈-POX showed excellent photocatalytic activity. 60.84% of apparent quantum yield was achieved in hydrogen production. The Au⁺³ and Pt⁺⁴ reduction and deposition pattern showed some insight of the catalyst materials. The optimization of metal deposition, electron donor concentration and method of metal incorporation helped to understand the whole system. These results will be very useful in the process of hydrogen production in presence of visible light.

Chapter six: Hydrogen production under visible light

6.1 Introduction

The main goal for developing porous metal oxide catalysts was to use them in visible light to produce hydrogen by water photolysis, to create a renewable source of energy. When hydrogen is burned in air, it produces energy and water without producing any greenhouse gases to complete the cycle. The wide band gap of the synthesized POX materials made them useful for absorbing UV light and for producing hydrogen by splitting water molecules, as already described in Chapter Five. However visible light has lower energy and it cannot overcome the band gap of POX materials. This necessitates the use of visible light sensitive dye molecules to bring the photo catalyst into the visible light spectrum. This chapter will describe the modification process of POX materials to make them visible light sensitive. The result of hydrogen evolution from the modified POX materials will be presented.

6.2 Experimental setup

Platinum and gold deposited POX materials were used as catalysts for water splitting into hydrogen gas. N3 (B4) dye (Dyesol Australia Pty Ltd, Queanbeyan, New South Wales, Australia) was used as a visible light sensitizer. The chemical name of this compound is *cis*-bis(isothiocyanato)bis(2,2'-bipyridyl-4,4'-dicarboxylato)-ruthenium(II) and the structure is drawn in Figure 6.3. The dye was dissolved in dry ethanol and different concentration of dye was prepared for analysis. A UV-VIS absorption spectrum is shown in Figure 6.4. Different methods of anchoring N3 dye with Pox materials were examined as well as different concentration of dye and electron donor (EtOH) were also tested to optimize the system. A 75W xenon arc lamp (Cat # 27-1031, Ealing Inc., Rocklin, CA, USA) was used as a source of visible light (Figure 6.1) where a plastic filter cut off the UV fraction (Figure 6.5). The light emission spectrum of this kind of lamp is shown in Figure 6.2. Similar to the steps described in chapter five, gas samples were analyzed periodically from the sample tube using gas chromatograph.

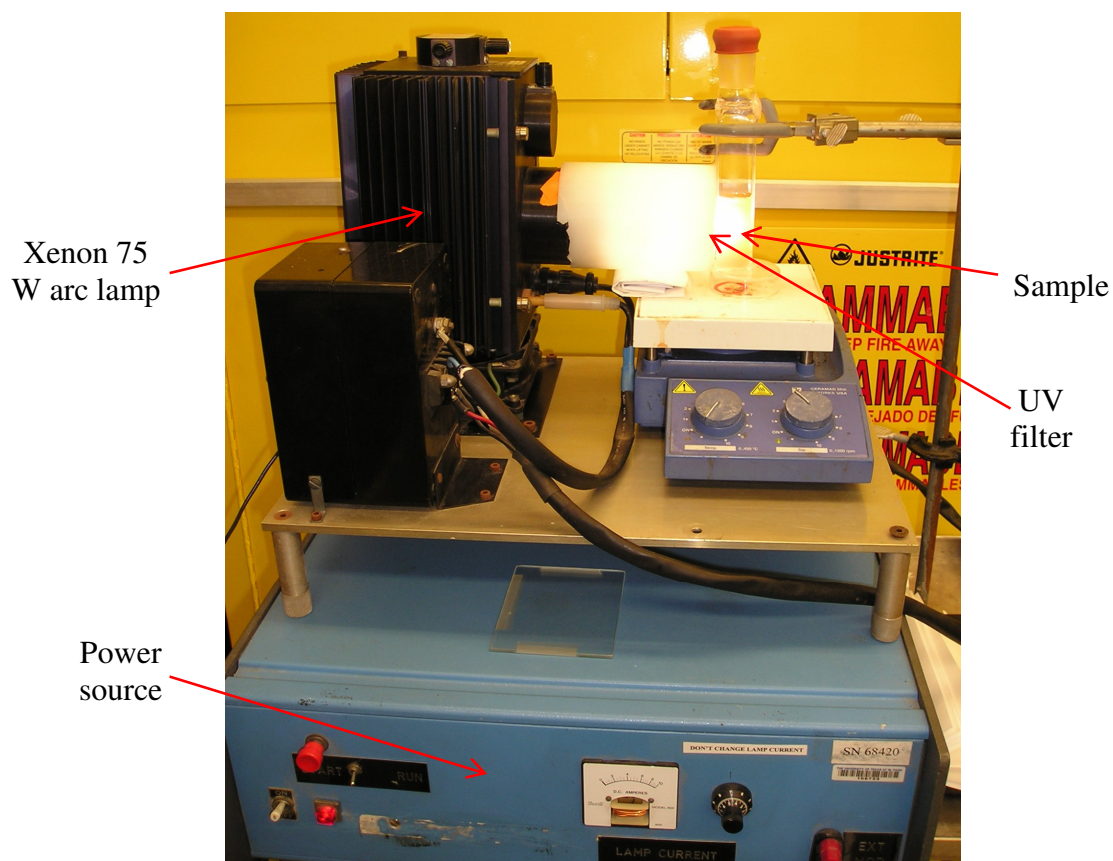


Figure 6.1: Visible light experimental setup

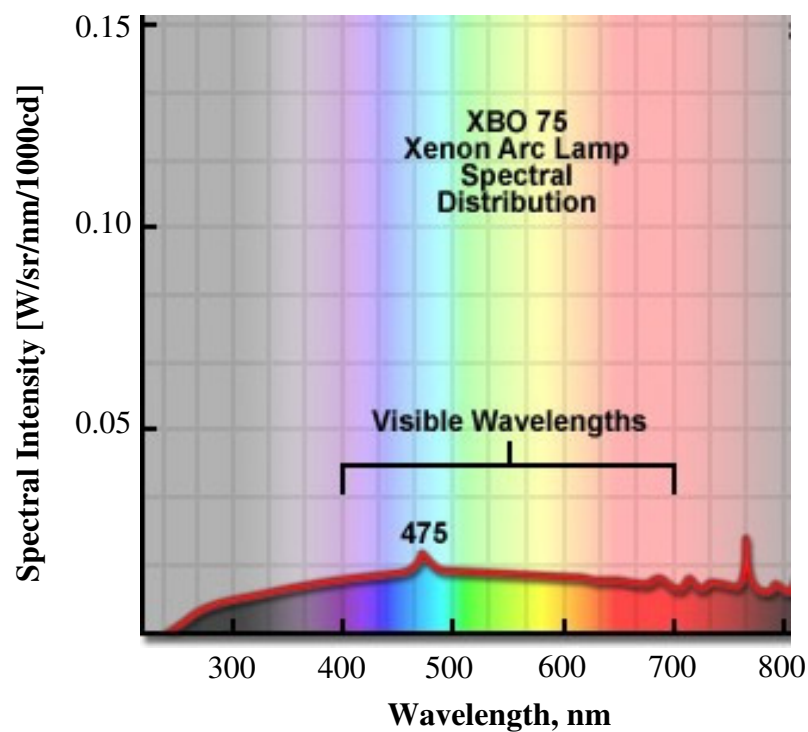


Figure 6.2: Light emission spectrum from 75W xenon arc lamp

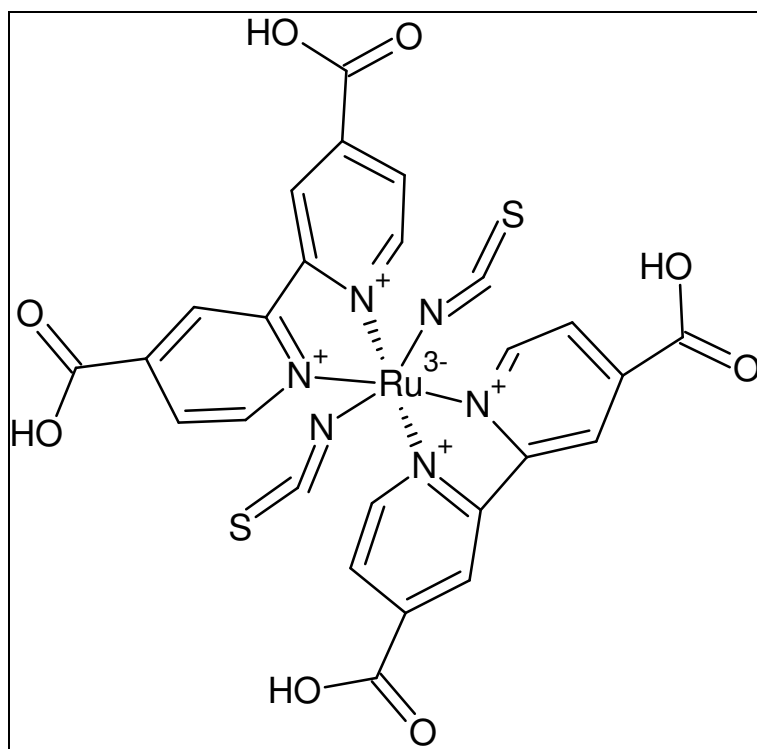


Figure 6.3: Chemical structure of N3 dye

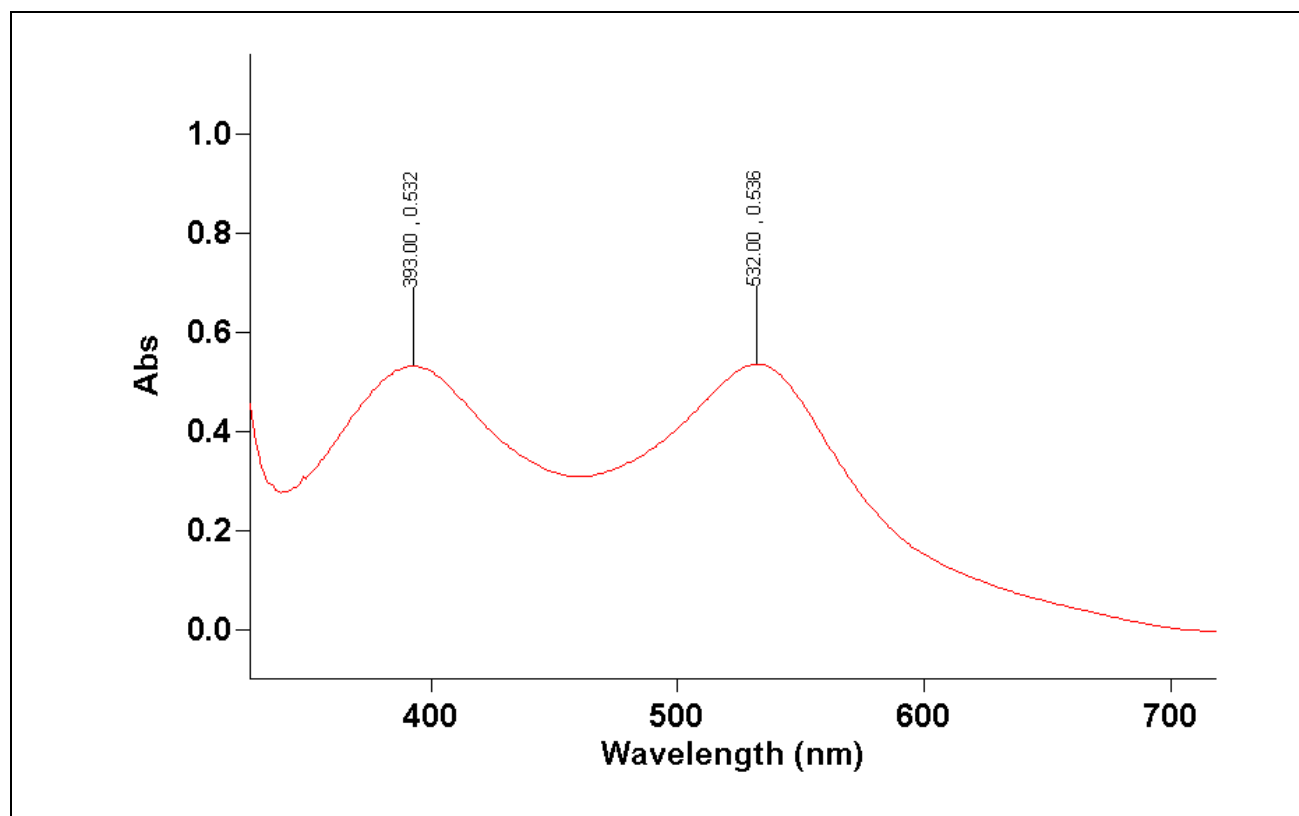


Figure 6.4: Absorption spectrum of N3 dye at 50 μmolar concentration

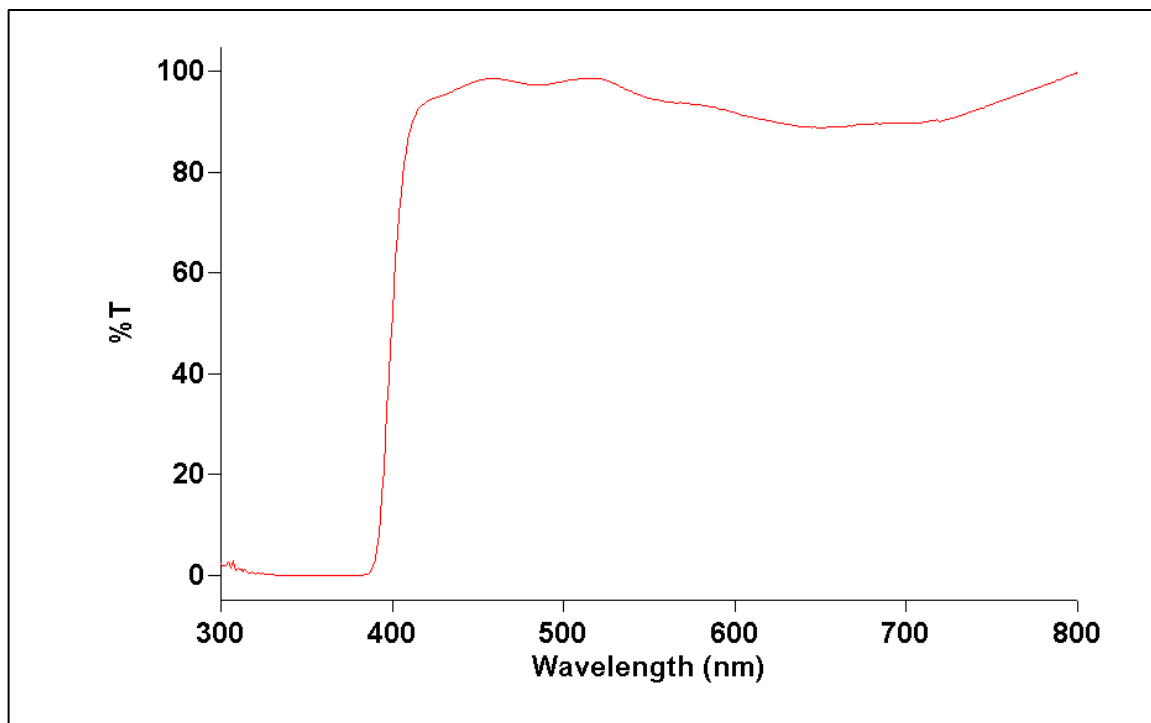


Figure 6.5: Transmission spectrum of plastic filter used to block UV light from xenon arc lamp.

6.3 Hydrogen evolution

0.015 gm of $\text{HTiNbO}_5/\text{HNb}_3\text{O}_8$ -POX materials was used in deposition of Pt and Au metals. The metal loading weight percentage was kept fixed in 5%. After metal loading, the wet sample was centrifuged and rinsed with dry EtOH for four times to make sure that there is no water but EtOH in POX materials. 10 mL of 1 milimolar N3 dye was added and stirred for 15 minutes in dark and then centrifuged and rinsed with water (pH 2) for two times. After centrifuging the sample, the solid part was kept for visible light water photolysis. This solid sample was then taken into a 30 mL pyrex glass reaction tube where 20 mL of water (pH 2) and 1 mL of EtOH was added. The reaction tube opening was closed by rubber septum. After purging the sample with argon gas for 15 minutes to remove the dissolved oxygen and headspace gas, the reaction tube was placed next to the xenon arc lamp using a plastic filter to cut off UV light. The rate of hydrogen evolution was measured by analyzing 0.25 mL of gas at different time intervals. The reaction tube was compensated by adding 0.25 mL of argon gas each

time the sample gas was withdrawn for analysis. The measured value of hydrogen evolution was corrected for the dilution by added argon gas.

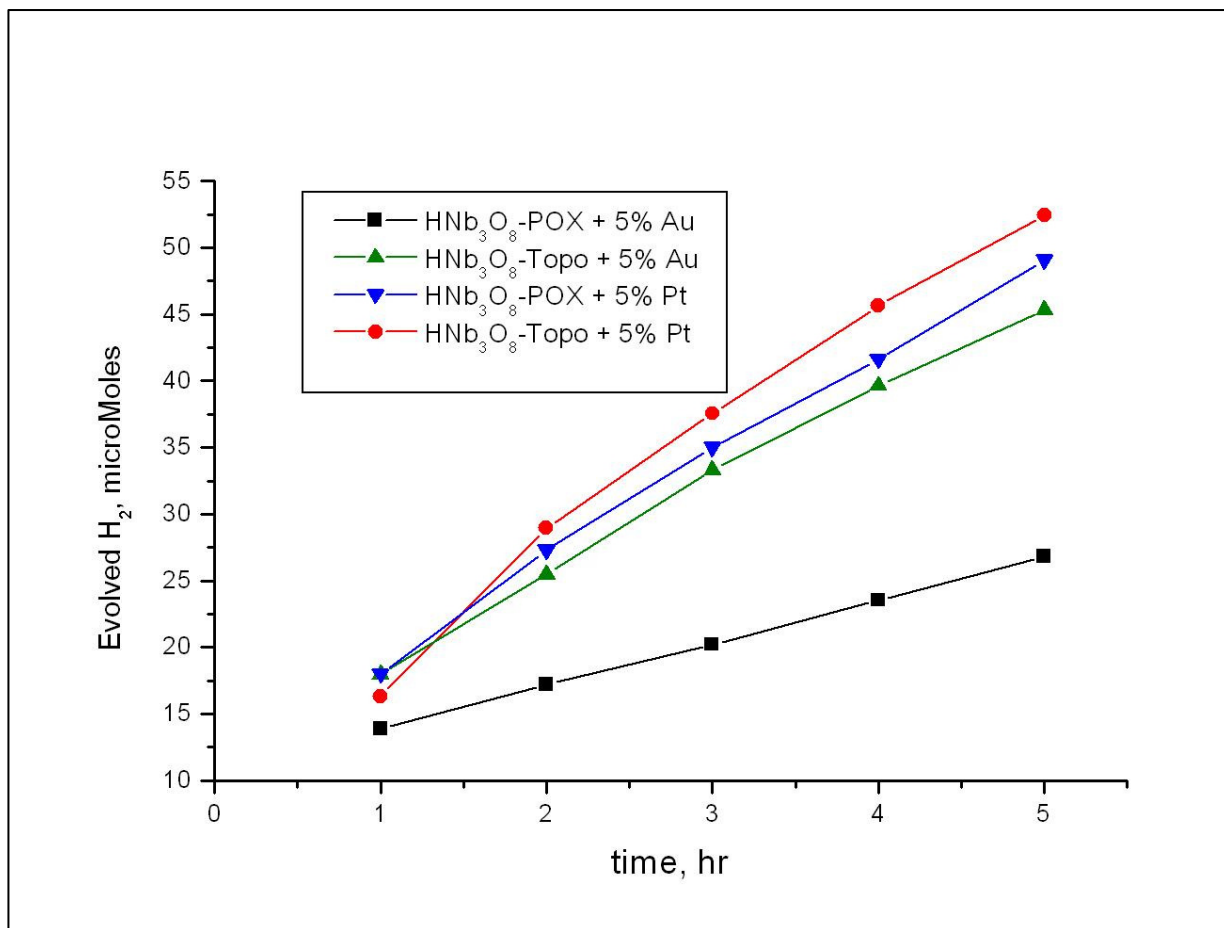


Figure 6.6: Hydrogen evolution in visible light by Au/Pt deposited HNb_3O_8 materials

The Pt deposited POX materials showed better hydrogen production ability than Au deposited POX materials (Figure 6.6 and 6.7). Sometimes Pt deposited samples are two times as good as Au deposited samples. However, HTiNbO_5 samples showed that Au deposited samples are as good as Pt deposited samples when they are topotactic dehydrated (Figure 6.7). Topotactic dehydration of POX materials showed increased hydrogen evolution activity in all cases. So the assumption that was made during materials characterization proved valid, which means that topotactic dehydration increases electronic conduction and so better hydrogen evolution by connecting the sheets covalently in place of original ionic bonds.

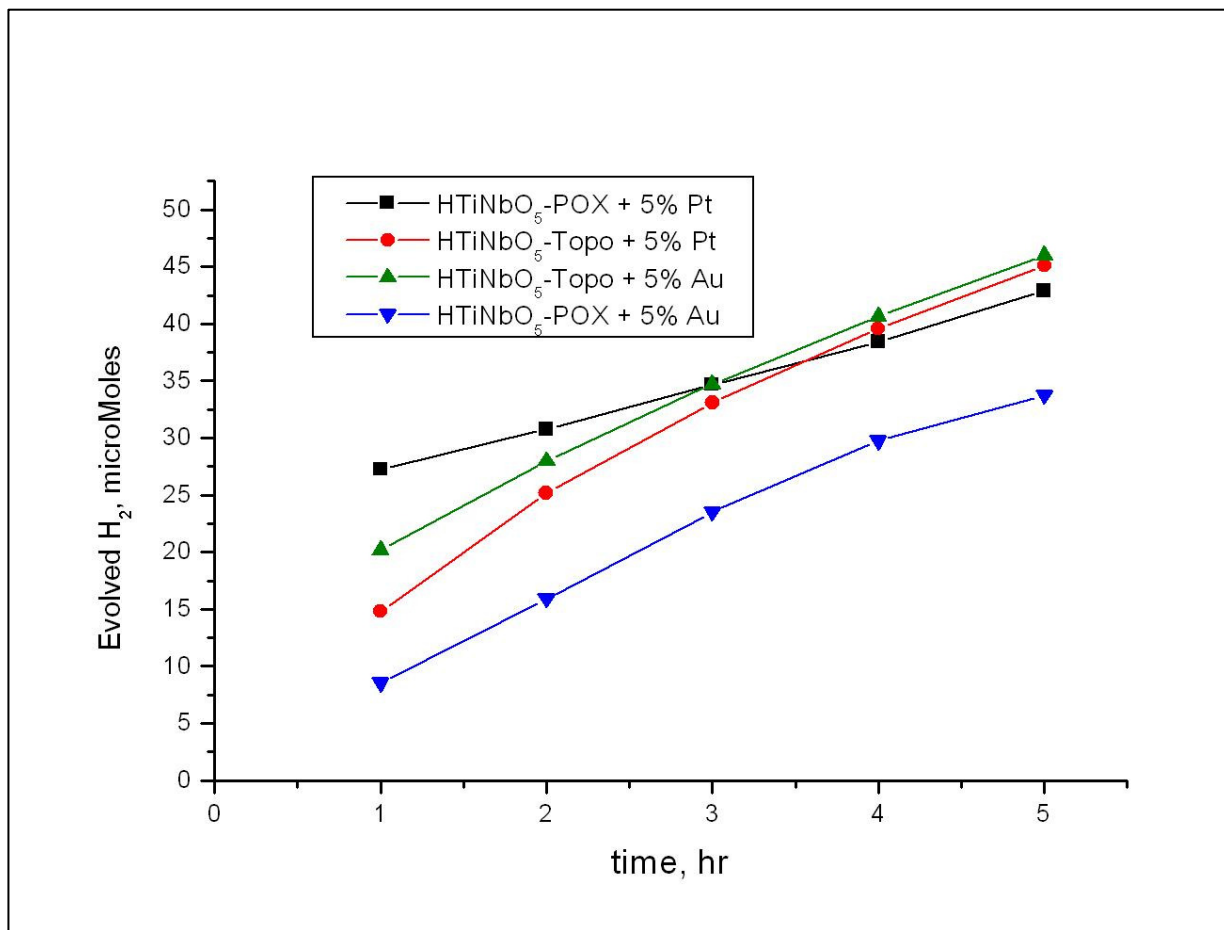


Figure 6.7: Hydrogen evolution in visible light by Au/Pt deposited HTiNbO₅ materials

6.4 Hydrogen evolution at different dye attachment methods

The visible light sensitizer, N3 dye was anchored with POX materials in two different techniques to get the maximum dye usage for most visible light absorption. The first method tried was precipitation method. In this process dye stuff was precipitated onto the POX materials. First the wet metal deposited POX containing residue water was taken to 15 mL centrifuge tube where 10 mL distilled water was added and 2-3 drops of 40% tetrabutylammoniumhydroxide (TBA) was mixed to adjust pH to 8. 1.4 mL of 1 mM N3 dye was mixed and then 2 drops of concentrated HCl was added to drop pH to 1~2. The sample was centrifuged and wet N3 dye precipitated POX materials were taken to the 30 mL pyrex reaction tube. Then 20 mL of water (pH 2) and 1 mL of dye EtOH was added to the tube. Before starting photolysis, the sample mixture was purged with Ar gas to remove any dissolved gas and headspace gas

in the reaction tube. The amount of 1.0 mL 1.0 mM dye was calculated by measuring the amount of dye needed to cover completely the POX materials surface where the surface area of POX materials and one N3 dye molecule were considered as $110 \text{ m}^2/\text{gm}$ and $1.96 \times 10^{-18} \text{ m}^2/\text{molecule}$ respectively.

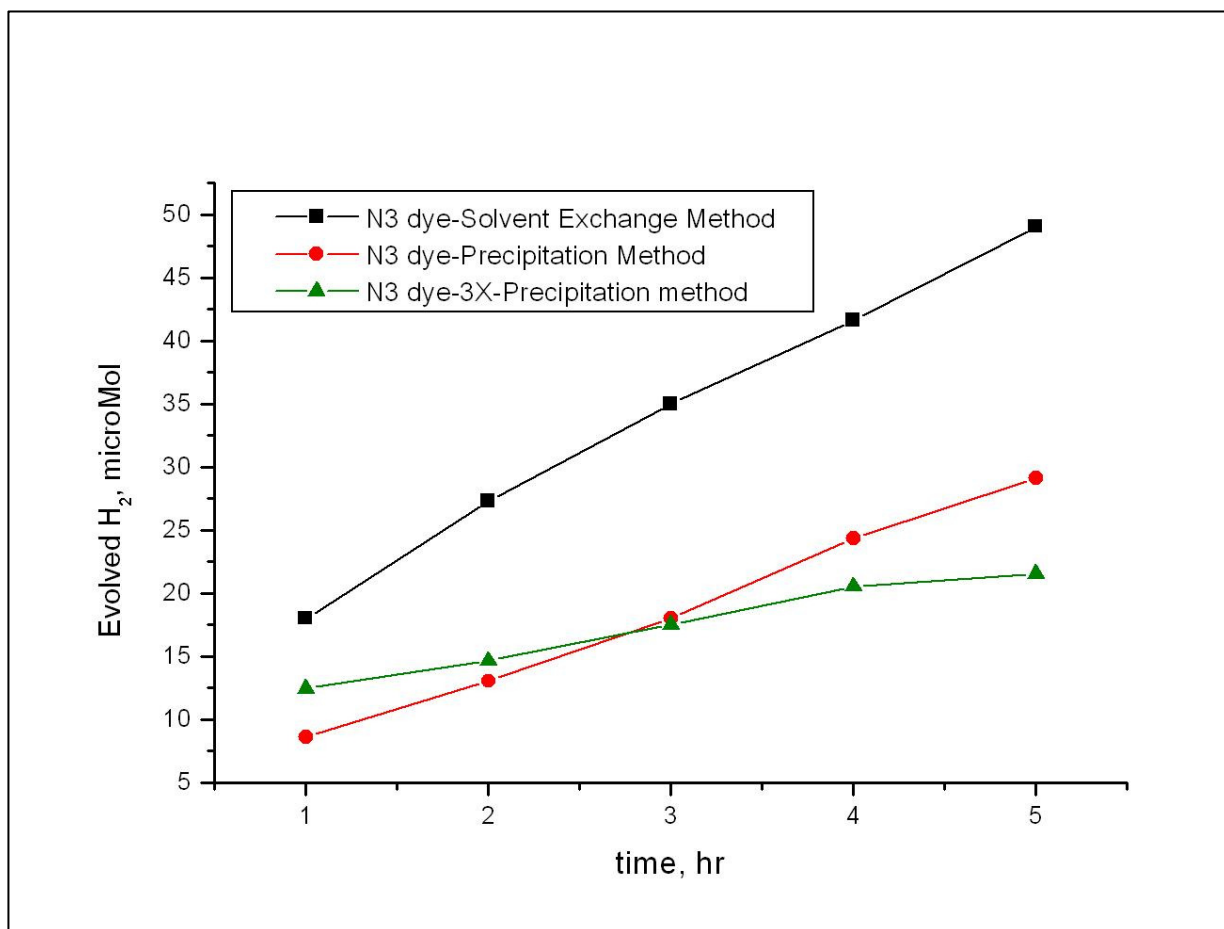


Figure 6.8: Hydrogen evolution at different dye attachment methods in 5% Pt loaded HNb_3O_8 POX

The second method was named as solvent exchange method as in this process wet metal deposited POX materials were solvent exchanged with dry ethanol. First wet metal deposited POX containing residue water rinsed and centrifuged with 25 mL dry ethanol for four times. 10 mL of 1.0 mM N3 dye was then added to it and the mixture was shaken for 20 minutes in dark. The sample was then centrifuged and rinsed with water (pH 2) for two times. Finally, the sample was taken to the reaction tube, 20 mL of water (pH 2), 1 mL of dry ethanol was added, and purged with argon gas.

Figure 6.8 shows that solvent exchange method had better catalytic activity in terms of the amount of hydrogen evolution than the precipitation method. So it is clear that the solvent exchange method makes it easier for N3 dye to attach to the POX materials surface. Since N3 dye solutions are made in dry ethanol solvent, the solvent exchange method with no water presence but ethanol, gives better anchoring ability of dye molecules than its counterpart, the precipitation method where residue water exists. A three times higher amount of dye that is needed to cover completely the POX materials surface, could not show any increase in hydrogen evolution rate.

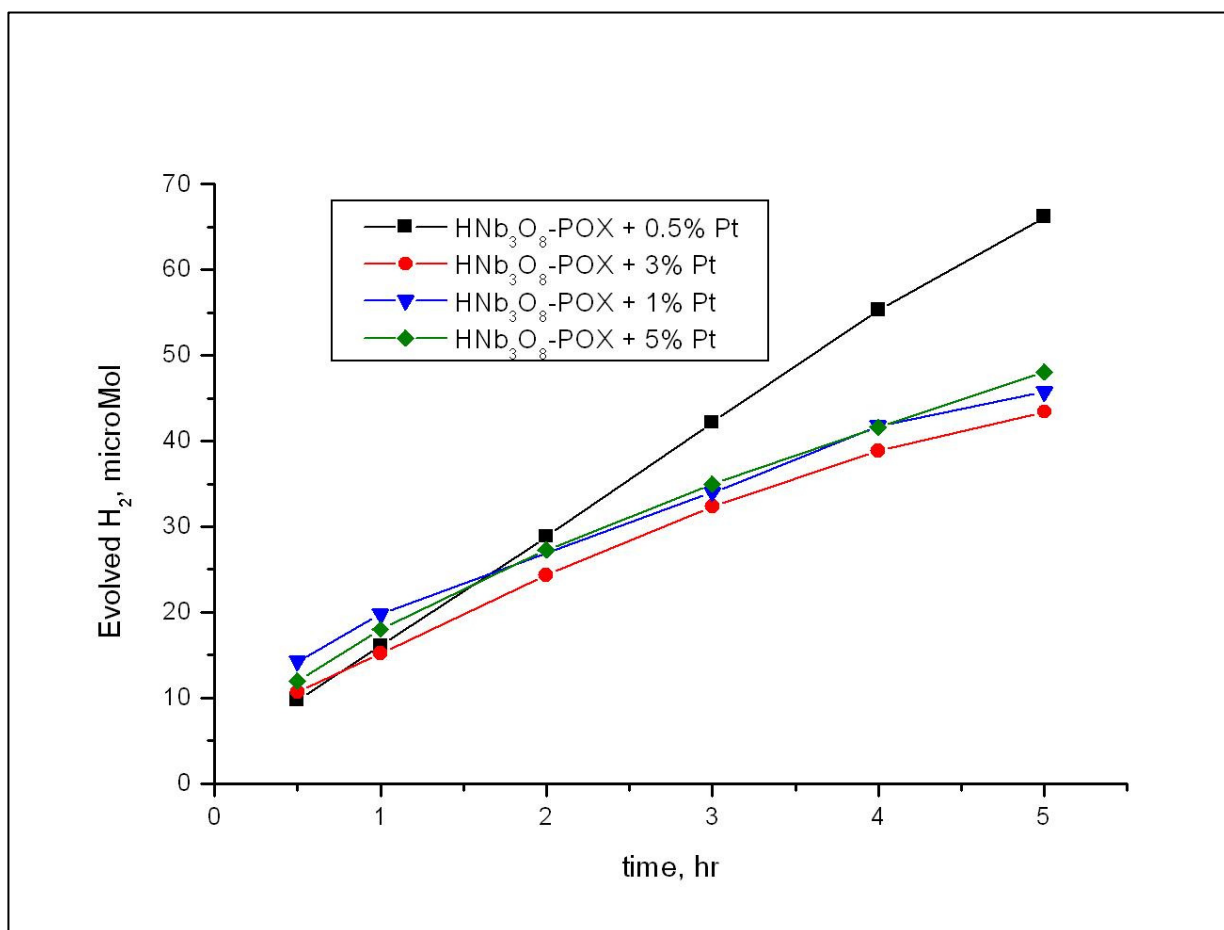


Figure 6.9: Hydrogen evolution in HNb₃O₈ POX materials at different Pt loading

6.5 Dependence of metal loading on hydrogen evolution

The effect of metal loading percentage on the hydrogen evolution rate was examined. Both Pt and Au metals were used for this analysis. N3 dye molecules were attached to metal deposited POX

materials by solvent exchange method and then rinsed twice with water (pH 2). As mentioned above 20 mL of water (pH 2) and 1 mL of dry ethanol was added to the sample and then Ar gas was purged through it.

Figure 6.9 shows that 0.5% Pt loaded HNb_3O_8 POX materials has higher hydrogen evolution ability than other Pt loaded HNb_3O_8 POX materials and Figure 6.10 shows that 3% Au loaded HNb_3O_8 POX materials have higher hydrogen evolution ability than other Au loaded HNb_3O_8 POX materials.

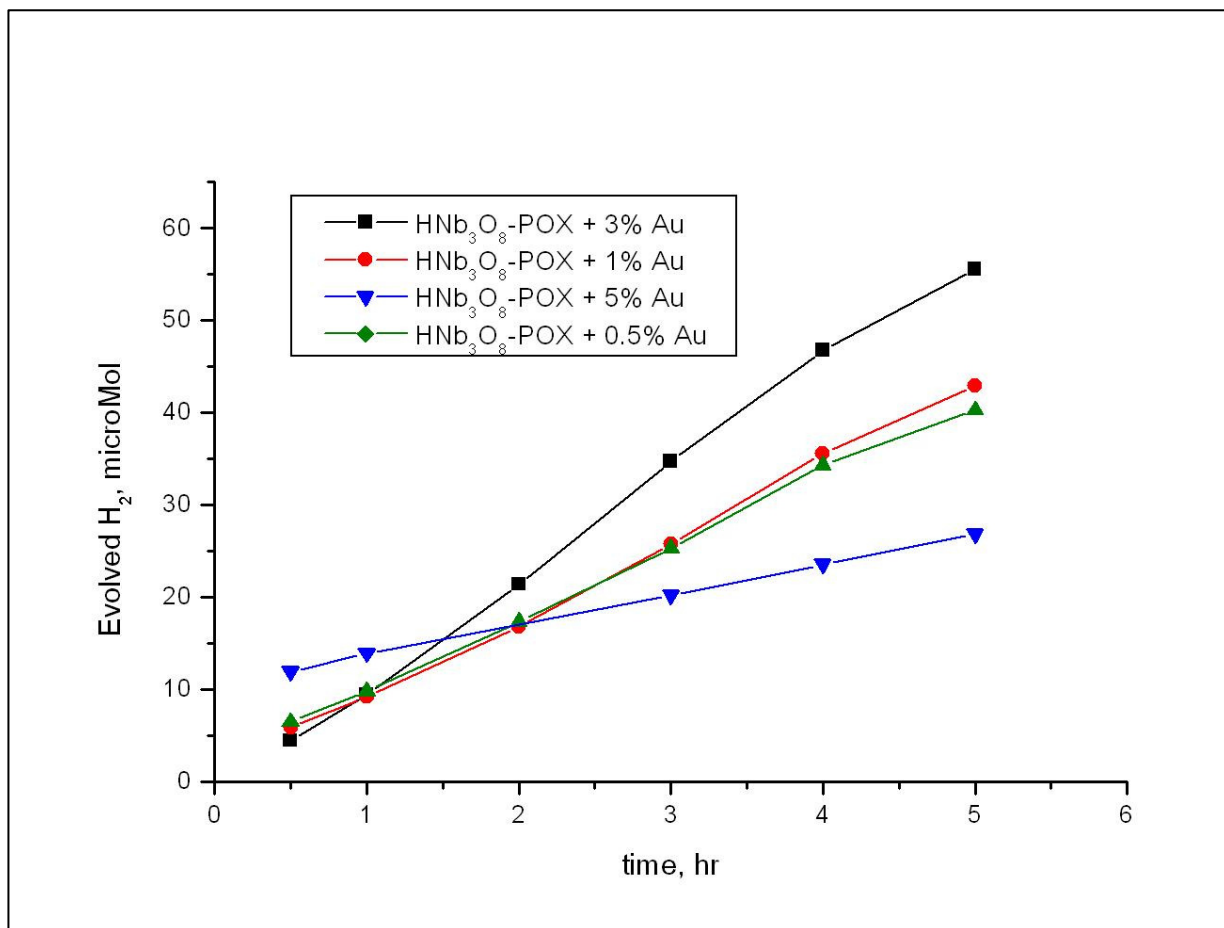


Figure 6.10: Hydrogen evolution in HNb_3O_8 POX materials at different Au loading

6.6 Dependence of dye loading on hydrogen evolution

Since N3 dye is a visible light sensitizer, it has great influence on hydrogen evolution. Different concentration of dye was used to get the optimum dye concentration for maximum hydrogen evolution. First the amount of dye needed to cover completely the POX materials surface was calculated and then

for a working volume of 10 mL the concentration was measured. 0.14 mL of 1 mM dye was the necessary amount for complete coverage of POX surface where it was considered that POX and dye molecules had surface area of $110 \text{ m}^2/\text{gm}$ and $1.96 \times 10^{-18} \text{ m}^2/\text{molecule}$ respectively. A ten times higher concentration was used to get a better concentration gradient which led to 1.4 mL of 1 mM dye. Other dye concentrations considered were 1.4 mL of 0.50, 0.75 and 1.50 mM.

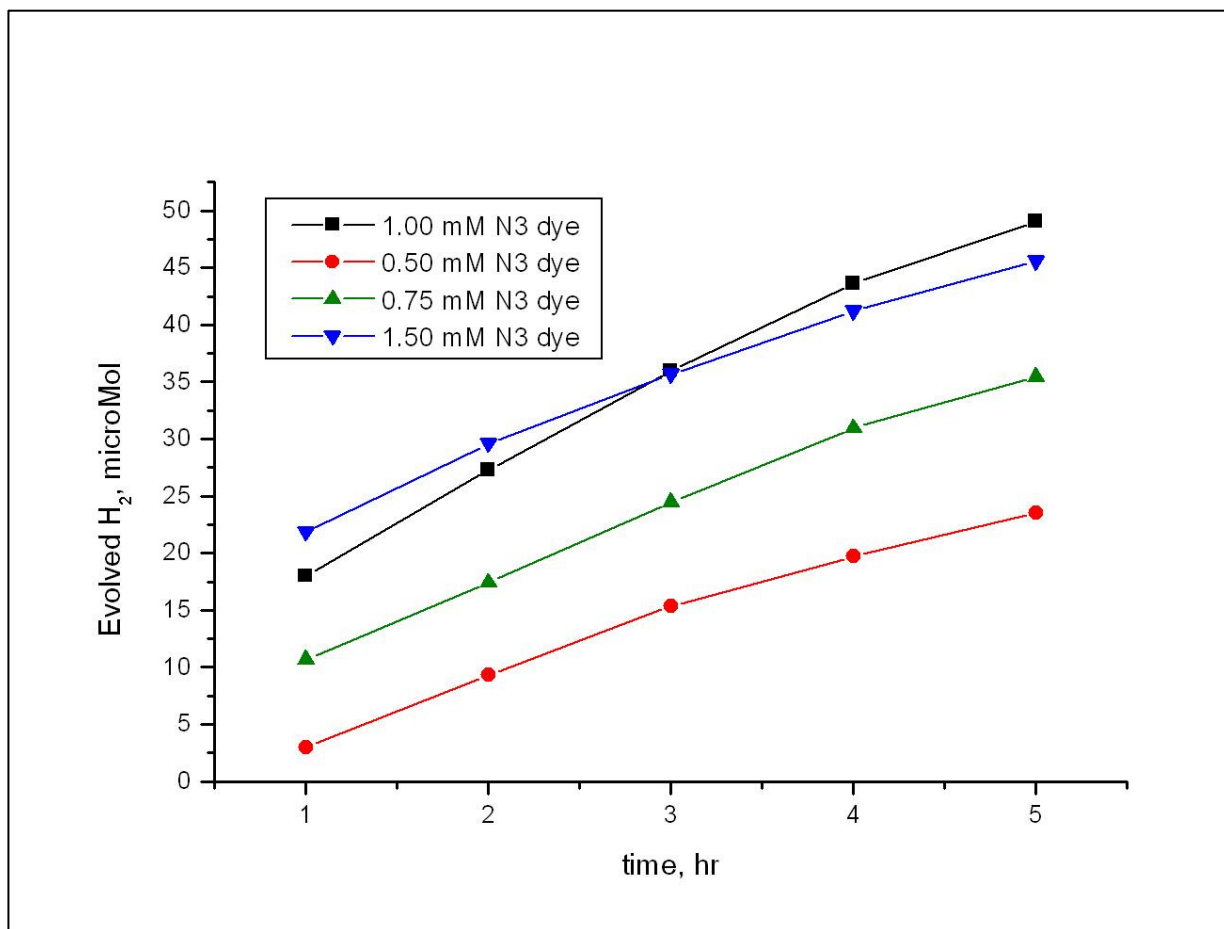


Figure 6.11: Hydrogen evolution in 5% Pt loaded HNb_3O_8 POX at different dye concentrations

6.7 Dependence of electron donor on hydrogen evolution

The electron donor provides a continuous supply of electrons to the POX materials for uninterrupted photocatalytic activity. So it is necessary to optimize the amount of electron donor necessary for the system. Dry ethyl alcohol (EtOH) was used as an electron donor throughout the

research. Figure 6.12 shows that 1 mL of EtOH was optimum for the current visible light experimental condition.

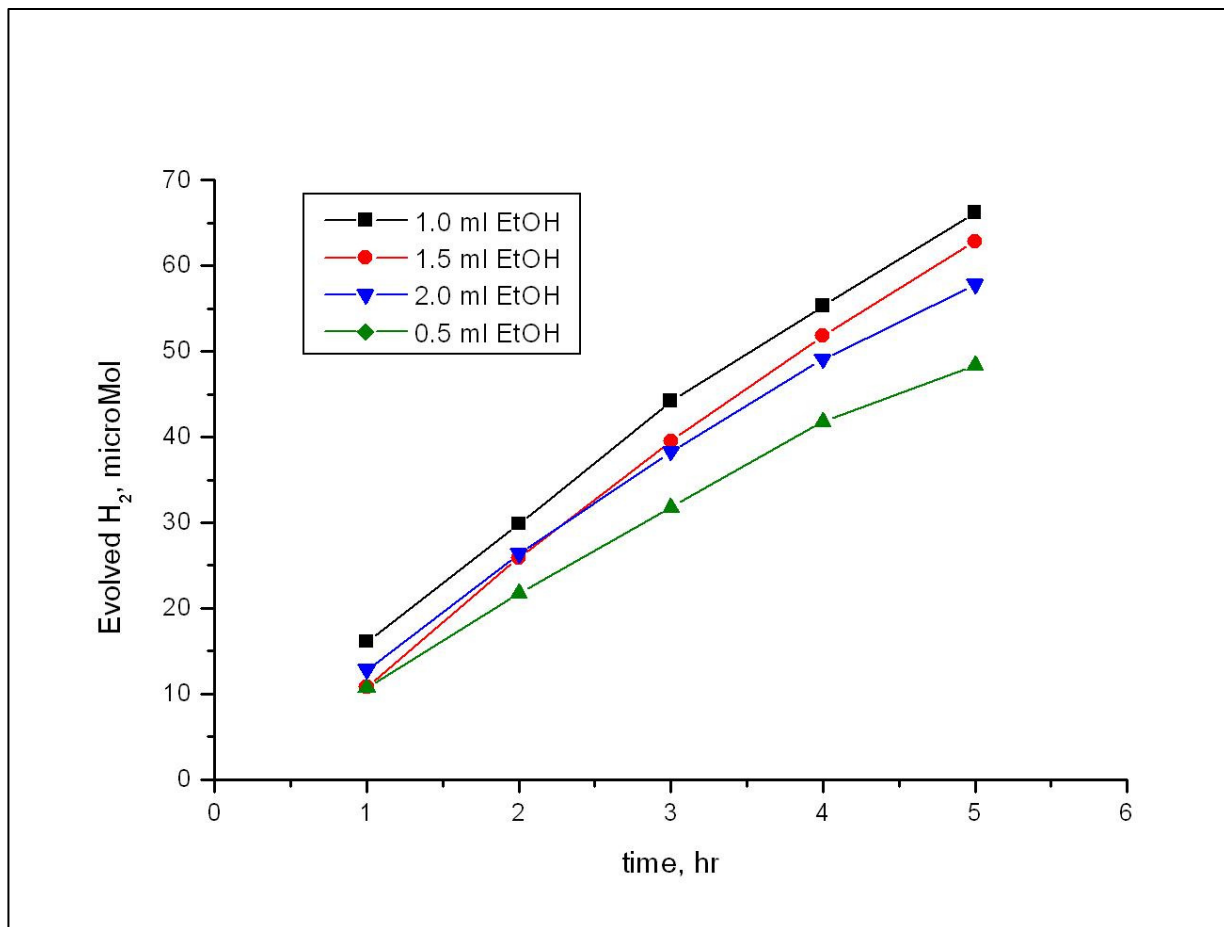


Figure 6.12: Hydrogen evolution in 0.5% Pt loaded HNb₃O₈ POX at different amount of EtOH

6.8 Quantum efficiency of hydrogen evolution

Number of photons involved in visible light photocatalytic system was measured using a light power meter (PM 100, Thorlabs Inc., Newton, New Jersey, USA) in conjunction with a thermal sensor (S212A-10 W, Thorlabs Inc., Newton, New Jersey, USA). Quantum efficiency of H₂ evolution was then calculated using the following equation:

Apparent quantum yield (AQY),

$$AQY(\%) = \left(\frac{R}{I} \right) \times 100 \quad (1)$$

where R and I represent the initial rate at which H₂ molecules were evolved and the rate at which photons impinge on the sample, respectively.

Number of photons (n),

$$n = \frac{p\lambda}{hc} \quad (2)$$

where p, λ , h, and c are power of photons in watt, wavelength of light (500 nm), Plank's constant (6.626x10⁻³⁴ joule.sec) and speed of light (2.99x10⁸ m/sec) respectively.

With a power meter reading of 4.25 mW calculates the number of photon of 1.07x10¹⁶/sec or 3.86x10¹⁹/hr from equation 2. 1 % Pt deposited HNb₃O₈-POX materials produced 19.76 μ M of hydrogen in one hour. So the apparent quantum yield (AQY) of hydrogen production became to 61.66% from equation 1 on the above. It is usually assumed that a maximum of ½ H₂ is produced per photon striking a sample.³⁴ 61.66% is the maximum AQY obtained considering initial rate of hydrogen evolution.

Table 6.1: Summary of quantum yields in visible light H₂ evolution.

Materials	Loaded Metal	% QY
HNb ₃ O ₈ -POX	5% Pt	30
HNb ₃ O ₈ -POX	5% Au	16
HNb ₃ O ₈ -Topo	5% Pt	32
HNb ₃ O ₈ -Topo	5% Au	28
HTiNbO ₅ -POX	5% Pt	26
HTiNbO ₅ -POX	5% Au	20
HTiNbO ₅ -Topo	5% Pt	28
HTiNbO ₅ -Topo	5% Au	27

However, based on average rate of hydrogen evolution instead of initial rate of hydrogen evolution, the maximum apparent quantum yield was found 44% for HNb_3O_8 -POX with 0.5% Pt loading. The Table 6.1 shows a comparison of different POX materials with their ability to hydrogen evolution.

6.9 Conclusion

The POX materials showed excellent catalytic activity in presence of visible light. Different type of methods were tried to get maximum incorporation of visible light sensitizer dye molecules. Pt and Au metals at various loading percentage helped measure the optimum metal loading condition. HNb_3O_8 -POX materials demonstrated better activity than HTiNbO_5 -POX materials and topotactic dehydrated materials confirmed enhanced reactivity than the normal POX materials. The Apparent Quantum Yield for the hydrogen production (AQY) was calculated to 61.66% which means that the synthesized catalysts have very promising aspect if it can be used in large scale with optimistic economical measures.

Chapter seven: Concluding remarks

7.1 Introduction

World energy consumption is ever increasing as time goes by. Since this energy is mostly coming from fossil fuels which are nonrenewable and responsible for green house gas emissions, there is a great need for developing new, renewable and environment friendly sources of energy. Solar energy has the potential to break water molecules into hydrogen and oxygen at right catalytic condition and this hydrogen gas as is known very flammable gas gives energy and water when burnt in air. So a complete renewable cycle is formed. But developing a suitable catalyst is the toughest job to make the process energy efficient, cost effective and handy to the society. This dissertation research was devoted to develop a catalyst that would enable visible light water splitting to generate hydrogen as a source of renewable energy directly useful for the major energy demand of the society.

7.2 Overall discussion

Since the discovery of photoelectrochemical water splitting by Fujishima and Honda 1972, there has been a lot of effort by scientists to make the result useful. The quantum efficiency of hydrogen production increased from 0.10 to 0.30 in these 38 years but still it is not in so called shape to be produced in global scale as a demand for the mankind. The prime responsible factor for low quantum efficiency is recombination of electrons and holes that are produced by sticking energetic photons on semiconducting materials. Material impurity, confined electronic transportation and slower reaction kinetics lead to this recombination process. In the development process of new porous metal oxide (POX) catalysts, succeeding over these restraining factors was in consideration.

Both of the synthesized POX materials, HTiNbO_5 and HNb_3O_8 , had shown high surface area, nano porous structure with high thermal integrity and wide band gap semiconducting nature. BET surface area analysis showed that the surface area of HTiNbO_5 -POX materials has a surface area of 140

m^2/g from a variety of pore size distribution which would be capable of working enormously if it could be used efficiently. The topotactic dehydration was done at $450\text{ }^\circ\text{C}$ for two hours. The material purity was confirmed with elemental analyses that showed that a trace amount of N and C was present in the sample. UV-VIS-NIR reflectance spectrum helped to quantify the band structure of POX materials and HNb_3O_8 and HTiNbO_5 had band gap of 3.10 eV and 3.07 eV respectively.

In UV light the POX materials exhibited spectacular result in terms of hydrogen evolution. HNb_3O_8 materials superseded HTiNbO_5 materials by a factor of two. The topotactic dehydration made both type of POX materials 50% better than the regular POX materials. In visible light HNb_3O_8 materials was slightly (10%) better than the HTiNbO_5 materials but topotactic dehydrated materials were better than the regular materials sometimes as high as two times. In topotactic dehydration, the POX materials loss water molecules making metal oxide sheets connected through covalent bonds which in turn lead to more electronic conduction throughout the metal oxide sheets and less recombination of electrons and photons and better productivity of hydrogen evolution. The apparent quantum yield of hydrogen production in visible light was achieved to 61.66% which made the synthesized materials very much useful for renewable energy production.

7.3 Experimental limitations

The synthesized materials exhibited high surface area like $140\text{ m}^2/\text{g}$ which means there is a lot of room for surface catalysis. However during the metal deposition step under UV light radiation, the magnetic stirring or during the centrifuge action at high rpm (i.e., 3000), the surface morphology might have been destroyed a little bit leading to a lower surface area of the catalyst in visible light photolysis although there could not be any BET analysis done after doing visible light experiment to conclude the analogy.

The visible light sensitizer dye, N3 has two absorption peaks: one at 380-420 nm and other at 500-540 nm while the UV light blocking filter cuts off light at 400 nm that means part of light

absorption spectrum of N3 dye could not be used. So if there is any tailoring work on N3 dye could shift the absorption spectrum a little towards visible region, then the complete utilization of light absorption by dye molecules would be possible and eventually would increase the quantum efficiency of hydrogen production. Practically on the earth's surface, the solar light does not cut off at exact 400 nm, a smaller fraction of UV closer to the visible region is always possible which will suitably fit the existing N3 dye in the water photolysis system.

The source of visible light used in this research was 75W arc lamp made by Ealing Inc, USA which is kind of old although working perfectly, however a newer and more powerful one could give a better result in terms of quantum efficiency.

7.4 Future work

There were some UV light water photolysis experiments done on exfoliated wet HNb_3O_8 materials that showed better catalytic activity over POX- HNb_3O_8 materials. A complete set of experiments done with exfoliated wet HNb_3O_8 and HTiNbO_5 materials would give better scope for total comparison between HNb_3O_8 and HTiNbO_5 materials in both POX and exfoliated conditions. However, the only limitation of working with exfoliated wet samples is that there is no way of doing topotactic dehydration of exfoliated wet HNb_3O_8 or HTiNbO_5 materials that was proved a successful way of getting better electronic conduction in this research.

The amount of POX materials used in all experiments was kept constant at 0.5 g/L of working volume. Lowering or increasing the material mass could give different result which might be a point of interest for future research. Similar interest of further work could be use of different visible light sensitizer dye because N3 was the only dye used in this research. A different dye might fit better in the visible light spectra with the developed POX materials.

A very important work of any project work is its economic analysis, breakdown of all costs and profits or ways of making it economically viable. However in this research work it was not possible of

doing certain kind of analysis to get a clear picture of economic feasibility. Although it was a sort of fundamental research, at least a thorough economic analysis would make this research work more realistic.

7.5 Conclusion

The current fossil fuel based, nonrenewable energy consumption trend needs to be changed for a sustainable world for generations to come. Wind power, solar power, hydropower or biofuel based renewable power consumption will positively change the way of living today and make the world more peaceful and friendlier than ever. The developed metal oxide photocatalysts, HNb_3O_8 and HTiNbO_5 materials would play an immense role in fundamental research and in the development process of efficient solar power conversion techniques for daily energy demand.

References

1. The outlook for energy: A view to 2030, ExxonMobil Corporation, Irving, TX, 2009.
2. Elizabeth Doris, Joyce McLaren, Victoria Healey, and Stephen Hockett, State of the States 2009: Renewable Energy Development and the Role of Policy, Technical Report, NREL, Golden, CO, 2009.
3. Andrew Mills, Stephen Le Hunte, An overview of semiconductor photocatalysis, *Journal of Photochemistry and Photobiology A: Chemistry* 108 (1997) 1-35.
4. David R. Lide, *Handbook of Chemistry and Physics*, 71st edition, CRC Press, USA.
5. A. Fujishima and K. Honda, Electrochemical Photolysis of water at a semiconductor electrode, *Nature* Vol. 238 July 2 1972.
6. B. O'Regan and M. Grätzel, A low-cost, high-efficiency solar cell based on dye-sensitized colloidal TiO₂ films, *Nature* Vol. 353 October 24 1991.
7. S. Uchida, M. Tomiha, H. Takizawa, M. Kawayara, Flexible dye-sensitized solar cells by 28 GHz microwave irradiation, *Journal of Photochemistry and Photobiology A: Chemistry*, 164 (2004) 93-96.
8. J.-J. Lagref, M.K. Nazeeruddin, M. Gratzel, Molecular engineering on semiconductor surfaces: design, synthesis, and application of new efficient amphiphilic ruthenium photosensitizers for nanocrystalline TiO₂ solar cells, *Inorganica Chimica Acta*, 361 (2008) 735-745.
9. Islam, F.A. Chowdhury, Y. Chiba, R. Komiya, N. Fuke, N. Ikeda, K. Nozaki, L. Han, Synthesis and Characterization of New Efficient Tricarboxyterpyridyl (β -diketonato) Ruthenium(II) Sensitizers and Their Applications in Dye-Sensitized Solar Cells, *Chem. Mater.* 2006, 18, 5178-5185.
10. M.K. Nazeeruddin, R. Humphry-Baker, P. Liska, M. Graetzel, Investigation of Sensitizer Adsorption and the Influence of Protons on Current and Voltage of a Dye-Sensitized Nanocrystalline TiO₂ Solar Cell, *J. Phy. Chem. B* 2003, 107, 8981-8987.

11. C. Klein, M.K. Nazeeruddin, P. Liska, D. Di Censo, N. Hirata, E. Palomares, J.R. Durrant, M. Gratzel, Engineering of a novel ruthenium sensitizer and its application in dye-sensitized solar cells for conversion of sunlight into electricity, *Inorganic Chemistry*, Vol. 44, No. 2, 2005 179.
12. O. Schwarz, D. van Loyen, S. Jockusch, N.J. Turro, H. Durr, Preparation and application of new ruthenium(II) polypyridyl complexes as sensitizers for nanocrystalline TiO₂, *Journal of Photochemistry and Photobiology A: Chemistry* 132 (2000) 91-98.
13. T. Ohno, T. Mitsui, M. Matsumura, Photocatalytic activity of S-doped TiO₂ photocatalyst under visible light, *Chemistry Letters*, Vol. 32, No.4, (2003).
14. T. Ohno, T. Tsubota, M. Toyofuku, R. Inaba, Photocatalytic Activity of a TiO₂ Photocatalyst Doped with C⁴⁺ and S⁴⁺ Ions Having a Rutile Phase Under Visible Light, *Chemistry Letters*, Vol. 98, No. 4, December 2004.
15. H. Ross, J. Bendig, S. Hecht, Sensitized photocatalytical oxidation of terbutylazine, *Solar Energy Materials and Solar Cells*, 33 (1994) 475-481.
16. T. Ohno, M. Akiyoshi, T. Umebayashi, K. Asai, T. Mitsui, M. Matsumura, Preparation of S-doped TiO₂ photocatalysts and their photocatalytic activities under visible light, *Applied catalysis A: General*, 265 (2004) 115-121.
17. T. Ohno, Z. Miyamoto, K. Nishijima, H. Kanemitsu, F. Xueyuan, Sensitization of photocatalytic activity of S- or N-doped TiO₂ particles by adsorbing Fe³⁺ cations, *Applied Catalysis A: General*, 302 (2006) 62-68.
18. S. Min, F. Wang, Y. Han, An investigation on synthesis and photocatalytic activity of polyaniline sensitized nanocrystalline TiO₂ composites, *J Mater Sci* (2007) 42:9966-9972.
19. J. Lobedank, E. Bellmann, J. Bendig, Sensitized photocatalytic oxidation of herbicides using natural sunlight, *Journal of Photochemistry and Photobiology A: Chemistry* 108 (1997) 89-93.
20. T. Ohno, Development of visible light sensitive TiO₂ photocatalysts and their sensitization using Fe³⁺ ions, *Journal of the Japan Petroleum Institute*, 49, (4), 168-176 (2006).

21. O. Ozcan, F. Yukruk, E.U. Akkaya, D. Uner, Dye sensitized artificial photosynthesis in the gas phase over thin and thick TiO₂ films under UV and visible light irradiation, *Applied Catalysis B: Environmental* 71 (2007) 291-297.
22. A.F. Nogueira, A.L.B. Andre, H. Winnischofer, M. Nakamura, F.M. Engelmann, K. Araki, H.E. Toma, Photoelectrochemical properties of supramolecular species containing porphyrin and ruthenium complexes on TiO₂ films.
23. M. Kitano, M. Takeuchi, M. Matsuoka, J.M. Thomas, M. Anpo, Preparation of visible light-responsive TiO₂ thin film photocatalysts by an RF magnetron sputtering deposition method and their photocatalytic reactivity, *Chemistry Letters*, (2005), 34(4), 616-617.
24. K. Hirano, E. Suzuki, A. Ishikawa, T. Moroi, H. Shiroishi, M. Kaneko, Sensitization of TiO₂ particles by dyes to achieve H₂ evolution by visible light, *Journal of Photochemistry and Photobiology A: Chemistry* 136 (2000) 157-161.
25. G.R. Bamwenda, S. Tsubota, T. Kobayashi, M. Haruta, Photoinduced hydrogen production from an aqueous solution of ethylene glycol over ultrafine gold supported on TiO₂, *Journal of Photochemistry and Photobiology A: Chemistry*, 77 (1994) 59-67.
26. G.R. Bamwenda, S. Tsubota, T. Nakamura, M. Haruta, Photoassisted hydrogen production from a water-ethanol solution: a comparison of activities of Au-TiO₂ and Pt-TiO₂, *Journal of Photochemistry and Photobiology A: Chemistry*, 89 (1995) 177-189.
27. M. Kitano, K. Tsujimaru, M. Anpo, Decomposition of water in the separate evolution of hydrogen and oxygen using visible light-responsive TiO₂ thin film photocatalysts: Effect of the work function of the substrates on the yield of the reaction, *Applied Catalysis A: General*, 314 (2006) 179-183.
28. M. Anpo, M. Takeuchi, The design and development of highly reactive titanium oxide photocatalysts operating under visible light irradiation, *Journal of Catalysis* 216 (2003) 505-516.

29. E. Thimsen, N. Rastgar, P. Biswas, Nanostructured TiO₂ Films with Controlled Morphology Synthesized in a Single Step Process: Performance of Dye-Sensitized Solar Cells and Photo Water splitting, *Journal of Physical Chemistry C* (2008), 112(11), 4134-4140.
30. S. Takabayashi, R. Nakamura, Y. Nakato, A nano-modified Si/TiO₂ composite electrode for efficient solar water splitting, *Journal of Photochemistry and Photobiology, A: Chemistry* (2004), 166(1-3), 107-113.
31. J.S. Jang, H.G. Kim, V.R. Reddy, S.W. Bae, S.M. Ji, J.S. Lee, Photocatalytic water splitting over iron oxide nanoparticles intercalated in HTiNb(Ta)O₅ layered compounds, *Journal of Catalysis*, 231 (2005) 213-222.
32. G.R. Bamwenda, H. Arakawa, The visible light induced photocatalytic activity of tungsten trioxide powders, *Applied Catalysis A: General* 210 (2001) 181-191.
33. C. Koenigstein, Some aspects of photochemical systems for direct light-induced hydrogen production, *Journal of Photochemistry and Photobiology A: Chemistry*, 90 (1995) 141-152.
34. K. Maeda, M. Eguchi, S.A. Lee, W. J. Youngblood, H. Hata, and T.E. Mallouk, Photocatalytic hydrogen evolution from hexaniobate nanoscrolls and calcium niobate nanosheets sensitized by ruthenium(II) bipyridyl complexes, *J. Phys. Chem. C*, 2009, 113, 7962–7969.
35. S. Masud, M. Zarei, M.L. Lopez, J. Gardea-Torresdey, C.V. Ramana, G.B. Saupe, Photoreduction of Metallic Co-catalysts onto Novel Semiconducting Metal Oxides, *Materials Science and Engineering B*, 2010 (under review).
36. M. Zarei, S.M.S. Masud, G.B. Saupe, Using New Porous Nanocomposites for Photocatalytic Water Decontamination, *Mater. Res. Soc. Symp. Proc.* 1145-MM04-36, 2009.

Vita

Mr. S. M. Sarif Masud was born in Bangladesh and did his bachelor degree in 1999 in Chemical Engineering and Polymer Science at Shahjalal University of Science and Technology in Bangladesh and master's degree in 2004 in Chemical Engineering at Chalmers University of Technology in Sweden. Mr. Masud started his Ph.D. study in Materials Science and Engineering at The University of Texas at El Paso in 2006 and worked as a research assistant in the Department of Chemistry. In his Ph.D. research he developed macroporous wide band gap semiconductor photocatalysts for water splitting to synthesize hydrogen gas as a renewable source of energy. The materials also exhibited excellent catalytic activity to decontaminate water.

In his early career Mr. Masud Taught Fluid Mechanics, Sciences of Material, Reaction Engineering and Reactor Design, Pharmaceutical Technology, and Unit Operations as a faculty in the department of Chemical Engineering and Polymer Science at Shahjalal University of Science and Technology in Bangladesh and worked as a intern Chemical Engineer in Volvo Technology Corporation in Sweden while studying his masters degree in Sweden.

Mr. Masud received several prestigious awards that include Dodson Dissertation Fellowship, Graduate School Research Award, General Motors Engineering Excellent Award, NASCAR/Wendell Scott Award, Cotton Memorial Scholarship and National Science Foundation Scholarship. Mr. Masud published two papers in scientific journals and submitted two more papers that are on the way of being published. He also attended eight national and international conferences such as Materials Research Society, American Chemical Society, North American Catalytic Society, and International Materials Research Congress in U.S.A. and Mexico.

Permanent address: 1127 Los Angeles Dr, El Paso, Texas, 79902

This dissertation was typed by the author.